NASA Contractor Report 4189

# High-Power AlGaAs Channeled Substrate Planar Diode Lasers for Spaceborne Communications

J. C. Connolly, B. Goldstein, G. N. Pultz,
S. E. Slavin, D. B. Carlin, and M. Ettenberg

CONTRACT NAS1-17441
NOVEMBER 1988



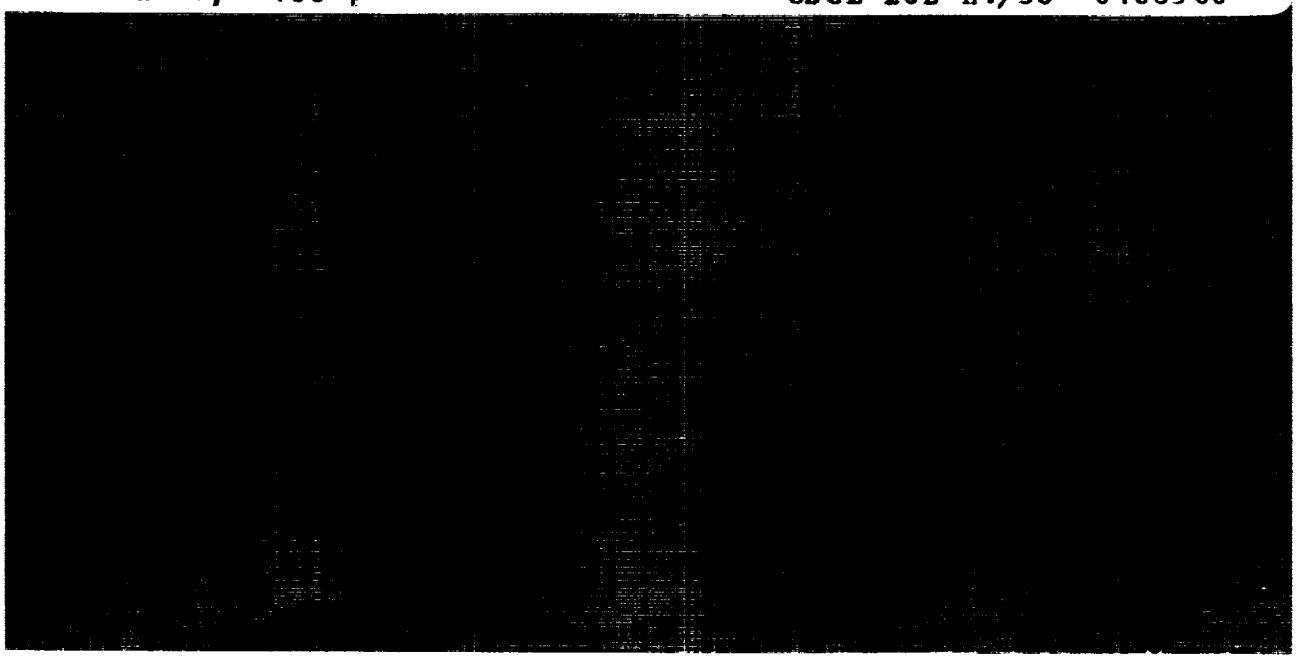

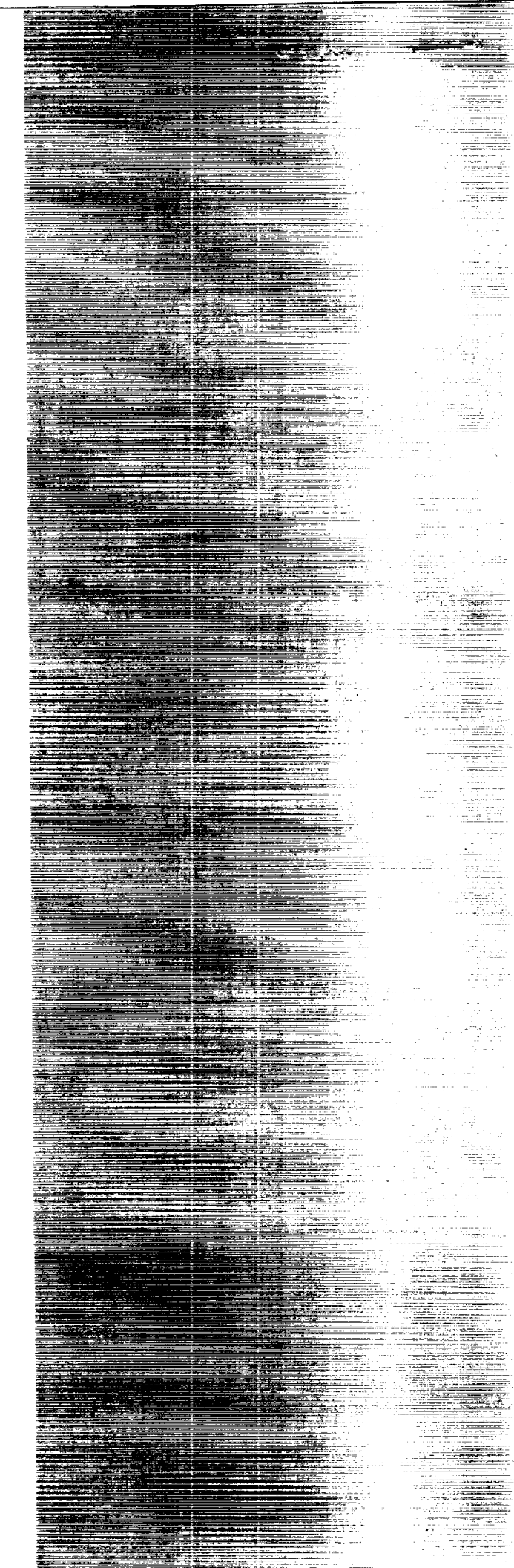

NASA Contractor Report 4189

# High-Power AlGaAs Channeled Substrate Planar Diode Lasers for Spaceborne Communications

J. C. Connolly, B. Goldstein, G. N. Pultz,
S. E. Slavin, D. B. Carlin, and M. Ettenberg
*David Sarnoff Research Center*
*Princeton, New Jersey*

Prepared for
Langley Research Center
under Contract NAS1-17441

National Aeronautics
and Space Administration

**Scientific and Technical
Information Division**

**1988**

## PREFACE

This report describes work performed from 28 June 1986 to 27 June 1987 at RCA Laboratories in the Optoelectronics Research Laboratory, B. Hershenov, Director, under Contract No. NAS1-17441. M. Ettenberg was the Project Supervisor, and D. B. Carlin, J. C. Connolly, G. N. Pultz, and B. Goldstein were Project Scientists. Other contributors to this research were J. K. Butler, G. A. Evans, N. A. Dinkel, F. R. Elia, M. G. Harvey, D. B. Gilbert, T. R. Stewart, J. J. Hughes, E. DePiano, D. P. Marinelli, D. T. Tarangioli, N. W. Carlson, D. J. Channin, V. J. Masin, S. E. Slavin, F. Z. Hawrylo, S. L. Palfrey, and A. R. Dholakia.

# Table of Contents

# Table of Contents (cont'd.)

# List of Illustrations

## List of Illustrations (cont'd.)

## List of Illustrations (cont'd.)

## List of Illustrations (cont'd.)

## SUMMARY

The fabrication procedures and theoretical understanding of high-power, 8600- to 8800-Å channeled substrate planar (CSP) lasers have been expanded, particularly in areas that focus on increasing power capability and reliability. These improvements have been realized without sacrificing the superior properties of the CSP laser, such as non-astigmatic wavefronts, modulation performance, and beam quality.

The single-spatial-mode, output power level for a discrete device has reached 70 mW cw. This value was chosen because of "kink" in the P-I curve and broadening of lateral far-field at values above 70 mW. The overall power capability for the laser has been extended to 190 mW cw, a 50% improvement over the results reported previously. The typical lateral and perpendicular far-field radiation patterns at the beam full width half power (FWHP) point for these devices are 7° and 27°, respectively. Although no means are provided to stabilize the longitudinal mode of the laser, a few selected devices displayed stable single mode cw operation at power levels up to 90 mW.

The results of computer modeling studies identified the importance of optical absorption or loss in the CSP structure and we have been able to correlate these findings with experimental results. In addition, we have found that the thickness of the n-cladding layer in the structure does not significantly alter the lateral effective index profile. In other related studies, we were able to identify and correlate the effect of compositional changes on the structure.

The reliability of the CSP lasers has also benefited from our new findings. We have been able to increase the lifetesting power level from 30 to 50 mW and have changed our test mode from a constant-current to constant-power format. This format change has permitted us to increase the stress level placed upon the devices and to monitor the performance of the devices in a mode similar to their operation in space. The results of CSP lasers placed on lifetest at 50 mW (50% duty cycle; 10 MHz) output power and at operating temperatures of 25°C, 50°C, and 70°C have shown room temperature lifetimes of approximately 3,000 h, a significant improvement over our previous work.

A new type of CSP structure has also been demonstrated, the distributed-feedback (DFB) CSP laser. This structure contains a grating that stabilizes the longitudinal mode of the CSP laser. Distributed-feedback operation has been obtained at room temperature over an 8°C temperature range. This structure has

not only provided longitudinal mode stability but has displayed superior wavelength-temperature dependence over the conventional CSP structure (0.7 vs 3 Å/°C) without degrading its excellent performance properties.

## HIGHLIGHTS

**High-power, single-spatial mode 8600- to 8800-Å CSP lasers**

- 190-mW, cw output power capability
- Single spatial mode operation up to 70 mW cw
- Room temperature lifetimes of 3,000 h at 50 mW
- Improved computer modeling capabilities
- Modulation rate to 2 GHz

**High-power, distributed-feedback CSP lasers**

- Demonstration of first DFB-CSP laser structure
- Single longitudinal mode operation up to 40 mW
- 0.7 Å/°C wavelength dependence upon temperature

# I. INTRODUCTION

The work described in the previous Annual Report centered on the development of both individual and arrays of high-power, single-mode diode lasers for potential use in areas such as space communications, optical data and storage, and local area optical communication networks. In the work on individual laser sources, we reported record power in a fundamental mode from channeled substrate planar (CSP) lasers having improved efficiency and reduced threshold current density without sacrificing the excellent beam qualities of the device. Similar results were reported for the individually addressed CSP laser diode arrays.

In this annual report, the research and development work was continued to improve further and refine the high-power, CSP laser structure for wavelength emission at 8600 to 8800 Å. Extensive computer modeling studies were conducted to identify the ultimate output power, performance, and reliability limitations of the device as well as the parameters that control them. The results of these studies were used to fabricate CSP diode lasers that have displayed higher output powers, lower threshold currents, higher efficiencies, and improved reliability.

A new laser structure was also developed that incorporates a grating to stabilize the longitudinal mode of the CSP diode laser during modulation. Another added benefit of the grating is the improved wavelength temperature dependence over conventional devices. The improvements described above have been shaped by the requirements of the NASA Advanced Communications Test Satellite (ACTS) program.

# II. DIODE LASER PERFORMANCE AT 8600- TO 8800-Å

The goal of this program was the development of AlGaAs diode lasers with an emission wavelength at 8600 to 8800 Å comparable in performance with previous diode lasers fabricated at 8350 Å. In addition, the focus of the program was to develop a new diode laser structure that operates in a stable longitudinal mode. The standard diode laser geometry that provides operation in a stable, single-spatial mode offers no method of longitudinal mode stabilization. The eventual use of these diode lasers would be as light sources for use in intersatellite communications systems and, specifically, the NASA Advanced Communications Technology Satellite (ACTS) System [1].

In this section, computer modeling, liquid phase epitaxial (LPE) growth, characterization, and reliability of the 8600 to 8800 Å, high-power CSP diode lasers are discussed. A later section describes the method used to incorporate a grating in this structure to stabilize the longitudinal mode without degrading its desirable performance characteristics.

## A. COMPUTER MODELING

The computer modeling program used at the David Sarnoff Research Center for this work has been developed and refined over years as our understanding of the operation of the CSP structure has improved. The method of modeling that we used starts with the basic laser structure and the various components associated with laser operation, such as the current distribution, carrier diffusion gain profile, and heating effects, which are sequentially incorporated into our model. As these various components are added, iterations are performed until self-consistency is obtained within the error limits imposed upon the device parameters.

A close examination of both the structure and the performance characteristics of high-power CSP lasers grown in the three LPE reactors used for this work was initiated. The goal of this study was to identify those parameters that yielded the most significant consequence to the high-power performance and operational lifetime of the CSP diode laser.

The first experimental parameter identified as significant to the performance of CSP lasers operating at an emission wavelength >8600 Å was the thickness of the n-cladding layer. Although no correlation could be found between

the thickness of the n-cladding layer and high-power operation, there was an indication that CSP structures containing thicker than normal n-cladding layers (0.4 to 0.5 μm vs 0.2 to 0.3 μm) displayed longer operational lifetimes. In addition, these results were also supported by similar findings on two other AlGaAs LPE reactors used for the growth of phase-locked arrays and 0.83-μm CSP lasers. This result may be significant since the increased operational lifetimes may be related to the design of the CSP structure itself and not with the quality of the LPE prepared materials, processing, and/or the growth system.

Based upon these results, a computer modeling study was performed varying the thickness of the n-cladding layer to determine the effect on the lateral index, gain, and optical field profiles in the CSP structure. In addition, the total modal losses were examined and found to be insensitive to the n-cladding thickness. These losses would directly effect the threshold current value of the device. An increase in the modal loss would lead to a corresponding increase in threshold current due to the higher gain necessary to support lasing. The experimental results support these findings since no correlation between the n-cladding thickness and threshold current was found.

In our modeling, we use the effective complex index technique to calculate any change in the mode properties in the laser structure [3] that would alter the CSP lasing properties. The complex effective index (n*) consists of a real and an imaginary part and is defined as:

$$n^* = \lambda/k_0 = \beta/k_0 + j\,\alpha/k_0$$

where $\beta$ is the propagation constant, $k_0$ is free space wavenumber ($2\pi/\lambda$), $\alpha$ is the absorption coefficient, and $\lambda = \beta + j\alpha$ is the longitudinal propagation constant of the mode. The complex effective index is calculated both in the channel and the winged regions of the structure, and the difference between these values is called the lateral effective-index step. The lateral effective-index step ($\Delta n$) in the CSP structure is defined as:

$$\Delta n = \beta/k_0 \text{ (channeled region)} - \beta/k_0 \text{ (winged region)}$$

Figure 1 shows a plot of the complex lateral effective index as the thickness of the n-cladding layer is varied between 0.2 and 1.5 μm is shown. The structure was modeled using an n- and p-cladding layer composition of $Al_{0.27}Ga_{0.73}As$ and

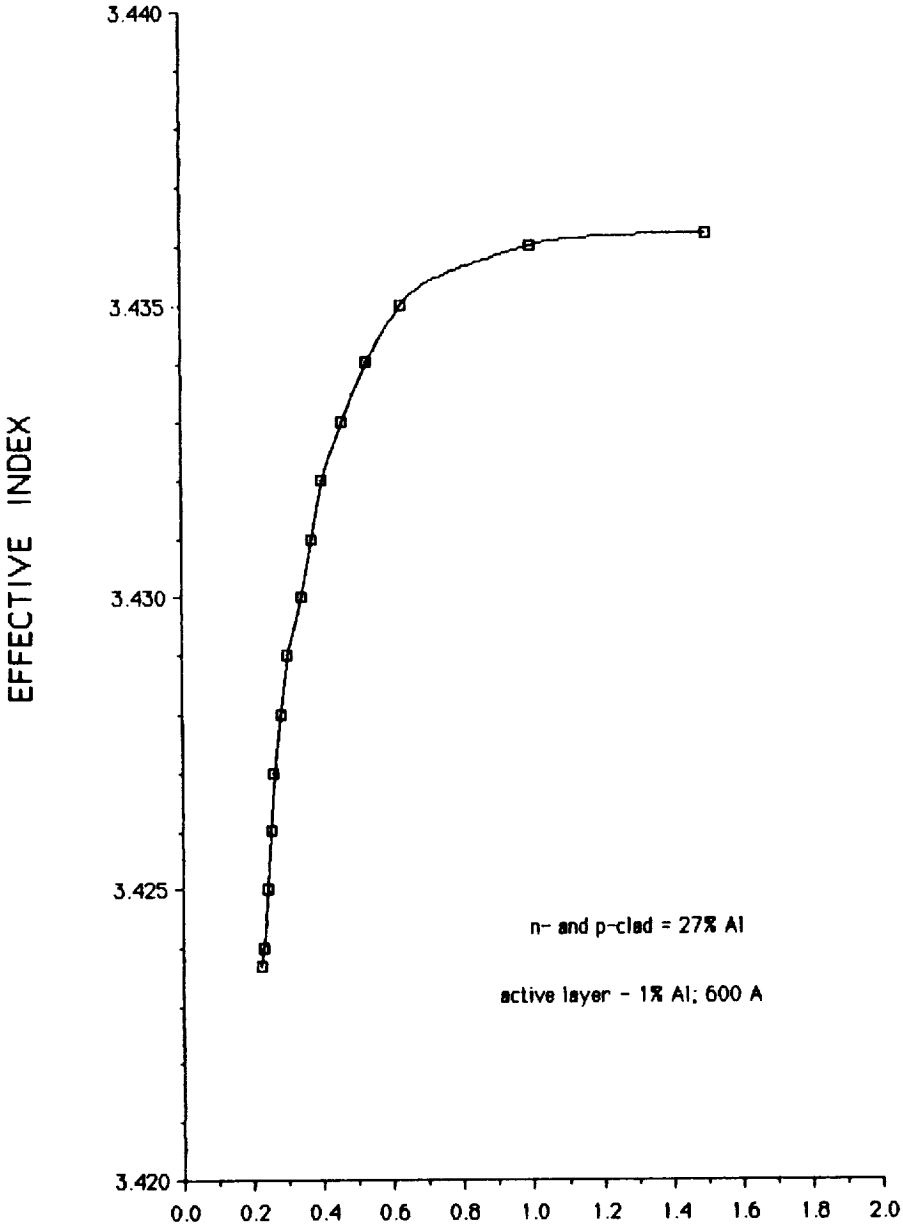


Figure 1. Complex lateral effective index for a 8650-Å CSP laser as a function of n-cladding layer thickness.

an active layer composition of $Al_{0.01}Ga_{0.99}As$. The active- and cladding-layer thicknesses are 0.06 and 1.5 μm, respectively, and the channel width is 4 μm. For an n-cladding layer thickness greater than 1 μm, the effective index remains unchanged at 3.436 (i.e., channel region) and decreases to 3.424 for a thickness of 0.25 μm. Thus, the lateral effective index step for a CSP laser with a n-cladding

layer thickness of 0.25 μm is $1.2 \times 10^{-2}$. The steep slope of the curve for n-cladding thicknesses between 0.25 and 0.6 μm demonstrates the uniformity and thickness control necessary for the growth of this layer. Small changes in the thickness of this layer can significantly alter the performance of the CSP laser.

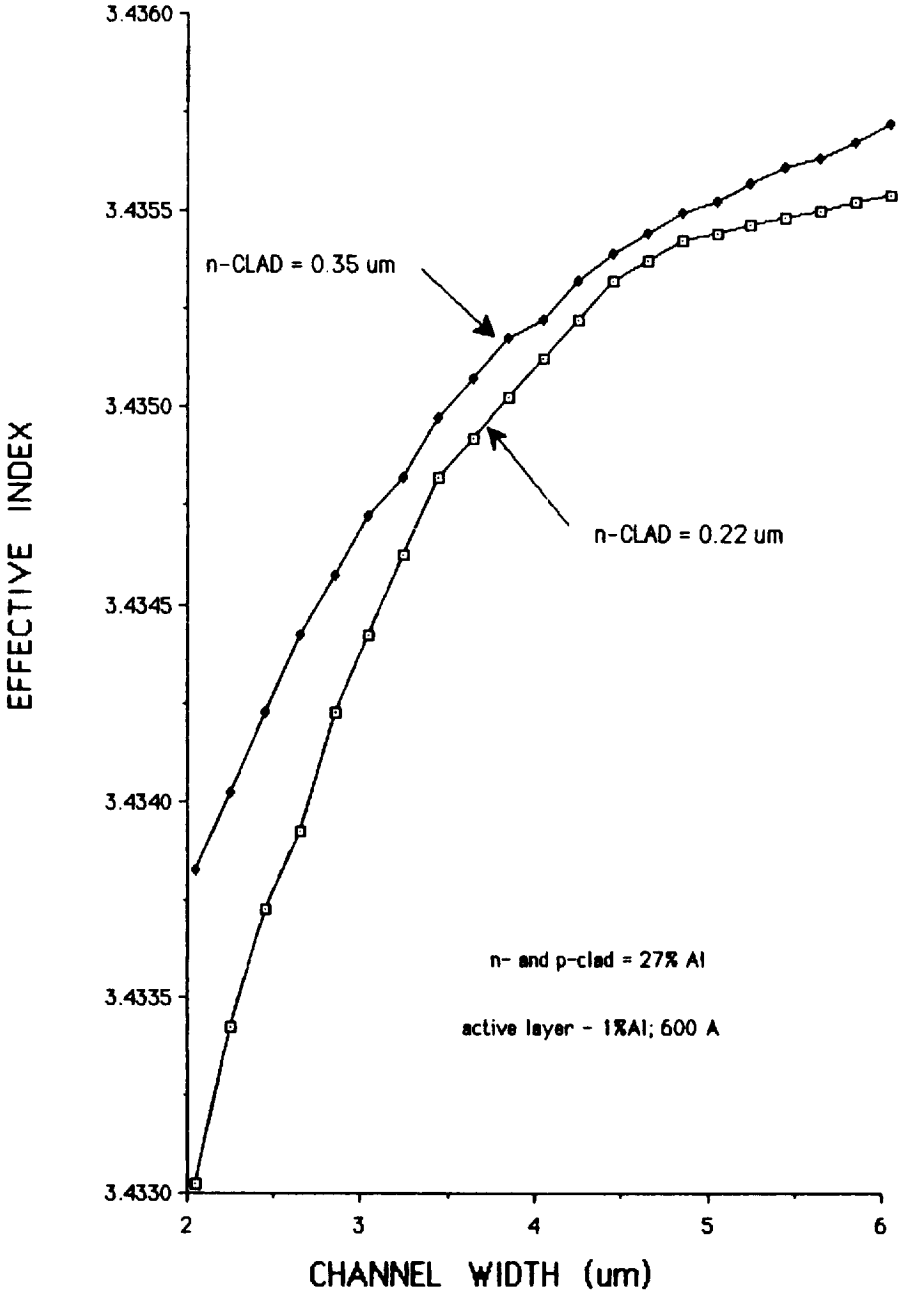


Figure 2. Complex lateral effective index profile for a 8650 Å CSP laser with an n-cladding layer thicknesses of 0.22 and 0.35 μm as a function of the V-channel width.

In Fig. 2, a plot of the complex, lateral effective index for CSP laser structures with n-cladding layer thicknesses of 0.22 and 0.35 μm is shown. The other parameters for the CSP laser remain unchanged. As the channel width is varied from 2 to 6 μm, the complex lateral effective index profiles for the two different n-cladding layer thicknesses varies at most $5.5 \times 10^{-4}$ for the range of channels (i.e., 3.0 - 4.5 μm) used in fabrication. This small index difference would not significantly alter the operation of the CSP structure. Generally, a change of $2 \times 10^{-3}$ or greater is required to change the modal properties of the structure.

Although the total modal losses in the CSP structure were found to be insensitive to the n-cladding thickness, the normalized loss or the loss parallel to the direction of the active layer varied significantly. In Fig. 3, the normalized loss for the CSP structure is plotted against the n-cladding thickness. The device parameters are the same as used previously. There is a significant change in the amount of loss ($8 \times 10^{-3}$) as the n-cladding layer thickness is reduced from 1.5 to 0.2 μm. Increasing the thickness to 0.4 μm reduces this loss to $3 \times 10^{-3}$. Loss in the CSP structure is critical for its operation in a single-spatial mode. A small change in loss represents a large change in the complex lateral effective index profile. If the loss value was zero in the structure while the real part of complex lateral index profile remained unchanged, the structure would behave as a ridge-guide-type laser.

The loss mechanism in the CSP structure is characterized by absorption of the optical mode by the highly absorbent GaAs substrate (10,000 $cm^{-1}$). The optical absorption in the substrate causes local heating of the substrate on either side of the V-channel. This heat must be removed from the substrate for the CSP laser to operate at high powers with reliable lifetimes. In our normal mounting configuration, the CSP laser is mounted p-side down to the heatsink. Thus, the heat in the substrate must be removed by re-radiation of the absorbed heat across the active region, through the p-cladding and cap layers, to the copper heatsink. Absorption cannot be totally eliminated in the CSP laser since absorption of the optical mode by the substrate is crucial to operation in a single-spatial mode at high output powers.

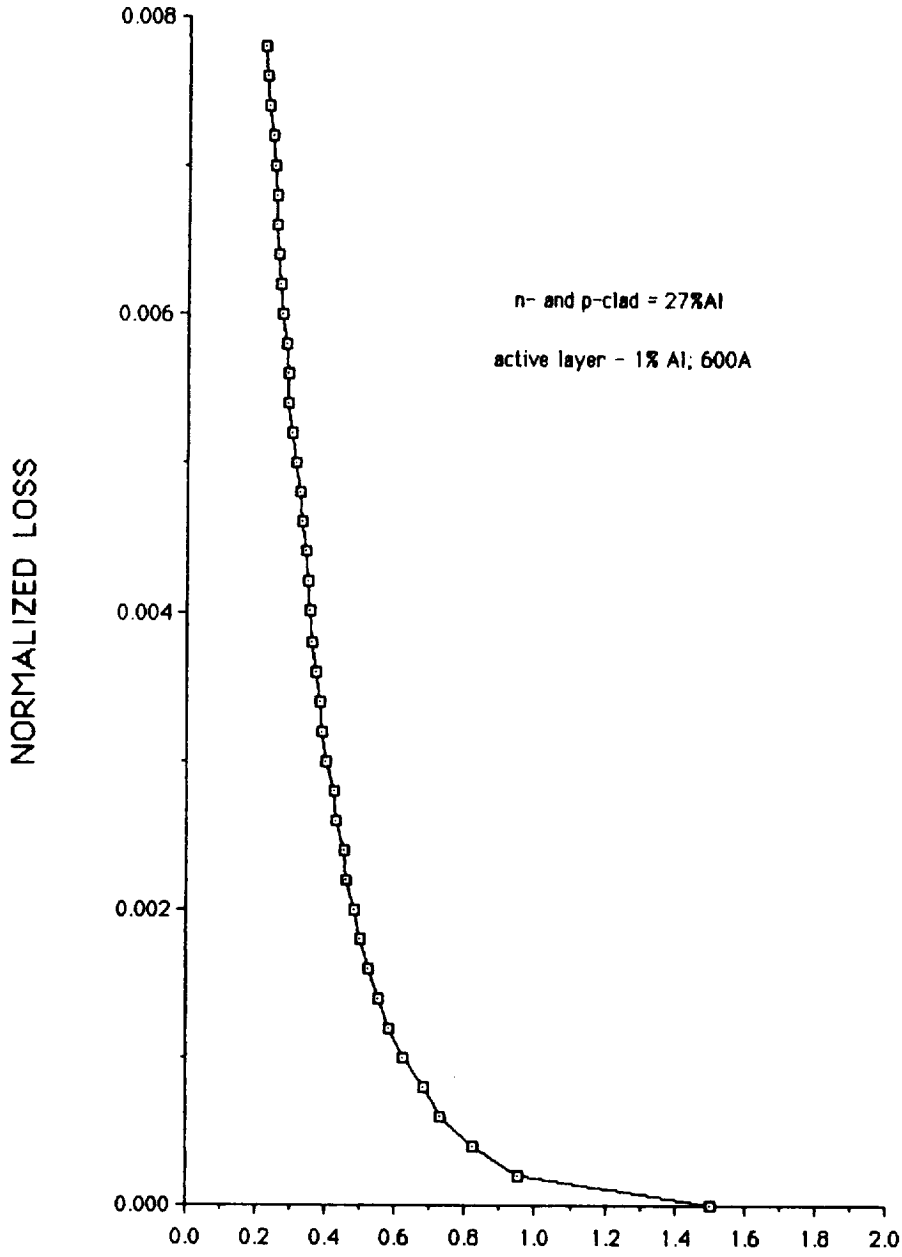


Figure 3. Normalized loss for a 8650-Å CSP laser as a function of n-cladding layer thickness.

The theory described above that associates long operational lifetimes with reduced heating along the shoulders of the V-channel fits the experimental evidence found from our analysis of lifetest data. The computer model used for this study clearly demonstrates that thicker n-cladding layers reduce the localized loss or absorption of the optical mode by the GaAs substrate. This reduction

translates to reduced heating in and around the active region of the device. The reduced heating permits the device to operate at a lower junction temperature while still maintaining the same output power level. Thus, longer operational lifetimes should be obtained. The absorption of the optical mode by the substrate may prove to be a very important factor not only for increased reliability, but for operation at higher output power levels.

In another modeling study, we investigated the effects of non-uniform photon densities along the propagation direction for high-power CSP lasers with low facet reflectivities. CSP lasers with high reflectivity facets (>30%) have almost uniform photon density along their longitudinal axis, allowing the assumption of uniform gain to be applied in their analysis. However, the highest powers obtained from CSP lasers are obtained by using a high-reflectivity rear facet (80%-90%) and a low-reflectivity output facet (0.5%-10%), resulting in large variations of the photon density along the lasing axis. By extending our previous work on uniform longitudinal gain analysis based on the "self-consistent model" [3], we have been able to develop simple phenomenological equations for the modal gain coefficient, the threshold current density and, in the limit of high facet reflectivities, the radiated power.

In self-consistent models the carrier density in the active layer is derived from a solution of the diffusion equation having both source and sink terms. The source for the injected carriers is the drive current, whereas the sink is the stimulated recombination. The current flow into the active layer varies laterally, and the lateral carrier diffusion within the active region affects the optical gain profile, modifying the shape of the optical field distribution in the CSP laser diode. The spatial dependence of the recombination term is computed from the product of the lateral gain profile and the photon density in the active layer as a function of position along the longitudinal direction.

In any laser structure the intracavity power $P_{(z)}$ is the sum of the forward and backward waves and is defined as:

$$P_{(z)} = P^{+}_{(z)} + P^{-}_{(z)}$$

For lasers having high facet reflectivities (>30%), the intracavity power is almost constant along the z, or lasing, direction. However, when reflectivities are lower, as in the case for high-power CSP lasers, the intracavity power exhibits relatively large changes along the lasing direction. In Fig. 4, the points show the modal

gain coefficient, computed from the self-consistent solutions of the carrier diffusion and Maxwell equations, as a function of the intracavity power for different values of drive current. The CSP device used for this work contained a 0.06-μm-thick GaAs active layer having an index of 3.6, a 0.4-μm-thick AlGaAs n-cladding layer having an index of 3.4, and a 1.5-μm-thick AlGaAs p-cladding layer having an index of 3.4. Both the V-channel and contact stripe widths were 6 μm.

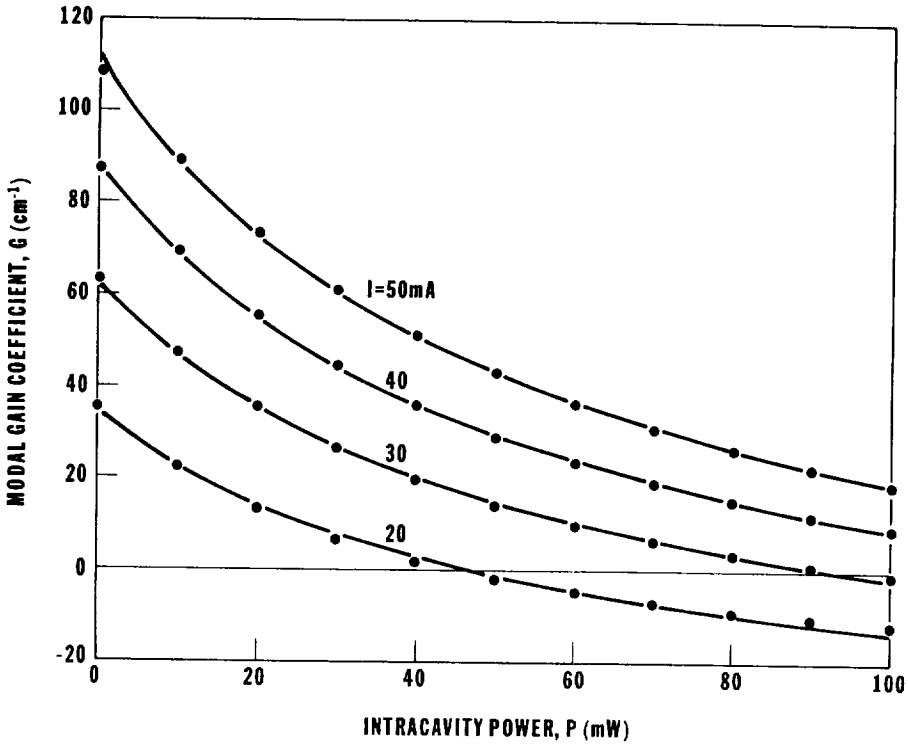


Figure 4. Optical gain characteristics of the fundamental mode as a function of the intracavity power. The drive current is for a device of length L = 100 μm.

Although the numerical data can be used to calculate the longitudinal variation of the gain in a laser with known facet reflectivities, it is useful to fit numerically calculated modal gain coefficient points to an analytical expression written as:

$$G(P) = \left(\frac{I}{I_0}\right)^c \frac{G_0}{(1 + P/P_s)^d} - \alpha_1$$

where c, d, $G_0$, $P_s$, and $\alpha_1$ are unknown constants. An optimization procedure for a least-squares fit to the computed values of the self-consistent modal gives c =

0.708, d = 0.687, $G_0$ = 51.4 $cm^{-1}$, $P_s$ = 41.2 mW, and $\alpha_1$ = 49.6 $cm^{-1}$. The value of $I_0$ is arbitrary, but we used $I_0$=10 mA for the $G_0$ value above. The resulting gain curves for these parameters are illustrated in Fig. 4.

When one or both of the facet reflectivities are small, the intracavity power varies considerably along the lasing axis. Thus, the intracavity power must be computed from the integral equation

$$P(z) = P_0\left[\exp\left(\int_0^z G(P)\,dz'\right) + \frac{1}{R_2}\exp\left(-\int_0^z G(P)\,dz'\right)\right]$$

where $P_0$ is an eigenvalue, facet 2 lies at z = 0, and facet 1 lies at z = L. The boundary condition on G(P) requires that its integral over the length of the cavity be $1/2\ln(1/R_1R_2)$.

In Fig. 5, the results for a CSP diode laser operating at an output power level of 50 mW and having a cavity length of 250 μm are shown. The rear facet of the laser has a reflectivity of 100%, and the output facet reflectivity is treated as a variable. When the output facet reflectivity is 30%, the power along the lasing axis is almost constant. However, if the reflectivity of the output facet is reduced to 5% by applying a 1/4 λ coating of $Al_2O_3$, the intracavity power varies from about 24 mW at the rear facet to about 55 mW at the emitting facet.

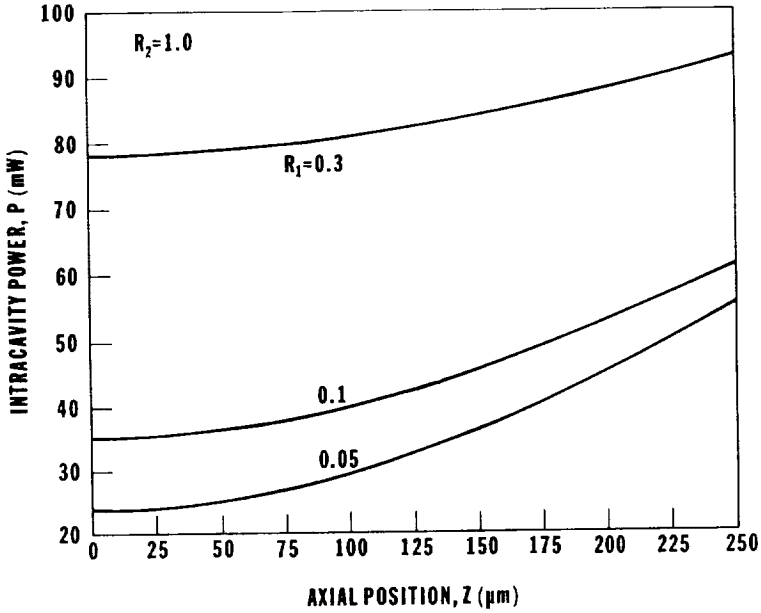


Figure 5. The intracavity power computed for a laser of length L = 250 μm. The back facet has $R_2$ = 1, while the front facet reflectivity is treated as a parameter. The total emission power from the front facet is 50 mW.

A more useful way of looking at the effects of mirror reflectivity upon the performance of the CSP laser is to examine the change in the output power vs drive current (P-I) plots for the same laser diode having various output facet reflectivities. Using the same device parameters as before, the P-I curves were calculated for the various facet reflectivities and are displayed in Fig. 6. From the figure, it can be seen that the threshold current value for the laser almost doubles as the facet reflectivity is reduced from 30% to 5%. The slope efficiency of the CSP laser also increases as the facet reflectivity is decreased. A more detailed description of these modeling results can be found in Appendix A of this report.

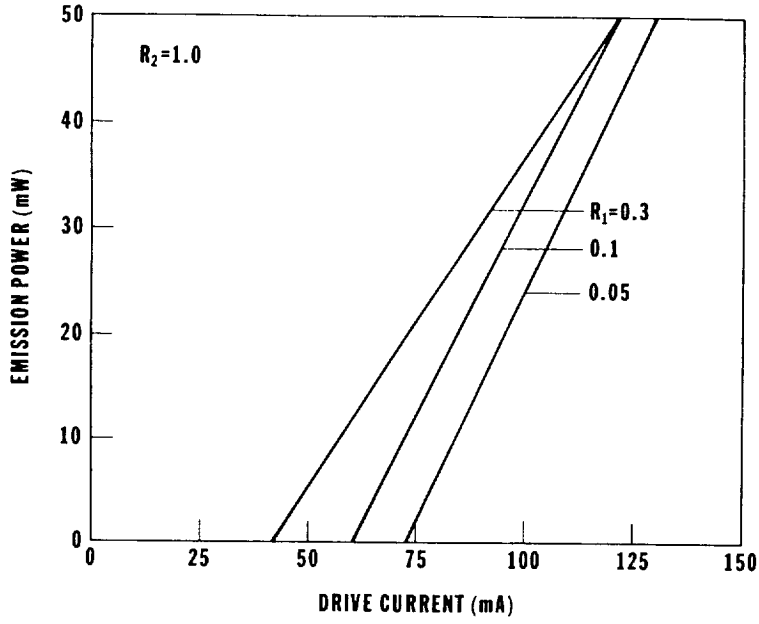


Figure 6. Emission power from the front facet of an AlGaAs laser vs drive current.

## B. LIQUID PHASE EPITAXIAL GROWTH

The results of our computer modeling clearly points out the importance of layer thickness, compositional, and layer uniformity across the growth substrate. Thus, we introduced the use of a new, fully automated LPE growth system. This LPE growth system was designed and constructed in-house since commercially available systems did not contain the necessary modifications and the degree of automation required for our type of growth process. Some of the unique features associated with our growth system are: (1) all gas lines and system components are fabricated from #316L stainless steel and are tungsten in gas (TIG) welded wherever possible and metal gasket sealed when not; (2) a vacuum pumping

system has been added to the gas-handling system to permit a pump/purge procedure to be performed on the growth chamber after loading of the growth boat; (3) automatic in situ temperature profiling of the growth boat during the growth process; (4) automatic positioning of both the top and bottom sliders in the growth boat; (5) automatic positioning of the three zone growth furnace; and (6) continuous monitoring and control of the growth temperature via a thermocouple mounted inside the growth boat. A photograph of this new reactor is shown in Fig. 7. In addition, all aspects of the growth process (i.e., pressure, temperature, gas flow rate, etc.) are continuously monitored and recorded. This system is the most automated and sophisticated LPE growth reactor that we are aware of in the world.

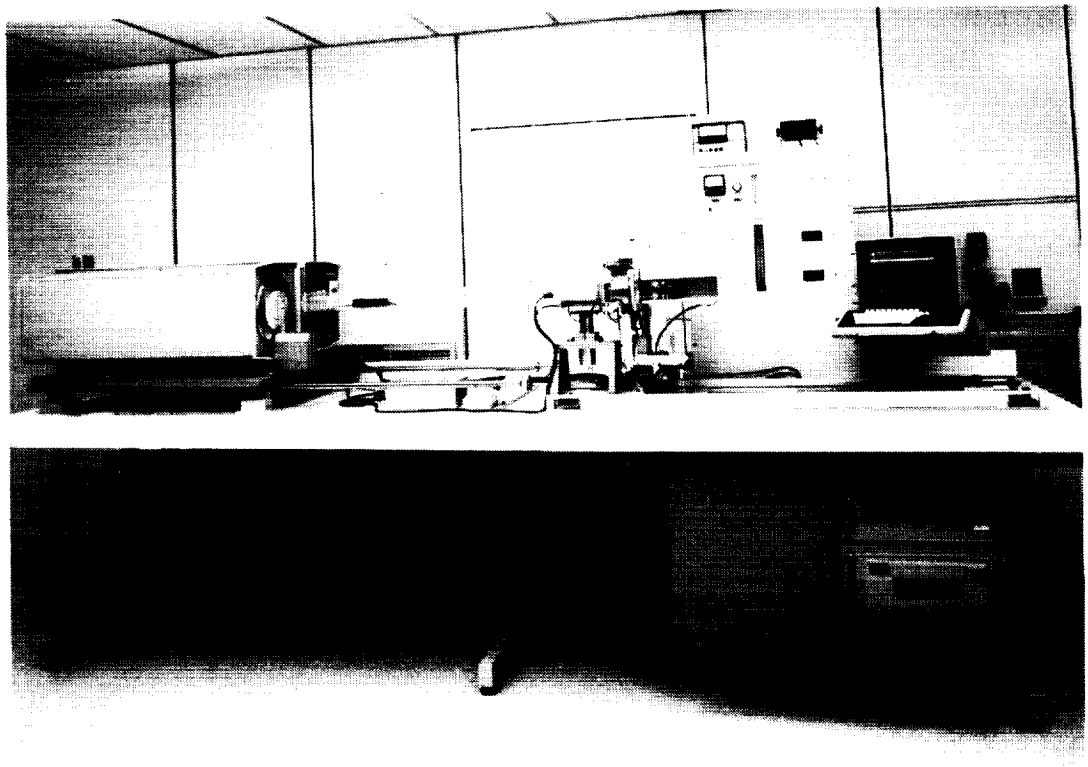

Figure 7. A photograph of an automated liquid phase epitaxial growth reactor used for the growth of CSP lasers.

In conjunction with the design of the new fully automated LPE reactor, we have redesigned the LPE growth boat. It is still fabricated from ultra-high-purity

graphite, but it has been modified to permit easy disassembly and cleaning along with improved wiping action for more complete melt removal to reduce gallium carry-over. In addition, the boat has been redesigned to accept larger substrates. A photograph of the new LPE growth boat is displayed in Fig.8. The new substrate size is 1.0 in. x 1.25 in. This increased size provides approximately 3.3 times more useable wafer area over our previous substrates. The growth melt for this boat is 10 gm as compared with 3 gm for the older design.

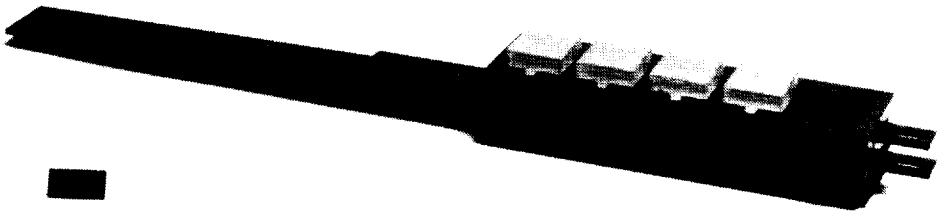

Figure 8. A photograph of the graphite growth boat used for the fabrication of CSP lasers.

One of the most important considerations in fabricating the CSP laser structure is the growth of a planar active layer while still maintaining a thin and reproducible n-cladding layer. A schematic diagram and a cross-sectional photograph of the CSP structure is shown in Fig. 9. If the active layer is nonplanar, due to incomplete filling of the V-channel in the substrate while trying to obtain a thin n-cladding layer, the lateral index profile of the CSP structure is altered leading to devices exhibiting small lasing spots and single-spatial mode operation at low power levels. On the other hand, if a planar active layer is obtained but the cladding layer is too thick, the devices will behave as gain-guided or oxide-defined contact stripe devices. The growth of a planar active layer in conjunction with a thin (0.2 to 0.4 μm) n-cladding layer requires that the growth melt be in a supersaturated condition prior to epitaxial growth. A

supersaturated condition is obtained by cooling a melt from an equilibrium condition to a temperature above the spontaneous or self-nucleation temperature. When the melt is in this state, it is normally referred to as supercooled. The exact temperature of all three parameters depends upon the composition of the melt itself. To ensure planar active-layer growth over the channel region while maintaining the appropriate thickness n-cladding layer, it is necessary to maximize the total amount of supercooling associated with the melt used for layer growth. This is accomplished in our automated growth system by using the single-phase growth method [4] for the n-cladding layer and the two-phase method [4] for the growth of the other layers in the CSP structure. The single-phase growth method permits us to accurately control the degree of supercooling present in the gallium melt prior to the introduction of the growth substrate. In addition to the quick filling of the V-channel to planarize the layer, careful control of the amount of supercooling also permits a high degree of control on the layer thickness, not only across the wafer, but from one LPE growth run to another. The single-phase growth technique may also be used for the growth of the other layers in the structure but is not necessary since the n-cladding layer grown directly on the non-planar substrate planarizes the surface for growth of the subsequent layers. The use of the single-phase growth technique for all the layers in the structure would unnecessarily complicate the growth process.

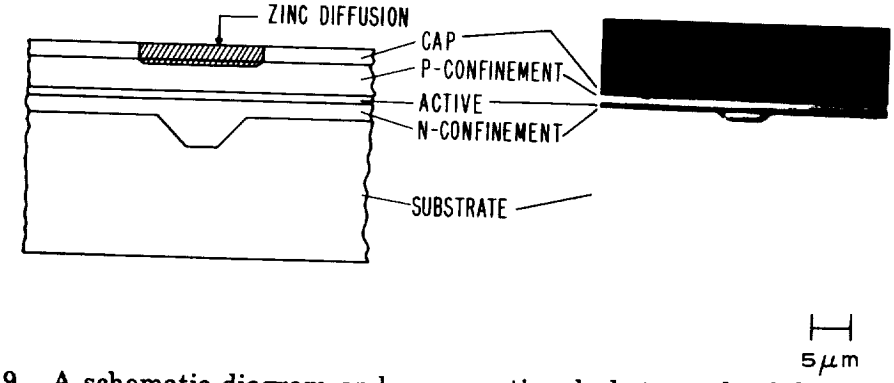


Figure 9. A schematic diagram and cross-sectional photograph of the CSP laser structure.

A detailed analysis of compositional variations within the layers of the CSP structure has been performed, and compositional changes in the n-cladding layer within the channel region have been observed. We have found that significant non-uniformities in the direction perpendicular to the junction can exist in the Al/Ga ratio. As a consequence, a large optical cavity (LOC) or enhanced substrate

loss (ESL) version of the CSP geometry may result, both of which may have significantly different characteristics from those of a conventional CSP laser. The CSP-LOC laser generally has a wider perpendicular full-width-half-power (FWHP) near-field distribution and similar or larger perpendicular far-field beam divergence compared with a conventional CSP laser. The ESL-CSP laser has an asymmetric perpendicular far-field pattern and can have either a larger or smaller FWHP perpendicular far-field pattern compared with a conventional CSP laser.

The principal experimental technique used for the surface compositional analysis on the cleaved facets of the lasers was Auger electron spectroscopy (AES) using a primary electron beam with a resolution of about 1000 Å. Figure 10(b) shows the Auger spectra that indicate the surface composition on a cleaved facet of a CSP laser at the points x = 0.3 μm and x = 1.2 μm shown in Fig. 10(a). The magnitudes of the Ga, As, and Al lines shown on the spectra reflect the concentration of these constituents at the two points and indicate that the Al concentration at the bottom of the channel is about twice that just below the active region. Note that the change in the magnitude of the Al line is tracked by a corresponding change in the magnitude of the Ga line, while the As line has remained essentially unchanged. Examining a random sampling of CSP lasers establishes that the magnitude of the concentration variations indicated in Fig.10(b) ranges from zero to a factor of about two.

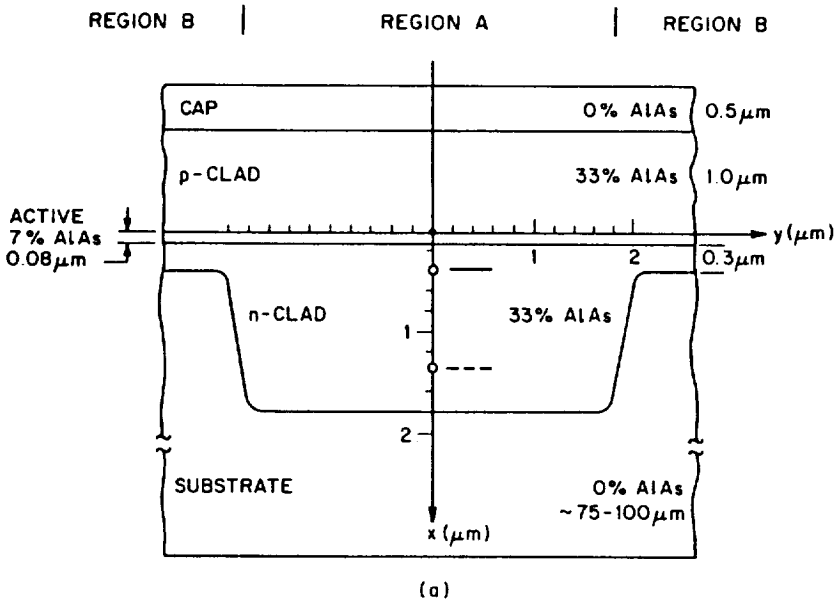


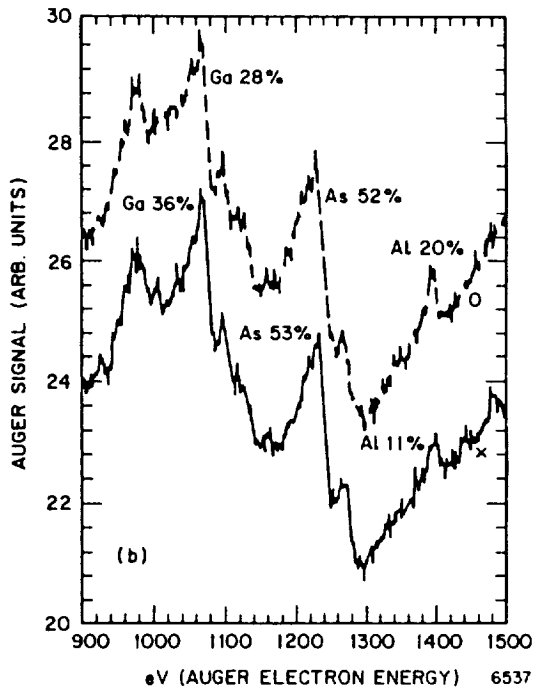


Figure 10. (a) Geometry of a typical CSP type laser; x = 0 is the top of the active layer and x = 1.8 μm is the bottom of the channel. (b) Auger analysis of a cleaved facet of a CSP laser showing a higher aluminum composition near the bottom of the channel (X = 1.4 μm, dashed line) than near the top of the channel (x = 0.4 μm, solid line).

A non-uniform Al/Ga ratio within the channel will affect the dielectric profile perpendicular to the junction. Figure 11 contains a series of possible index profiles together with their electric field distributions for (a) a uniform Al/Ga ratio in the channel, (b) a higher Al/Ga ratio at the channel bottom (CSP-LOC), and (c) a lower Al/Ga ratio at the channel bottom (ESL-CSP). Graded-index profiles are also possible; however, their characteristics are qualitatively similar to the abrupt step profiles. The Al concentrations and corresponding index values for the three structures shown in Fig. 11 are tabulated in Tables 1, 2, and 3.

**Table 1. CSP Structure.**

| layer | thickness (μm) | %AlAs | index (λ=0.83μm) | $\Gamma_{layer}$ | Re{$n^*_{eff}$} | Im{$n^*_{eff}$} |
|---|---|---|---|---|---|---|
| 1 p-clad | >1.0 | 33 | 3.40657 | .389 | | |
| 2 active | 0.08 | 7 | 3.62805 | .222 | 3.43401 | $6.6 \times 10^{-5}$ |
| 3 n-clad | 1.8 | 33 | 3.40657 | .389 | | |
| 4 substrate | ~ 75 | 0 | 3.64 | $3.4 \times 10^{-6}$ | | |

**Table 2. CSP-LOC Structure.**

| layer | thickness (μm) | %AlAs | index (λ=0.83μm) | $\Gamma_{layer}$ | Re{$n^*_{eff}$} | Im{$n^*_{eff}$} |
|---|---|---|---|---|---|---|
| 1 p-clad | >1.0 | 33 | 3.40657 | .19043 | | |
| 2 active | 0.08 | 7 | 3.62805 | .19205 | | |
| 3 LOC | 0.4 | 22 | 3.48276 | .59205 | 3.46932 | $6.6 \times 10^{-5}$ |
| 4 n-clad | 1.8 | 40 | 3.364 | .02546 | | |
| 5 substrate | ~ 75 | 0 | 3.64 | $2.9 \times 10^{-9}$ | | |

**Table 3. ESL-CSP Structure.**

| layer | thickness (μm) | %AlAs | index (λ=0.83μm) | $\Gamma_{layer}$ | Re{$n^*_{eff}$} | Im{$n^*_{eff}$} |
|---|---|---|---|---|---|---|
| 1 p-clad | >1.0 | 33 | 3.40657 | .331 | | |
| 2 active | 0.08 | 7 | 3.62805 | .190 | | |
| 3 LOC | 0.9 | 33 | 3.40657 | .346 | 3.43405 | $5.11 \times 10^{-4}$ |
| 4 n-clad | 1.8 | 26.3 | 3.45245 | .125 | | |
| 5 substrate | ~ 75 | 0 | 3.64 | .008 | | |

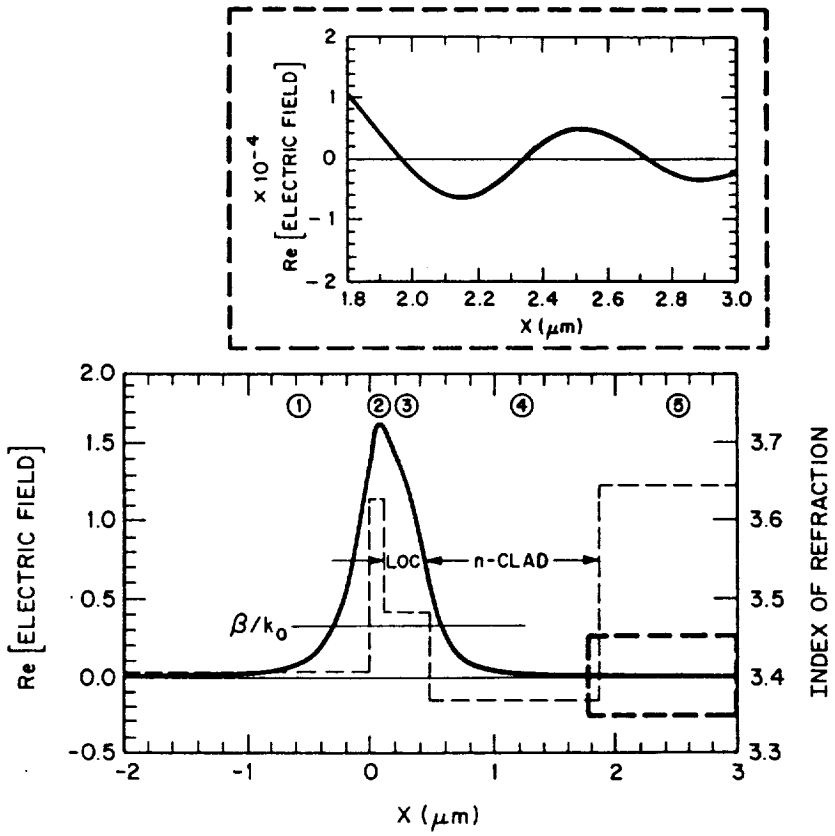


Figure 11(a)

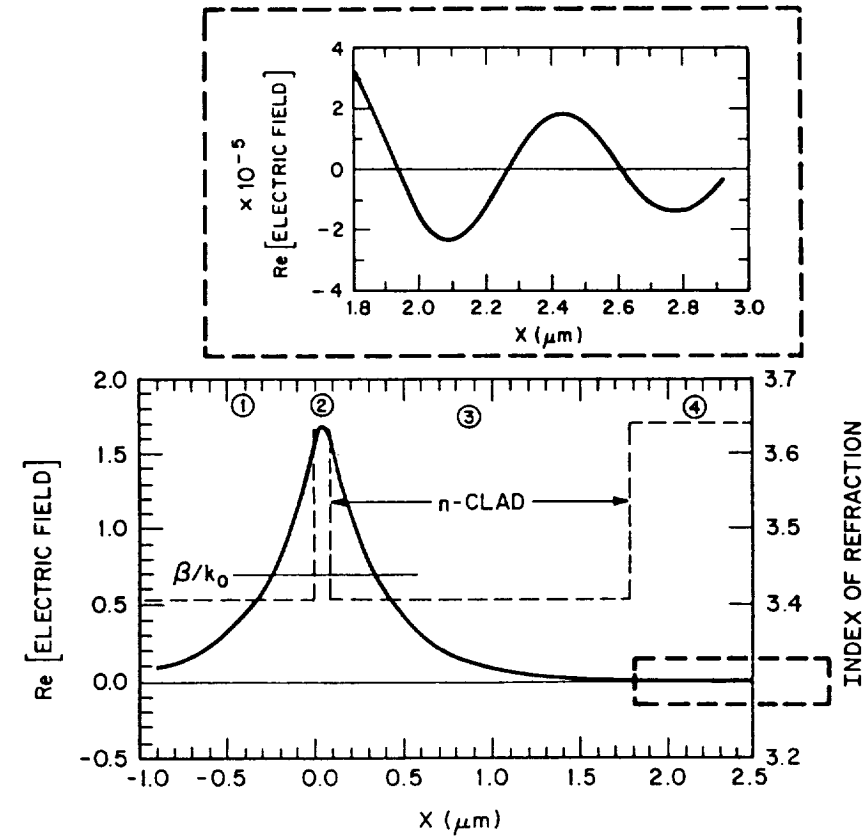


Figure 11(b)

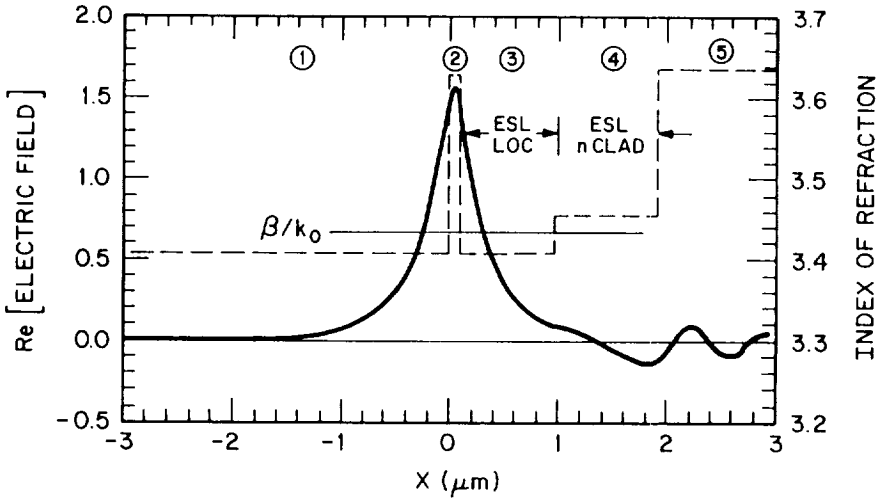


Figure 11(c)

Figure 11. Index profiles (---) and corresponding electric field distributions (——) for (a) a conventional CSP laser, (b) a CSP-LOC laser; and (c) an ESL-CSP laser. The layer compositions, thicknesses, and effective index for each structure are listed in Tables 1-3. The dashed rectangles in (a) and (b) show the field distributions on expanded scales for x > 1.8 μm.

The data in Fig. 10 indicates that the aluminum concentration is highest at the bottom of the channels. For this case, the computed effective perpendicular index profile is no longer that of a simple double-heterostructure (DH); it is that of a large optical cavity (LOC). Such a dielectric profile was introduced intentionally to lower the optical power density by producing a wider perpendicular near-field distribution than that of a conventional DH configuration [5]. In Fig. 12, the FWHP of the near-field intensity is plotted as a function of AlAs composition (or index at $\lambda$ = 0.83 μm) of the LOC layer assuming the AlAs mole fraction of the p- and n-cladding layer is 0.33 and that of the active layer is 0.07. The CSP-LOC FWHP near-field intensity of the fundamental mode reaches a maximum of about 0.4 μm (for a 0.4-μm-thick LOC layer) and 0.72 μm (for a 0.9-μm-thick LOC layer) at AlAs compositions of the LOC layer of about 18%. These curves are designed to indicate trends in behavior of the mode and do not consider, for example, higher order modes, which are possible in thick LOC layers.

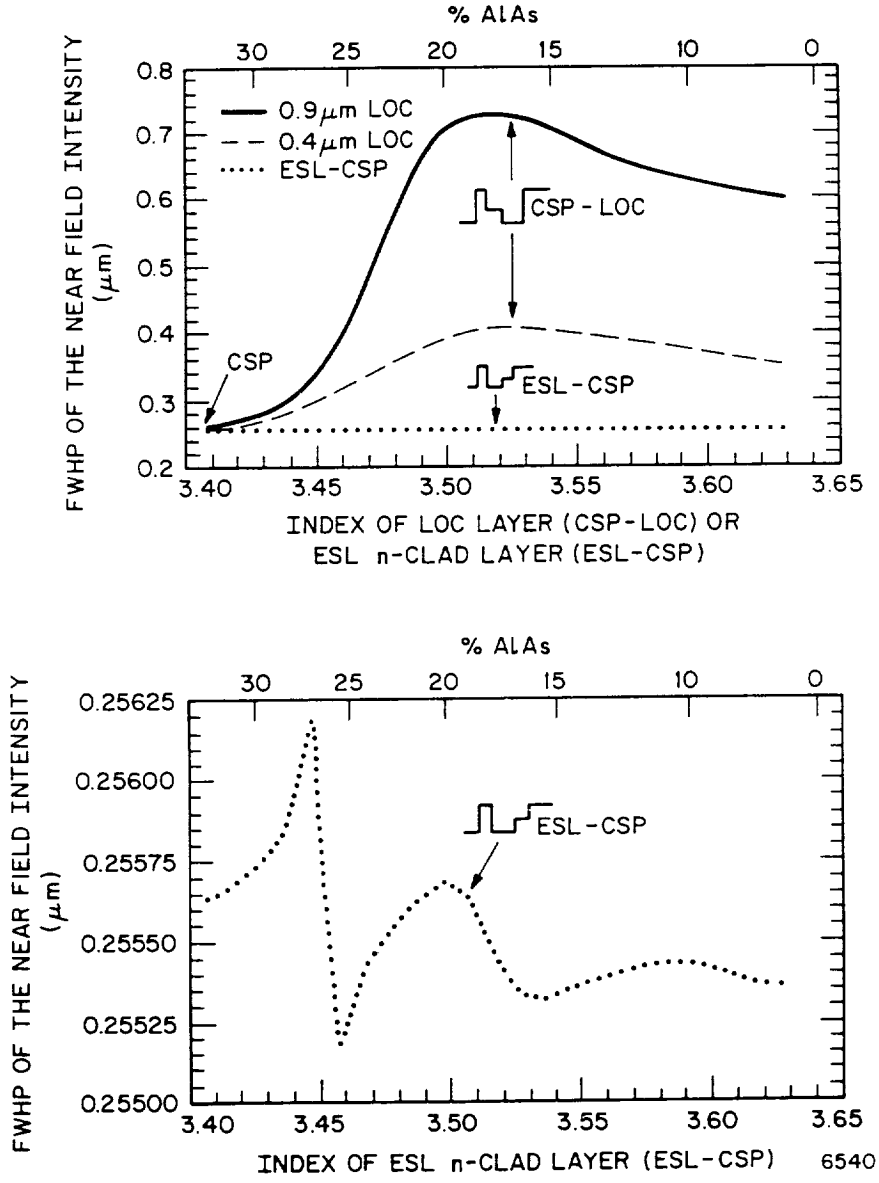


Figure 12. (a) Calculated near-field FWHP as a function of the % AlAs (or index of refraction at $\lambda$ = 0.83 μm) of a 0.4 μm (---) and 0.9 μm (——) thick LOC layer (CSP-LOC geometry) or of the 0.9 μm (·····) thick n-cladding layer (ESL-CSP geometry). The n-cladding layer for the CSP-LOC layer has an AlAs mole fraction of 0.33, and the LOC layer for the ESL-CSP has an AlAs mole fraction of 0.33. (b) The calculated near-field FWHP as a function of AlAs or index of refraction for the ESL-CSP structure on an expanded scale. The common point to all three curves (at an index value = 3.40657) corresponds to the conventional CSP laser described in Table 1.

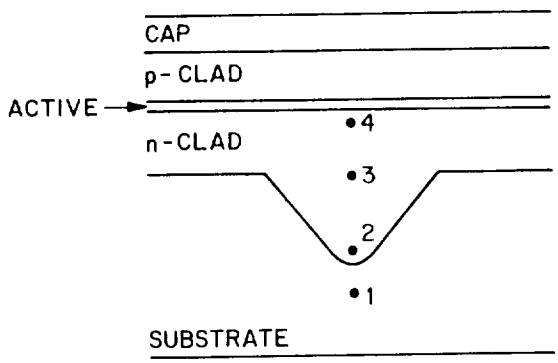


| FACET POSITION | COMPOSITION % Al | % Ga | % As |
|---|---|---|---|
| 1 | 0 | 50 | 50 |
| 2 | 14 | 35 | 53 |
| 3 | 20 | 29 | 52 |
| 4 | 18 | 32 | 52 |

Figure 13. Composition measured by Auger analysis at four positions along a cleaved facet of a CSP-type laser showing a lower aluminum composition near the bottom of the V-channel than near the top.

Some CSP structures examined also displayed lower Al concentrations at the bottom of the channel, which is opposite to our previous findings. Figure 13 shows a schematic drawing of the channel region of a CSP laser together with the Al concentrations, as given by AES data. The effective perpendicular index profile, displayed in Fig. 14, can be thought of as pulling some of the optical mode power into the substrate, thereby increasing the mode loss. This mechanism, which we call Enhanced Substrate Loss (ESL), can also be explained by realizing that all the modes supported by the index profiles are complex modes (i.e., the longitudinal and transverse wave vectors have a real and an imaginary component) because the field solutions to the electromagnetic wave equation [6] are sinusoidal in the substrate. Usually, the n-cladding layer separating the active region from the substrate is thick enough (>1 μm) that field penetration of the laser mode into the substrate is negligible. However, if the mole fraction of AlAs is lower at the bottom of the channel than at the top of the channel, the higher index portion in the channel acts as an anti-reflection coating between the high-aluminum, low-index portion and the no-aluminum, very-high-index substrate, thereby coupling or redistributing a larger fraction of the mode power into the substrate.

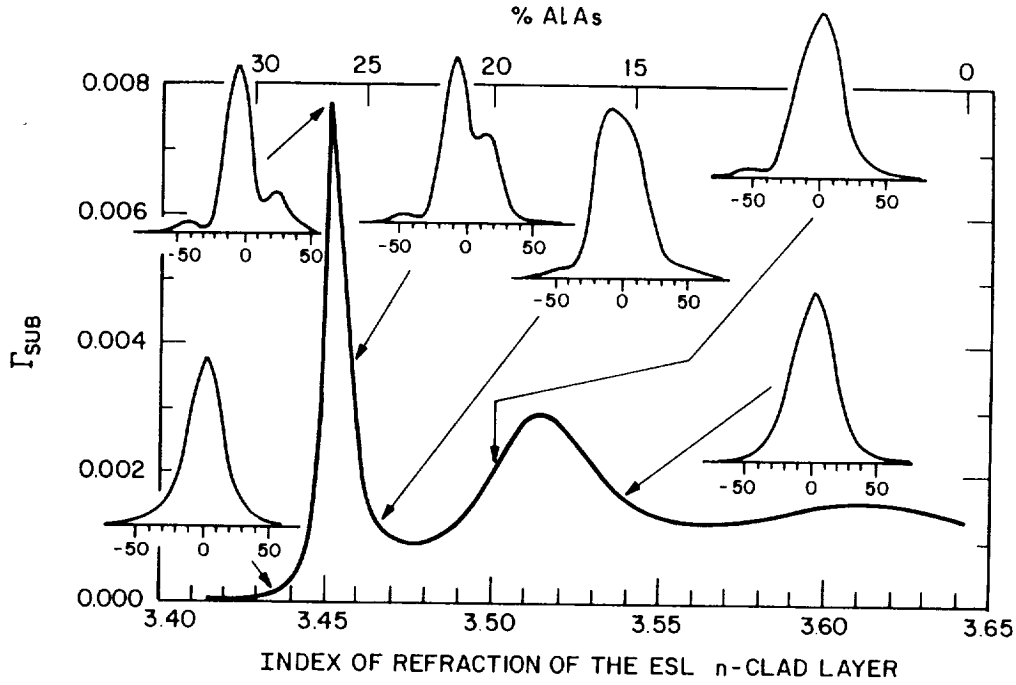


Figure 14. The substrate confinement factor, $\Gamma_s$, as a function of the % AlAs (or index of refraction at $\lambda$ = 0.83 μm) of the n-cladding layer at the bottom of the channel of an ESL-CSP laser. The inset far-field intensity vs angle patterns show a large variation in asymmetry as a function of % AlAs of the n-cladding layer.

The exact cause of a non-uniform Al/Ga ratio occurring within the channel region of a CSP laser during the growth of the first cladding layer is not fully understood. However, we do know that (1) layer growth must be faster at the bottom of the channel than at the top to obtain a planar surface, (2) both lateral and perpendicular growth components must be present within the channel, (3) the sidewall and bottom of the channel present different crystallographic planes for nucleation that are different from those above the channel, where the growth is planar, and 4) varying degrees of meltback may be present at the sidewalls and bottom of the channel. Any of these conditions can readily affect the composition of the ternary compound that initially nucleates and freezes out from the AlGaAs melt, and can alter this composition as the growth proceeds and overall growth conditions change. Furthermore, if the Al/Ga ratio changes during the initial growth, then changes in the local melt composition may occur, which might further change the Al/Ga ratio later in the growth process. Data from the AlAs-GaAs phase diagram shows that very small changes in the Al content in the melt produces very significant changes to the Al content in the grown material. The

basis for a non-uniform Al/Ga ratio within the channel of a CSP laser is also consistent with the variability of this effect from channel to channel since it would be the local conditions around each channel that would determine the magnitude of the effect. A more complete description of these abnormalities can be found in Appendix B of this report.

## C. LASER DIODE PROCESSING

In the wafer processing area, all aspects associated with the different processes (i.e., diffusion, metallization, photolithography, etc.) are closely monitored to maintain a high throughput yield. In addition, the processes are closely scrutinized periodically and changed as the need arises for improvements in both yield and process quality. One area that we examined was the effects of ion sputtering or milling of the emitting facets of the CSP lasers. The cleaved mirror facets of the CSP lasers contain native oxides, owing to the reactive nature of the aluminum alloys used in the growth of the structure and absorbed impurities (i.e., water, carbon, etc.) on the surface caused by various fabrication procedures. A pre-deposition cleaning using argon ion-beam milling should increase adhesion of the facet coatings (a problem that has plagued this process for years) and improve device reliability. The principal problem associated with the use of this milling or sputtering process is the damage that may result at the mirror facet of the laser. The exact point at which this cleaning procedure is a benefit and at which damage to the laser facets occurs was unknown. As a result, we implemented a study to determine all the variables associated with this process.

In this study, we used AES to quantify changes in the surface composition of the laser facets generated by the argon ion bombardment. Deviations from stoichiometry and surface-oxide removal rates were examined for argon ion current densities between 0.02 and 0.04 $mA/cm^2$ and ion energies in the range of 200 and 1000 eV.

The experiment was performed in a conventional cryo-pumped electron beam deposition system having a base pressure of $10^{-7}$ Torr. The ion source used was a broad beam type, and the physical constraints within the deposition chamber resulted in placement of the ion gun at an angle of 5° off the normal of the sample surface. The argon flow rate to the ion source was adjusted via a mass flow controller to yield an operating pressure of $10^{-4}$ Torr during the ion

milling process. A biased plasma probe with a grounded shield could be interchanged with the sample, thus enabling in situ measurements of the ion current density prior to actual sample exposure to the beam.

An AES system is attached to the electron beam system and kept isolated during the deposition process by a gate valve. A magnetically coupled feedthrough is used to transfer the samples between the two systems without exposure to the atmosphere. A schematic diagram of the combined electron deposition/AES system is shown in Fig. 15.

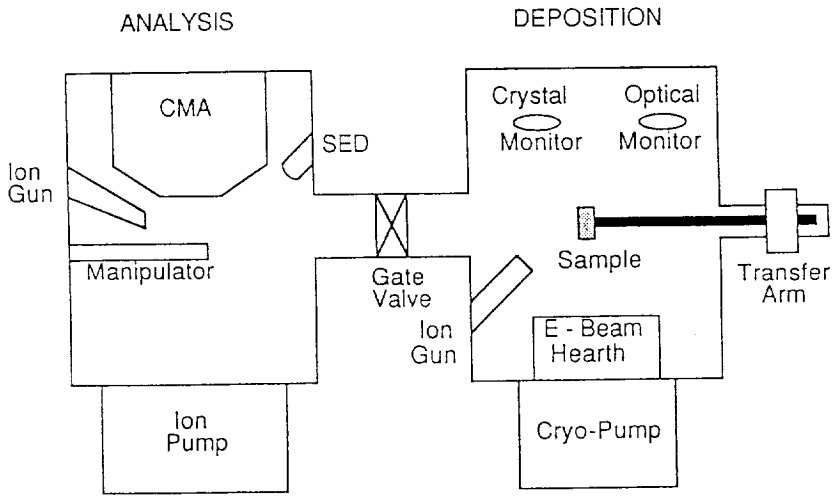


Figure 15. Schematic diagram of the combined electron beam deposition and Auger analysis system use for facet coating experimentation.

The CSP samples used in this investigation were cleaved in atmosphere, and no prior cleaning was employed prior to loading the samples into the deposition system. In all cases the samples were examined prior to cleaning and were subsequently examined at various stages during the argon ion-beam milling process. The only impurities observed on the sample prior to ion beam milling were carbon and oxygen. After milling, AES measurements revealed that the carbon had been completely removed, while trace amounts of oxygen still remained on the facet. The inability to completely remove oxygen is likely to be due to absorption of residual water in the deposition system prior to the transfer operation. Trace amounts of argon were also observed to be present after milling.

In Fig. 16, a plot of the normalized oxygen peak height vs the ion milling time for 1000-eV argon ions at three different ion current densities is shown. The rate at which the oxygen is removed from the facet is clearly proportional to the

ion current density, as was expected. Similar results have been obtained at ion energies between 200 and 1000 eV. An estimate of 10 Å for the native oxide thickness was determined based upon the ion milling rates of $Al_2O_3$ and $Ta_2O_5$ standards. The oxide removal rates, using this thickness, were approximately 1, 2, and 5 Å/min. for ion current densities of 0.02, 0.03, and 0.04 mA/cm$^2$, respectively. These results compare favorably with those observed by other researchers [7]. A complete description of this work can be found in Appendix C.

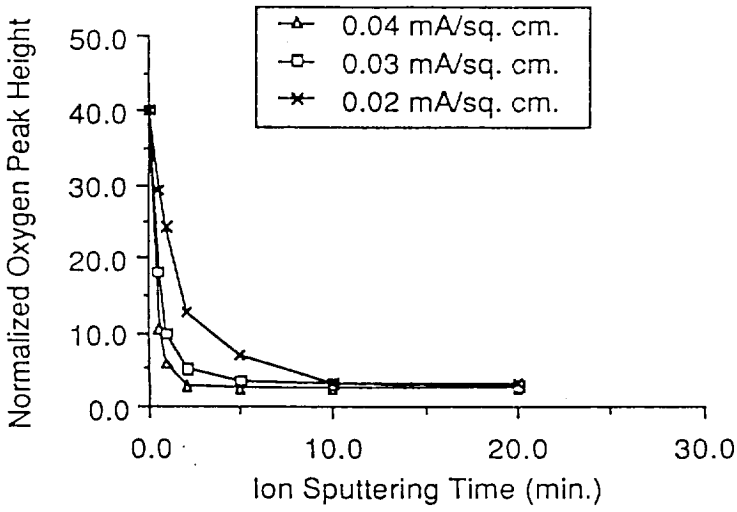


Figure 16. Removal rate of oxygen from the laser facet as a function of ion sputtering time using 1000-eV argon ions.

## D. LASER DIODE DIE AND WIRE MOUNTING

The problems associated with the use of indium solders are well known and documented. Thus, we have focused our attention on the development of fluxless mounting techniques incorporating hard solders. Some hard solders, such as tin, are subject to "whisker" growth; therefore, we concentrated our efforts using gold-based solder alloys (i.e., Au-Sn, Au-Ge, Au-Si, etc.). The soldering process is performed in a hydrogen/nitrogen environment to inhibit the formation of oxides during mounting. Analysis of devices on lifetest, using scanning electron microscopy (SEM) and energy dispersive analysis of x-rays (EDAX) after operating lifetimes in excess of 8,000 hours, have shown no evidence of the "whisker-type" growth that had previously been seen using tin-based solders.

The wirebond connection to the n-side of the CSP laser has also been examined. The first wirebond made to the CSP lasers was performed on a ball-type wirebonding machine. The smallest-diameter gold wire (0.007 in.) having

the lowest hardness value was used to minimize the amount of stress placed on the chip during the wirebonding process. The deformation of the ball and damage to the laser chip were evaluated using SEM and metallurgy cross-sectioning techniques. A series of experiments were conducted to fully assess the impact of the stress on the laser chip during the wirebonding process. A 3-gm pull-force value was used as the minimum acceptable bond strength. In almost all cases, damage to the laser chip was observed, owing to the force required in deforming the ball to obtain the minimum bond strength. Additional analysis revealed that the exact cause of the damage was not only associated with the wirebonding process but also with the poor quality of the wafer surface used for the wirebond. During the thinning procedure, this surface is lapped to remove the residual zinc diffusion and to reduce the wafer thickness for the subsequent cleaving process. Analysis of the lapped surface revealed damage to the GaAs crystal at depths up to 0.002 in. (total chip thickness after lapping is only 0.004 in.). During the wirebonding process, the stress placed on the chip during the deformation of the ball resulted in propagation of the defects associated with the lapping procedure into the laser chip. A modification to the thinning process using the standard lapping procedure in conjunction with a chemical etching procedure has not only reduced the damage associated with the lapping process but has dramatically improved the surface finish. This has lead to wirebonds exhibiting less damage with greater bond strengths. However, to ensure long-lived CSP lasers, it is necessary to eliminate all damage associated with this bond. This requirement leads us to investigate another bonding technique, called wedge bonding. This technique still requires deformation of a wire, but not of the large diameter ball. Thus, the forces necessary for deformation are greatly reduced. By utilizing our experience with the ball bonding process and applying it to the wedge-style bonding, we have been able to obtain bonds exhibiting the minimum bond strength without any observable damage to the CSP laser chip. Analysis of failed-lifetest devices after many thousands of hours of operation have shown no propagation of defects from the location of the wirebond to the laser structure.

In the CSP laser, the heat caused by operating the laser is generated along the contact stripe on the p side of the chip. The hottest location along that stripe, however, is near the emitting facets, where additional heat is generated due to strong optical absorption. Thus, heatsinking of the facets, particularly the output facet, is essential for reliable operation. The beam divergence of the CSP laser is quite large, which requires that the position of the output facet of the chip be at the

edge of the heatsink. Mechanically polishing this edge to the tolerance required for suitable heatsinking (radius <1 μm) is quite time-consuming and results in the incorporation of the polishing media into the oxygen-free high-conductivity (OFHC) copper mount (measurements performed using AES techniques). Thus, we have developed a broaching technique that leaves the corner of the OFHC copper mount with a radius of less than 1 μm and without any contamination on the mounting surface. In addition, the surface roughness or quality of the mounting surface by both techniques is comparable.

## E. LASER DIODE OPERATING CHARACTERISTICS

A CSP laser has been fabricated that has produced lasing operation to 190-mW-cw, single-fundamental-spatial and spectral-mode operation up to 70 mW cw, with single-spatial-mode operation continuing to 150 mW; beyond 70 mW there are increasing line-broadening effects in the parallel far-field patterns accompanied by the appearance and growth of spectral sidebands. We show in Fig. 17 the power output vs current input (P-I) curves, the spectral content of the output, and the parallel and perpendicular far-field radiation patterns at different power levels. The laser facets for these measurements were coated with an $Al_2O_3$/Si dielectric stack to produce 90% reflectance on the back facet and an approximate $\lambda/4$ $Al_2O_3$ layer to produce an approximately 10% reflectance on the front, or emitting, facet. The room temperature (23°C) cw threshold current is 48 mA and the differential quantum efficiency, $\eta$, at the emitting facet is 41%. The laser displayed a minor kink in the P-I curve at ≈70 mW of output power. The performance characteristics of the device remained unchanged over the entire power range including the kinked region. However, broadening of the lateral far-field radiation pattern, due to gain saturation and heating effects, could be observed at powers >100 mW. The wavelength shift is that expected from the bandgap shift due to joule heating and a 25°C/W mounted-diode thermal resistance. The beam FWHP at 20 mW for the parallel and perpendicular far-field patterns are, respectively, 6.5° and 27°. It is worth noting that, after failure at 190 mW cw, the laser facet visually showed no damage and the laser continued to be operable up to 120 mW cw.

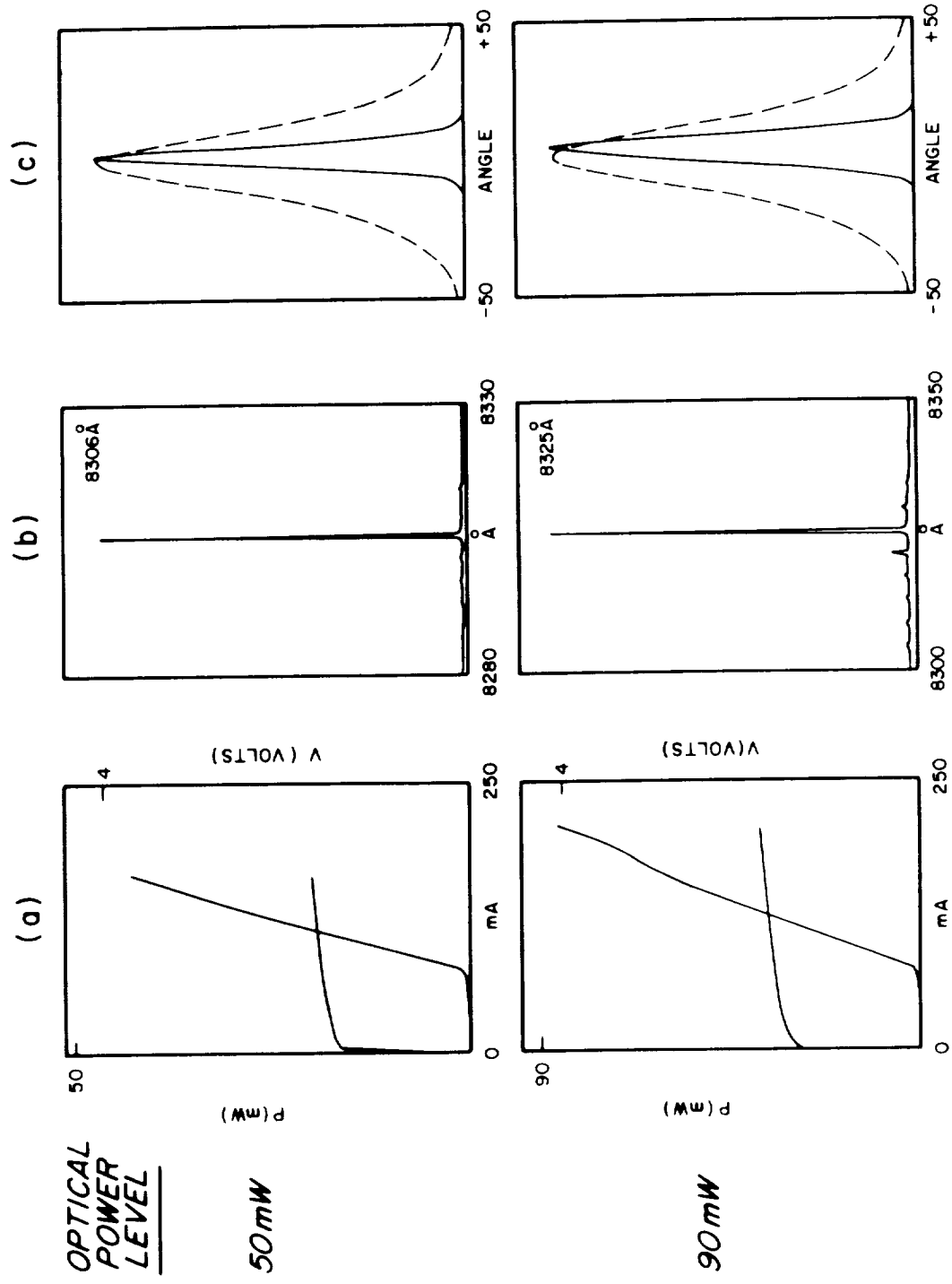
(a)
(b)
(c)
OPTICAL POWER LEVEL
50mW
90mW
P(mW)
V (VOLTS)
mA
ANGLE
8306Å
8325Å
0
Å
+50
-50
8280
8330
8300
8350
50
90
4
250

Figure 17(a).

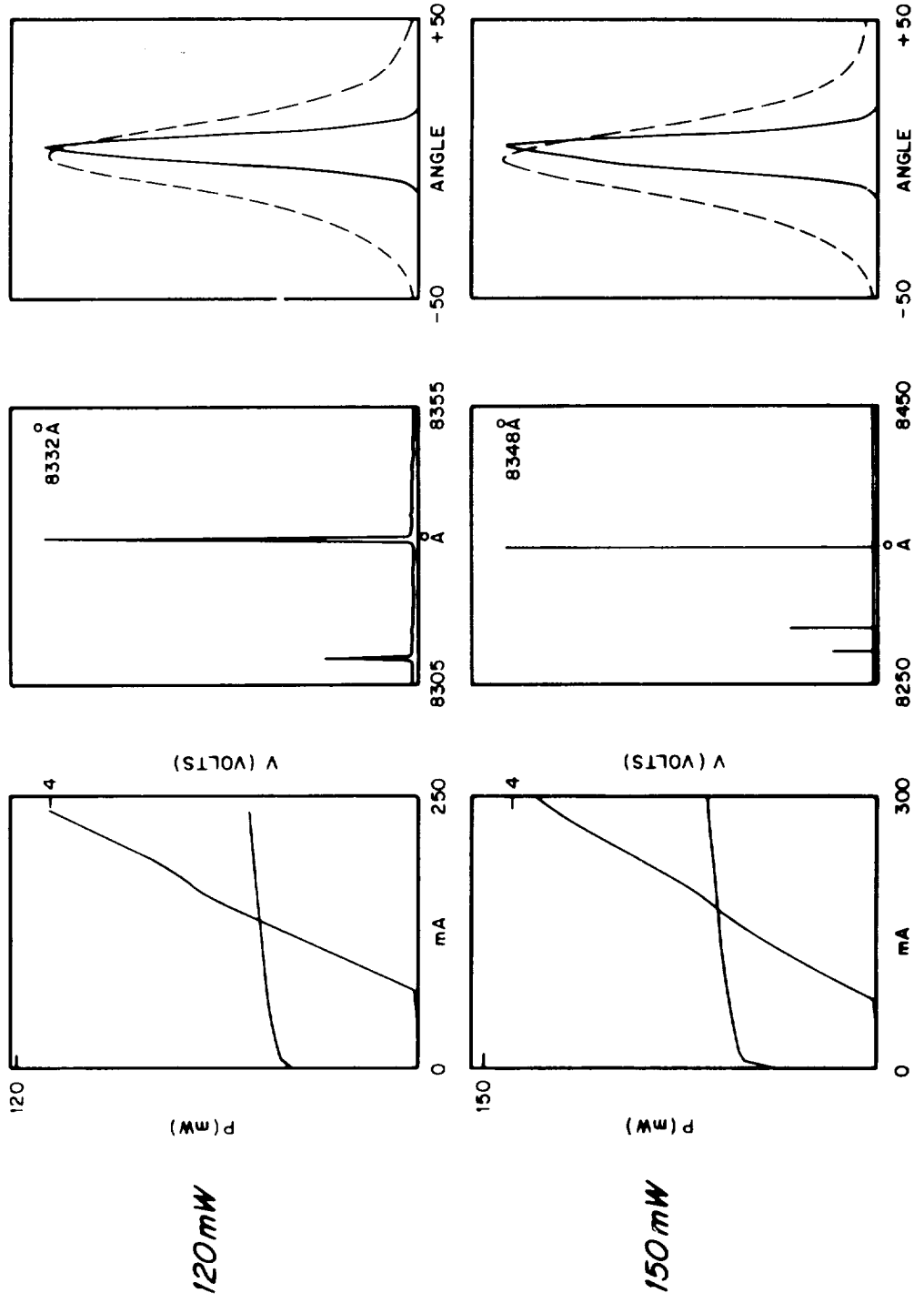


Figure 17(b).

Figure 17. Power output/current input (P-I) curves, spectrum, and far-field radiation patterns at various output power levels for a high-power CSP laser.

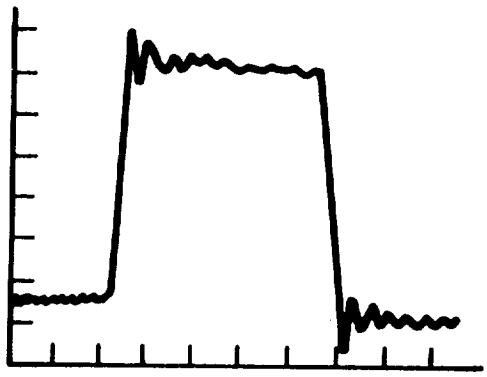

2 nsec/div
Current input pulse
10% duty cycle

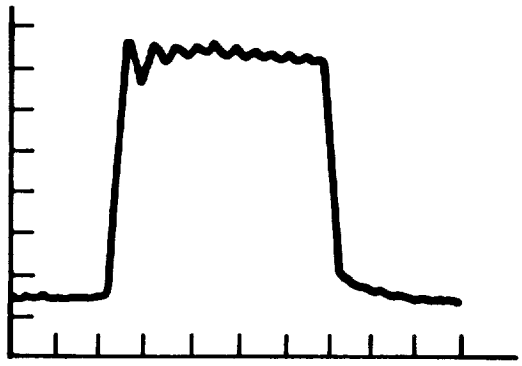

2 nsec/div
Peak pulse optical
output power = 60 mW

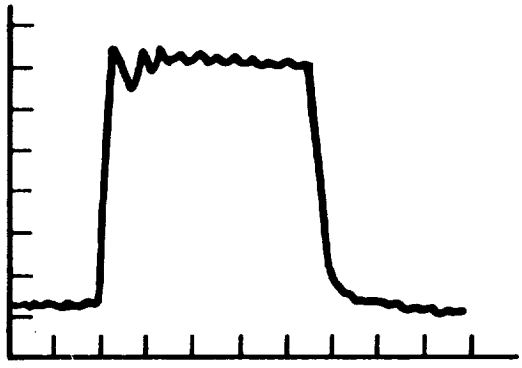

2 nsec/div
Peak pulse optical
output power = 80 mW

Figure 18. Response of a CSP high-power laser to square current pulses at 14% duty cycle. The fall and rise times are <0.5 ns.

Typical laser modulation behavior is indicated in Fig.18, in which we show the laser response to square current pulses at 14% duty cycle. The fall and rise times are <0.5 ns (the limit of the pulse resolution); note the almost complete absence of tailing in both the leading and trailing edges of the output pulse, as well as a minimum of ringing oscillation. Modulation properties were found not to change at power levels up to 80 mW, the limit of the experiment.

## F. LIFETESTING AND RELIABILITY ASSURANCE

Semiconductor lasers, such as the CSP lasers, only operate in the lasing mode at rated power up to about 100°C. Thus, there is little margin above the normal maximum operating temperature to carry out fully operational lifetests that can be used to obtain traditional Arrhenius extrapolations. As a consequence, we use detailed measurements of the change in drive current for rated power at operating temperatures of 25°C, 50°C, and 70°C. Previous studies [12] have shown that the change in threshold current and drive current could be described by a power law of the type

$$\frac{\partial I}{I} = At^n$$

where $0 < n < 1$. By fitting this expression to the characteristics of the aging parameter, the predicted change can be determined. All the CSP lasers were tested using a constant power technique in which the drive current used to power the device is continually adjusted to maintain rated output power. This technique subjects the devices to a greater operational stress than the constant current technique in which the laser is placed on lifetest at rated power and the decrease in output power is monitored.

A total of 15 CSP lasers were placed on lifetest; 8, 4, and 3 at operating temperatures of 25°C, 50°C, and 70°C, respectively. In all cases the operating conditions were 50 mW at a 50% duty cycle and at a repetition rate of 10 MHz. The threshold currents for all the devices were below 80 mA, and the initial thermal resistances were between 20°C/W and 40°C/W. The lasers were mounted p-side down on a copper heatsink and had ($\lambda/4$) $Al_2O_3$ coating with a reflectance of 10% on the emitting facet and a ($\lambda/4$) $Al_2O_3$/Si stack coating having a reflectance of 90% on the rear facet. The devices all operated in the fundamental mode and had emission wavelengths between 8600 and 8800 Å. The devices were not subject to a

preselection burn-in process prior to placement on lifetest. The devices placed on lifetest were taken from three different LPE growth runs that displayed operational characteristics of suitable quality for use in the ACTS program.

As shown in Fig. 19, all eight devices placed on lifetest at 25°C are continuing to lase after 1000 to 1500 h on lifetest. In most cases only a modest increase in drive current was required to maintain the rated power of 50 mW. CSP lasers removed during the lifetesting process and re-characterized exhibited no change in the far-field radiation patterns or spectral characteristics, and only a small change was observed in the threshold current value. The invariance in the far-field pattern means that the lasing spot remains unchanged.

In Fig. 20, we show the results of four CSP lasers placed on lifetest at 50°C at 50 mW. In addition, we have included a projected lifetime for the lasers if an activation energy of 0.07 eV is assumed. Two of the devices have not required any change in drive current after 500 and 800 h, respectively. The other two devices have required large changes in drive current, which would be unacceptable in the ACTS program. Although these devices are considered unacceptable, the projected lifetimes of the devices still exceed 6,000 h, more than 3 times the estimated lifetime expected at the beginning of this program.

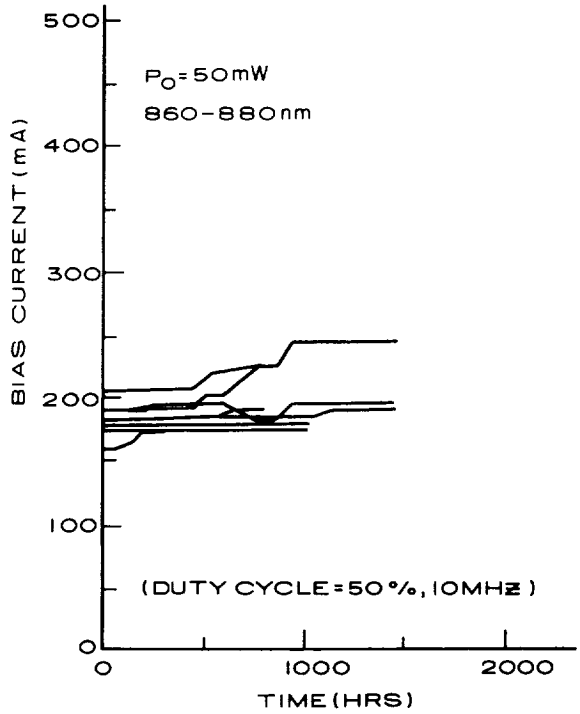


Figure 19. Aging behavior of high-power, 8600- to 8800-Å CSP lasers at 25°C as a function of operating time. The lasers were maintained at a constant output power level of 50 mW (50% duty cycle; 10 MHz).

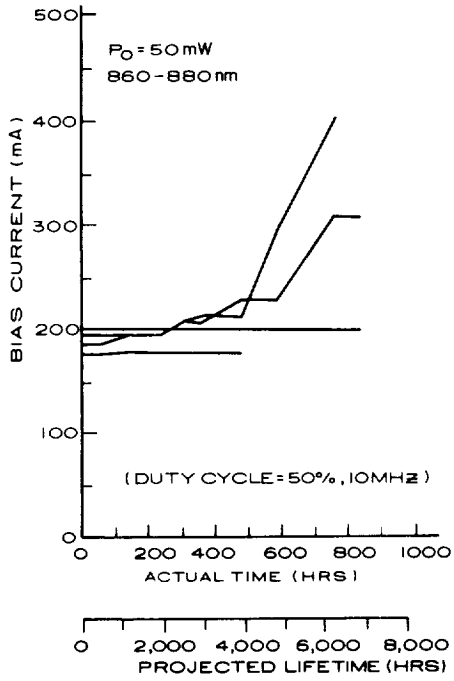


Figure 20. Aging behavior of high-power, 8600- to 8800-Å CSP lasers at 50°C as a function of operating time. The lasers were maintained at a constant output power level of 50 mW (50% duty cycle; 10 MHz).

The results of the three devices placed on lifetest at 70°C and 50 mW are shown in Fig. 21. As before, we have included a projected lifetime scale for these devices, assuming an appropriate activation energy. One of the devices placed on lifetest started to degrade immediately and most probably should not have been used. However, even with this rapid degradation, its usable life was in excess of 5,000 h, as predicated from our projected lifetime value. The other two devices degraded in a similar manner and are still operating after 450 h on lifetest. Although these lifetests are continuing, if we assumed they were completed at this point, the projected lifetimes for these devices would exceed 17,500 h, a value that would be acceptable for ACTS-type devices. This value translates to approximately two years of usable life if the devices were used on a continuous basis. If the devices were used intermittently, their lifetimes would be commensurate to the time they were in operation.

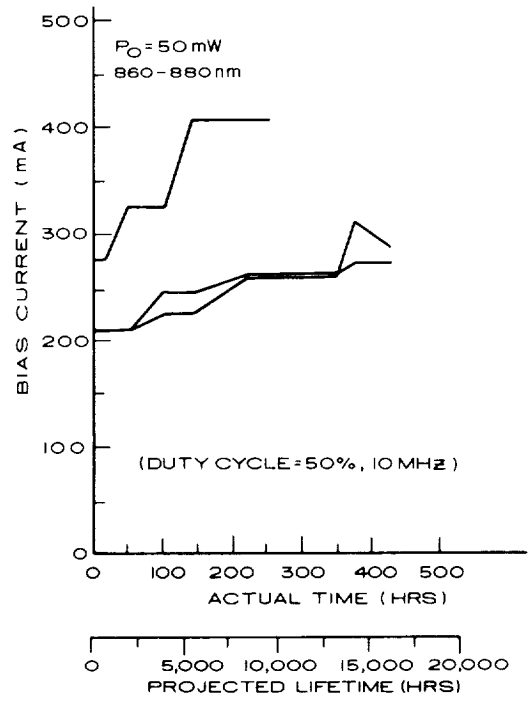


Figure 21. Aging behavior of high-power, 8600- to 8800-Å CSP lasers at 70°C as a function of operating time. The lasers were maintained at a constant output power level of 50 mW (50% duty cycle; 10 MHz).

## G. POST-LIFE FAILURE ANALYSIS

The examination of failed devices is critical to the development of new techniques and processes that will ultimately lead to CSP lasers that exhibit high reliability and long life. The analysis of a failed device is not a straightforward process, owing to the inherent small size of the laser chip and the even smaller geometry of the laser structure. Thus, many of the routine analytical techniques had to be modified so that the analysis on the small laser chip could be performed.

The diffusion of zinc into the CSP structure is an important part of the fabrication procedure. It provides the high carrier concentration necessary for good ohmic contact and confines the current to the lasing region of the device. In addition, the position of the zinc front determines the gain profile for the laser. Analysis of devices on lifetest revealed that some of the devices from different LPE growth runs whose near-field radiation pattern prior to lifetesting displayed a single lobe that had changed to a two-lobe far-field after failure in lifetesting. In Fig. 22(a) and (b) the near-field radiation patterns for a CSP laser before and after

lifetest are shown. We refer to the reduced intensity in the center of the near-field pattern of Fig. 22(b) as a node. The devices that exhibited these effects were examined using angle lapping techniques in an attempt to identify the common physical feature that would account for the observed effect.

In almost all the devices we examined with this observe defect, the common feature was the position of the zinc front in the structure to that of the active layer. In some cases the zinc front that we delineated using a chemical etchant had actually penetrated into the active layer, while other devices displayed a front in very close proximity to the active layer. The deep zinc diffusion region is not composed of a uniform concentration of zinc. Analysis of this region by secondary ion mass spectroscopy (SIMS) has shown that the leading edge of the zinc region may be one to two orders of magnitude lower in carrier concentration than the surface. Thus, delineation by chemical etching techniques may not reveal the actual position of the zinc front, but instead identify a specific carrier concentration at which the etching process is activated. However, SIMS studies have shown that the actual misplacement between the zinc and the etched fronts is <1000 Å. Thus, for our analyses here we can assume that both fronts are at the same location. The evidence linking the position of the zinc front to a change in the near-field pattern suggests that the two are related.

Previous work by other researchers [8-10] suggests that a highly doped, zinc-diffused region is a potential source of defects that form non-radiative recombination centers that degrade the lifetimes as well as the performance of laser diodes. A nonradiative recombination region in the active layer of the device will result in no light being emitted from the area. Thus, devices with the zinc front penetrating into the active layer will display near-field radiation patterns containing two lobes, each lobe corresponding to a lasing spot on either size of the nonradiative region. A process change has been implemented to eliminate this problem in the future. This change involves growing a thicker p-cladding layer (from 1 to 1.5 μm) in the CSP structure and maintaining the zinc front, as delineated by a chemical etchant, at least 0.5 μm from the active layer. Devices meeting these critical parameters have been placed on lifetest, and no change in the near-field radiation pattern has been observed after many thousands of hours on lifetest. The complete details of this study can be found in Appendix E.

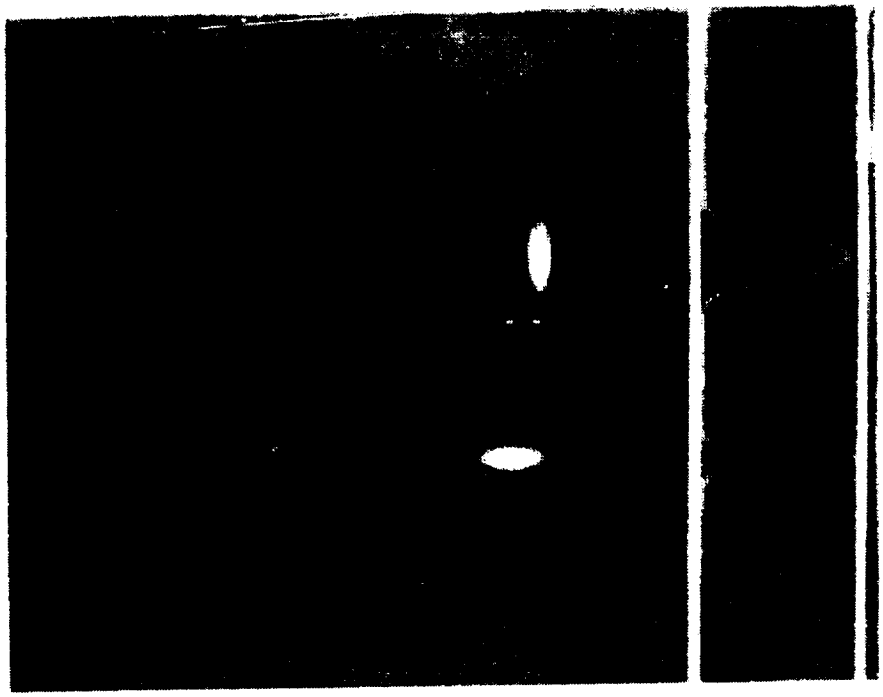

5 μm

(a)

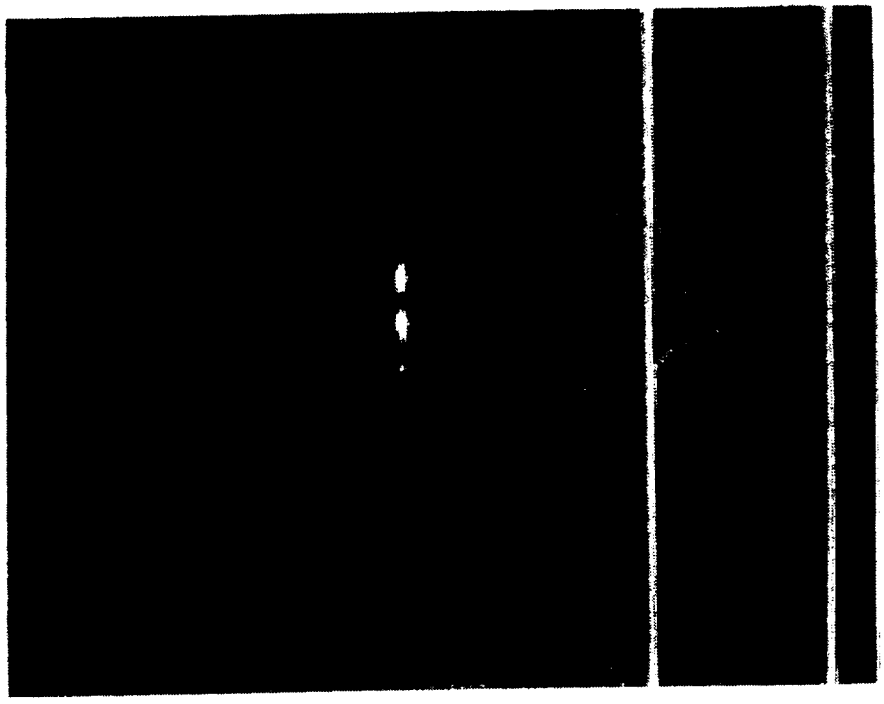

5 μm

Figure 22. (a) Pre-lifetest, near-field pattern and light-intensity scan for high-power CSP laser. (b) Post-lifetest, near-field pattern and light-intensity scan for the same CSP laser.

# III. LASER PERFORMANCE OF A DFB-CSP LASER

The goal of this phase of the program was the development of a high-power CSP laser that operates in a stable, single-longitudinal mode. Our approach to achieving this single-longitudinal-mode behavior is the introduction into the CSP structure of an additional feature rather than merely relying on the reproducibility of those elements that produce the laser's wave-guiding properties. To achieve stable operation at a single wavelength, a grating will be incorporated directly into the CSP structure, making it a distributed-feedback, channeled-substrate planar (DFB-CSP) laser. This grating, whose geometrical properties are determined from the laser's planned wavelength and refractive index, can be built directly into the CSP structure. The periodic grating instead of the mirror facets will now provide the feedback to support lasing. The feedback via the grating should produce a device with stable, single-longitudinal-mode operation even under 100% depth modulation conditions as well as providing improved temperature dependence of the longitudinal mode (0.7 Å/°C for DFB-CSP vs 3 Å/°C for standard CSP). In addition, since the feedback for lasing is provided by the grating, this type of structure should be much less susceptible to instabilities in the longitudinal-mode behavior, owing to light being reflected back into the lasing cavity from various components (i.e., lenses, beam splitters, fibers, etc.) in the optical system.

## A. DEVICE MODELING

In conventional lasers, the optical feedback is provided from a pair of reflecting surfaces that form a Fabry-Perot cavity. In a DFB laser, optical feedback is provided from a Bragg-type diffraction grating. In DFB lasers the grating is usually produced by corrugating the interface between two of the semiconductor layers that comprise the laser. This corrugation provides 180° reflection at certain specific wavelengths, depending on the grating spacing.

The basis for selective reflection of certain wavelengths can be understood by examining the original case considered by Bragg [11], in this case, the reflection of an incident plane wave by the atomic planes of a crystalline lattice. However, the same effect is observed in the case of reflection from a corrugated grating formed in the junction plane of a laser. To maintain the phase coherence of the plane wavefront and thereby avoid destructive interference, the path lengths

for reflections from successive reflectors must differ by an integral number of full wavelengths. Thus, from geometrical considerations, we obtain the Bragg relation given by

$$2d \sin\theta = \ell\lambda, \quad \ell = 1, 2, 3,...,$$

where $\theta$ is the angle formed by the incident ray and the atomic planes, and $\lambda$ is the optical wavelength in the medium. To adapt this relationship to the case of 180° reflection by a grating in a DFB laser, it is only necessary to let d equal the grating spacing $\Lambda$, let $\lambda$ equal $\lambda_0/n_g$, where $n_g$ is the effective index in the waveguide for the mode under consideration, and let $\theta$ equal 90°. Under these assumptions the equation above becomes

$$2\Lambda = \ell(\lambda_0/n_g), \quad \ell = 1, 2, 3, \ldots .$$

The vacuum wavelength of light that will be reflected through 180° by such a grating is therefore

$$\lambda_0 = 2\Lambda n_g/\ell, \quad \ell = 1, 2, 3, \ldots .$$

Although the grating is capable of reflecting many different longitudinal modes, corresponding to the various values of $\ell$, usually only one mode will lie within the gain bandwidth of the laser. In fact, because of the difficulty of fabricating a first-order (i.e., $\ell = 1$, $\Lambda \approx 1200$ Å) grating, usually a second-order grating is used in most DFB-type structures.

The change in lasing wavelength as a function of heatsink temperature for a DFB laser can be calculated if the principal of operation is understood. The wavelength shift in a DFB laser results from a change in the Bragg condition due to changes in both the index of refraction and in the grating period. Since the fractional change in index with temperature is about an order of magnitude greater than the thermal expansion coefficient, only the former need be considered.

In a DFB laser, the lasing wavelength is locked by the grating's Bragg wavelength, given by

$$\lambda_B = 2n\Lambda/\ell$$

where n is the effective index, and $\ell$ and $\Lambda$ are the grating order and period, respectively. Differentiating this equation with respect to temperature yields

$$\frac{d\lambda_B}{dT} = \frac{1}{n_g}\left[\lambda_B\left(\frac{\partial n}{\partial T}\right)\right]$$

where $n_g$, the "group" index is given by

$$n_g = n - \lambda\left(\frac{\partial n}{\partial \lambda}\right)$$

and $d\Lambda/dT$ is assumed small. For an AlGaAs laser operating at 8300 Å, $n_g$ is ≈4.2 (from the Fabry-Perot mode spacing). Thus, for

$$\lambda_B = 8300 \text{ Å and } \partial n/\partial T = 3.5 \times 10^{-4} \text{ °C}^{-1}$$

we find that the wavelength change with temperature should be about 0.7 Å/°C.

In addition to providing a means of accurately selecting the peak emission wavelength, grating feedback also results in a narrower linewidth of the optical emission. The spectral width of the emission line is established by a convolution of the laser gain curve with the mode-selective characteristics of the laser cavity. Since the grating is much more wavelength-selective than a cleaved facet, the resulting emission linewidth of a DFB laser is significantly less than that of Fabry-Perot laser. The emission linewidth of a DFB laser depends strongly on the coupling coefficient k of the grating. Decreasing the operating temperature also decreases emission linewidth, because the gain curve of the laser is narrowed as the thermal distribution of electron energies is decreased.

## B. GRATING FABRICATION AND LPE/MOCVD GROWTH TECHNIQUES

A schematic of the structure is shown in Fig. 23(a) and in the stained cross-sectional cleave in Fig. 23(b). The details of the structure can be seen more clearly in Fig. 23(c), in which we show a stained cross-section lapped at a 1° angle in the vertical direction. The substrate is prepared by chemically etching a second-order grating using a photoresist mask obtained by standard holographic interferometry into a 0.8-μm-thick, n-type $Al_{0.15}Ga_{0.85}As$ layer. A 0.12-μm-thick

GaAs layer is then grown over the grating. These layers are grown using metalorganic, chemical-vapor deposition (MOCVD) for improved uniformity and surface morphology. The MOCVD growth also improves the nucleation of the GaAs layer on the $Al_{0.15}Ga_{0.85}As$ grating surface. The $Al_{0.15}Ga_{0.85}As$ layer prevents layer meltback of both the V-channel and the grating, while the GaAs layer grown over the grating, provides a nucleating surface during subsequent LPE growth. In Fig. 23(c) some nucleation problems are still evident with the MOCVD grown GaAs layer. The index step at the grating interface is approximately 0.1.

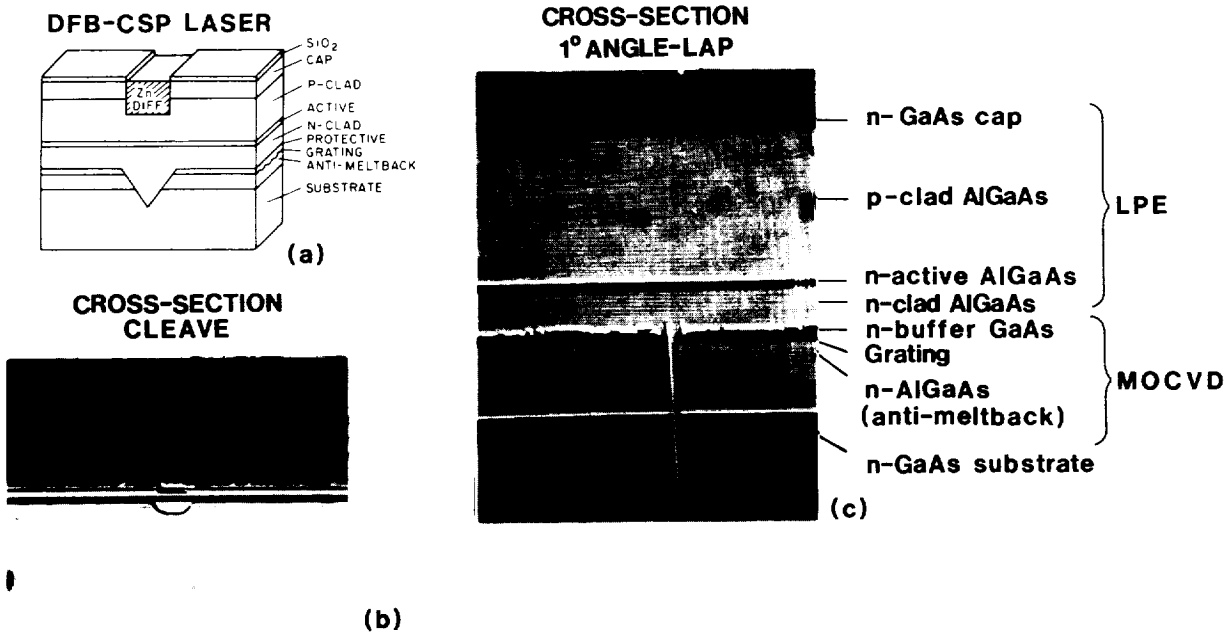


Figure 23. (a) Schematic diagram of CSP-DFB laser. (b) Stained cross-sectional cleave of CSP-DFB structure. (c) Stained cross-sectional cleave lapped at a 1° angle in the vertical direction. Note especially the beginning of meltback between the n-cladding and n-buffer layers.

The LPE growth is performed in the automated LPE growth reactor, as described in the LPE growth of CSP lasers section of this report. The MOCVD was performed in Cambridge Instruments' MR-100 system at atmospheric pressure. It contains four metal alkyls and three hydride sources for the growth of AlGaAs compounds. The gas-handling system has been designed to give abrupt interfaces (<10 Å) so that quantum-well-type structures can be routinely grown. Under computer control, the gas flows and growth temperature may be ramped, making

it possible to grow graded-interface structures and devices that require graded doping profiles as well. The horizontal cell configuration allows the thickness and compositional uniformity over a 2-in. wafer to be better than 10%. The typical background doping and mobilities in GaAs are ~$10^{14}$ $cm^{-3}$ and 7500 $cm^2$/V-s at 300 K and 80,000 $cm^2$/V-s at 77 K. A photograph of the system is shown in Fig. 24.

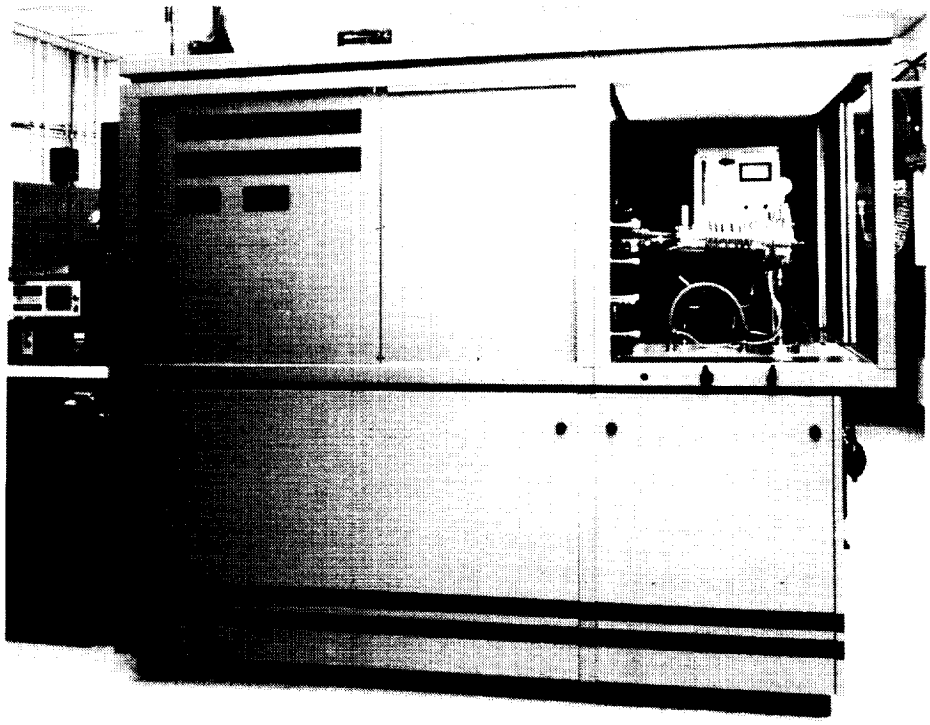

Figure 24. Photograph of metalorganic chemical vapor deposition (MOCVD) system used for the epitaxial growth of the DFB-CSP laser.

After the grating, which is formed using chemical etching techniques, and its protective layers have been fabricated, a 4.2-μm-wide V-channel is chemically etched into the substrate and four layers are grown: (1) $Al_{.33}Ga_{.67}As$ cladding layer (0.3 μm, $N_d = 1 \times 10^{18}$ $cm^{-3}$), (2) $Al_{0.06}Ga_{0.94}As$ active layer (0.07 μm, $N_d = 1 \times 10^{17}$ $cm^{-3}$), (3) $Al_{0.33}Ga_{0.67}As$ cladding layer (1.5 μm, $N_a = 5 \times 10^{17}$ $cm^{-3}$), 4) GaAs capping layer (0.7 μm, $N_d = 5 \times 10^{17}$ $cm^{-3}$). The growth is performed at 800°C, using a cooling rate of 1°C. This procedure significantly reduces the complexity of fabricating the DFB-CSP structure. In addition, the current path in the device does not include a regrowth interface, which has been associated with higher-than-normal series resistance for devices fabricated with one or more growth

interfaces in the current flow path. After LPE growth, routine contacting technology completes the device, which includes Zn stripe diffusion for current-confinement, Ti/Pt/Au for the p-contact, and AuGe/Ni/Au for the n-contact.

Upon closer inspection of fabricated structures, we have found that the chemically etched gratings used in our structure were relatively shallow (~100 Å) and displayed non-uniformities across the surface of the wafer. Both the shape and the depth of the grating should be considerably improved by the use of our newly acquired Commonwealth Scientific ion-beam etching system. This system can be operated in three different modes: first, conventional ion-beam etching, second, reactive ion-beam etching, and third, ion-beam-assisted etching. Conventional ion-beam etching isotropically removes material from a sample as a result of bombarding it with inert gas ions. In the reactive ion-beam etching mode, a reactive gas is used in place of the inert gas to add a chemical etching component to the process. Ion-beam-assisted etching uses an inert gas ion beam while a "blanket" of reactive gas is maintained at the sample surface. In this case, the sample is not only chemically etched, but it is also protected from high-energy ions that can cause crystalline damage.

The improvement in the quality of the grating using ion-beam etching can be clearly seen from Figs. 25 and 26. In Fig. 25, a cross-sectional scanning electron micrograph (SEM) of a grating prepared using chemical etching techniques is shown. The grating is etched along the dovetail direction in the GaAs substrate since the CSP structure is fabricated along the V-direction. Thus, shallow gratings (200 to 300 Å) are obtained, owing to the undercutting action of the preferential etchant. This undercutting limits our ability to fabricate deep gratings, which are required to enhance feedback and suppress Fabry-Perot operation. In addition, a more complex photolithographic process is required for chemically prepared gratings as opposed to ion-beam-etched gratings. This photolithographic process leads to nonuniform linewidths in the submicron grating pattern. These problems have led to the development of a grating procedure incorporating ion-beam etching techniques.

A cross-sectional micrograph of an ion-beam-etched grating in a GaAs substrate is shown in Fig. 26. The increased grating depth and sharply defined mesas can be clearly seen in the photograph. The grating was fabricated using a beam voltage of 300 eV and a current density of 0.7 $mA/cm^2$ at an incidence angle of 30°.

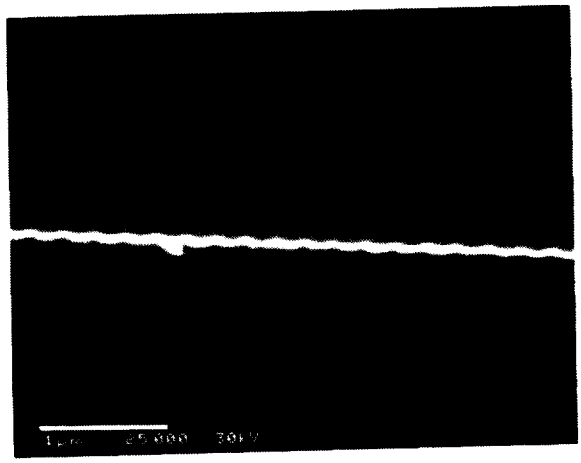

Figure 25. A grating with a 2400-Å period formed in an AlGaAs layer by chemical etching techniques.

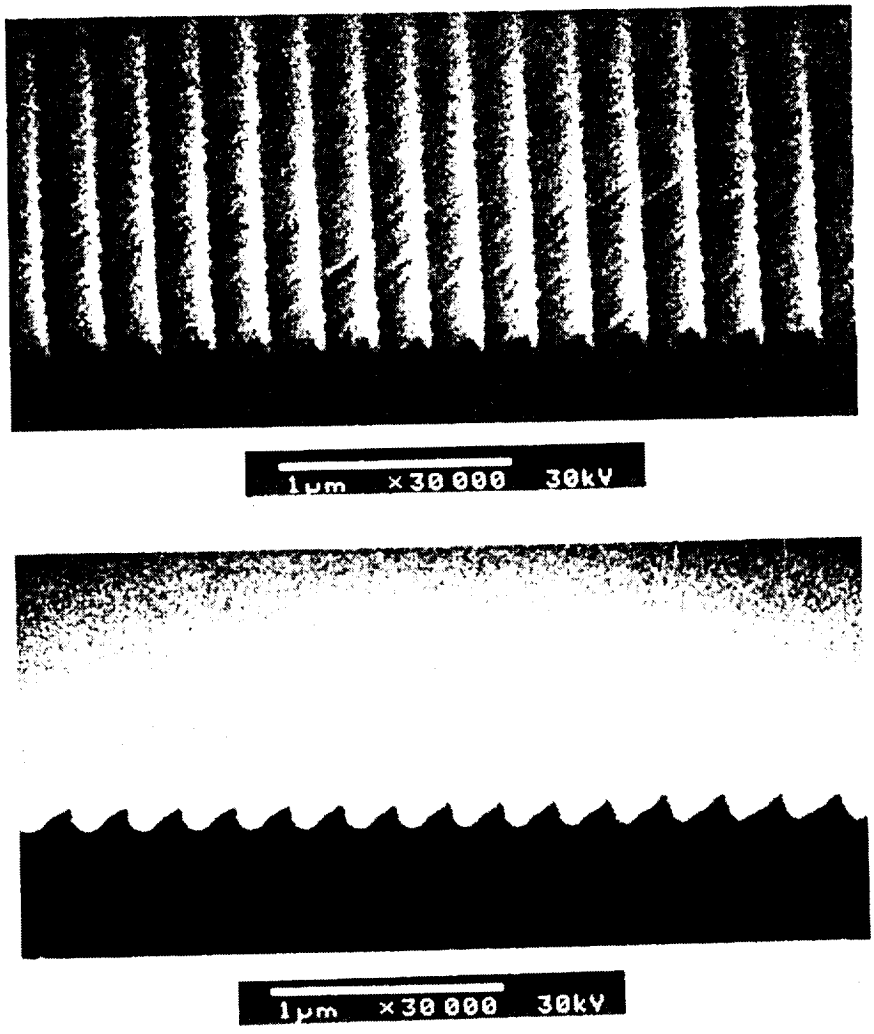


Figure 26. A grating with a 2400-Å period formed in an AlGaAs by ion-beam milling techniques.

Although we have been able to fabricate DFB-CSP lasers using the techniques described above, we are still plagued with nucleation non-uniformities and low yield. As a consequence, a series of wafers were grown with ion-beam-milled gratings on the shoulders of the V-channel. The grating was fabricated into a 0.6-μm-thick $Al_{0.12}Ga_{0.88}As$, layer and a GaAs layer was grown over the grating using MOCVD techniques. The period of the grating was chosen based upon emission wavelength spread obtained from previous LPE growths. All the wafers grown displayed some non-uniform nucleation across the growth surface. The growth in the channel region appeared normal, while the surrounding areas showed various stages of growth. Analysis using angle-lapping techniques revealed a problem at the interface between the grating and the GaAs protective overgrowth layer. Further investigation on the LPE substrates identified that the GaAs layer was non-contiguous.

A growth study was then conducted to determine the cause of the non-contiguous film. A set of wafers containing gratings fabricated into a MOCVD grown $Al_{0.12}Ga_{0.88}As$ layer were prepared for this study. Very thin GaAs layers (100 to 1000 Å) were grown on top of the grating and cross-sectional samples were examined using a SEM. The samples showed that unlike conventional MOCVD growth, the re-growth layer does not necessarily follow the previous surface morphology in all situations. Figure 27(a) shows an SEM cross-sectional photograph of an ion-beam-milled grating in a GaAs substrate. The grating has a period of 2400 Å, a value comparable with the period in our device structures, and a depth of 1200 Å. The slight waviness at the edges of the grating is an artifact of the SEM used to take the photographs. Figures 27(b) and 27(c) show the same grating milled into 14% and 23% AlAs but with AlGaAs and GaAs grown over top of the grating. For the case of a thin $Al_{0.40}Ga_{0.60}As$ layer grown on top of the grating (Fig. 27b), the layer follows the periodic nature of the grating replicating its shape. On the other hand, when a thin GaAs layer is grown over top of the grating milled in $Al_{0.23}Ga_{0.77}As$ (Fig. 27c), the layer fills in only the valleys of the gratings. This results in a surface composed of GaAs and $Al_{0.23}Ga_{0.77}As$. This type of surface makes the growth of a layer on top by LPE very difficult since the nucleation process will normally be incomplete across a large area due to the exposed $Al_{0.23}Ga_{0.77}As$ regions. Thus, for obtaining complete nucleation of the surface by LPE growth techniques, it is necessary that the valleys in the grating be filled until coalescence of the GaAs material in the

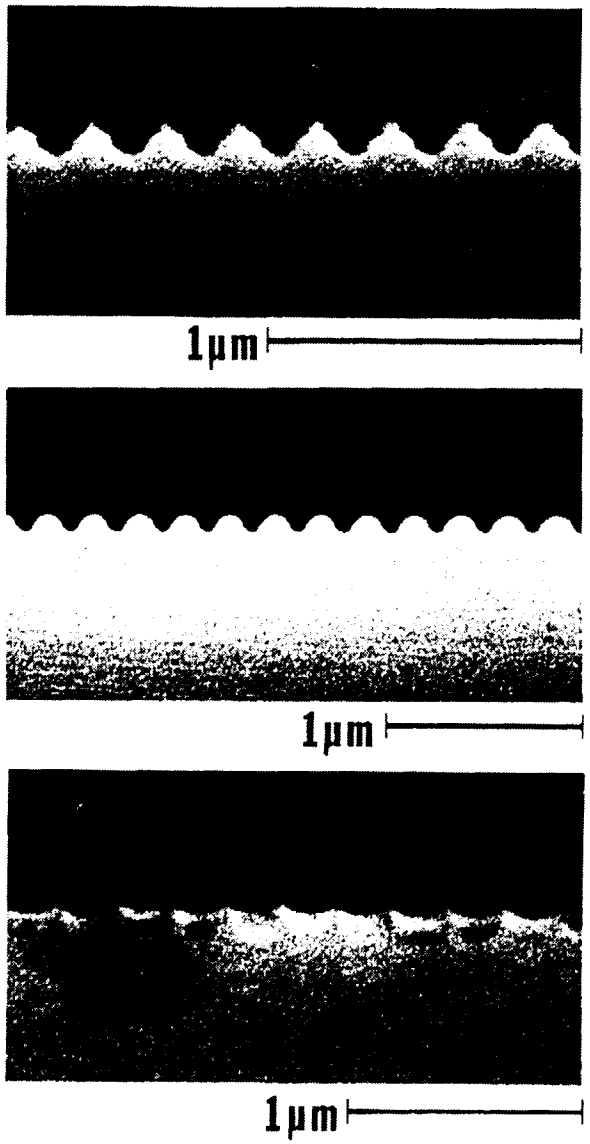


Figure 27. (a) An SEM cross-sectional photograph of an ion-beam-milled grating in a GaAs substrate. (b) An SEM cross-sectional photograph of an ion-beam-milled grating in a 14% AlAs with a 40% AlAs layer grown on top by MOCVD. (c) An SEM cross-sectional photograph of an ion-beam-milled grating in 23% AlAs with GaAs grown on top by MOCVD.

valleys occurs above the peaks of the grating. This coalescence will ensure uniform nucleation during the subsequent LPE growth process.

## C. LASER DIODE OPERATING CHARACTERISTICS

Theoretically, successful DFB action should be indicated by two lines in the output spectrum. In practice, however, only one line is most often seen because of non-uniformities or asymmetries in the Bragg scattering or reflections in the Fabry-Perot cavity. Thus, the significant indication of DFB action is that the spectrum of light output contains one line, indicating a single longitudinal mode, that remains essentially fixed with no mode-hopping over a range of power and temperature for both cw and pulsed operation. This wavelength can, in fact, change with operating conditions, such as power and temperature, but it changes largely according to temperature-induced changes in the effective index, which can be predicted theoretically (see modeling section). The mode remains locked by the grating rather than determined by the properties of the Fabry-Perot cavity, and changes observed are those stemming from the grating.

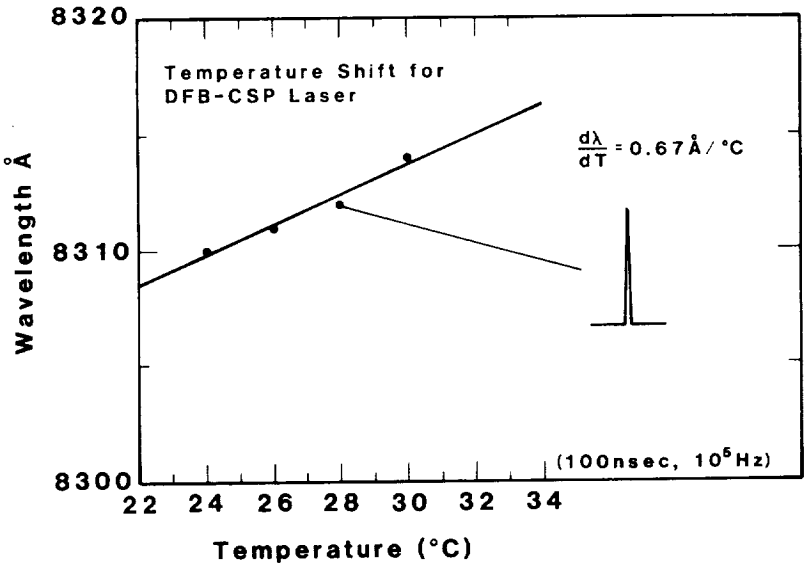


Figure 28. Emission wavelength shift as a function of heatsink temperature for a CSP-DFB laser operating pulsed at an output power of 10 mW.

The CSP-DFB laser displayed DFB operation at pulsed (1% duty cycle; 100 ns) power levels up to 40 mW and at cw power levels up to 10 mW. Figure 28 shows the change in the single-longitudinal-mode spectrum for a DFB-CSP laser operating over the temperature range of 24°C-32°C. The pulsed output power from

the device was maintained at 10 mW. The facets of the device were coated (front-10%; rear-85%), and no attempt was made to suppress the Fabry Perot modes. Sideband rejection ratios are in the range of 18 to 23 dB. The observed pulsed spectra were characteristic of DFB lasers in that they remained single-line for all temperatures [6]. A typical pulsed spectrum for this device operating at 28°C can be seen in Fig. 28. The wavelength temperature dependence for both pulsed and cw operation is about 0.7 Å/°C. This behavior is that expected for an AlGaAs laser of the given composition and layer thickness operating at 8300 Å [7]. The fact that the DFB behavior described above occurs over a relatively small temperature range and at powers only up to 40 mW pulsed can be associated with the small grating depth (~100 to 200 Å) produced by chemical etching in the dovetail direction.

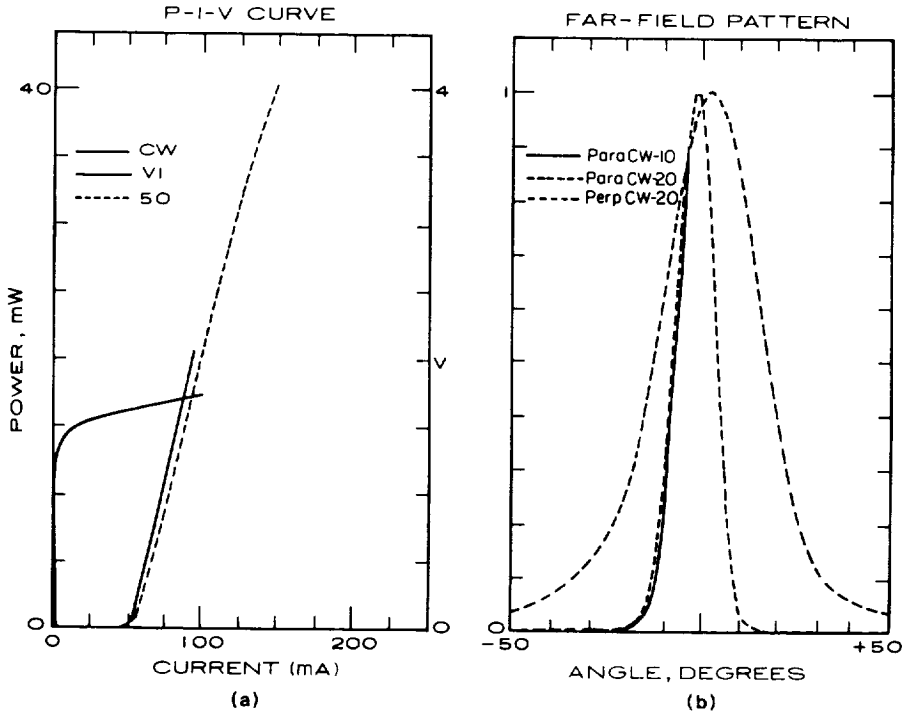


Figure 29. (a) Power-current curves for a CSP-DFB laser. (b) Far-field radiation patterns for a CSP-DFB laser.

Figures 29(a) and (b) show the P-I curve and far-field patterns, respectively, demonstrating thresholds as low as 50 mA, kink-free power curves, and well-defined, single-spatial modes. The overall efficiency of the laser at 40 mW (total input electrical power divided by output optical power) is 15%. Thus, incorporation of the grating and the accompanying extra layers (see Fig. 23) do

not interfere with the desirable spatial mode and high-power properties of the basic CSP structure. A more complete description of the results can be found in Appendix F.

# IV. CONCLUSIONS

The continued support of the high-power CSP laser by NASA has led to significant improvements in both the performance levels and reliability of the device at wavelengths (8600 to 8800 Å) previously thought unattainable. These results are important because the transparency of the atmosphere in this wavelength regime makes possible optical communication links for space-to-ground systems. Advances in LPE growth and computer modeling techniques has resulted in the fabrication of lasers operating at record high-power levels. In addition, these device improvements have led to overall improvements in reliability both in terms of output power and operating lifetimes. Further work is still necessary, however, to develop laser sources to meet the critical requirements for space applications. Both higher power capability and reliability improvements are necessary for the realization of a spaceborne laser communication system.

As AlGaAs lasers continued to be used in a wider range of applications, it has become increasingly apparent that control of the longitudinal mode will be necessary to avoid mode-hopping and instabilities in the output of the laser due to optical feedback. The development of the DFB-CSP lasers addresses these issues. This novel structure has demonstrated stable longitudinal-mode operation over an 8°C temperature range at pulsed powers up to 40 mW. However, if a laser device is to be incorporated into space-qualified systems, more work needs to be performed. Some of the specific areas that need to be explored are the incorporation of the grating in the peak of the optical mode, improved grating fabrication, and the development of new growth techniques to extend the usable power and temperature range.

## REFERENCES


1. D. B. Carlin, M. Ettenberg, N. A. Dinkel, and J. K. Butler, "A high-power channeled-substrate-planar AlGaAs laser," Appl. Phys. 47, 655-667 (1 October 1985).

2. G. A. Evans, J. K. Butler, and V. Masin, "Lateral optical confinement of AlGaAs channeled-substrate-planar lasers," IEEE Journal of Quantum Electronics, QE-24 (5), 737-749 (May 1988).

3. J. K. Butler, G. A. Evans, and B. Goldstein, "Analysis and performance of channeled-substrate-planar double-heterostructure lasers with geometrical asymmetries," IEEE J. Quantum Electron, QE-23 (11), 1890-1899 (November 1987).

4. J. J. Hsieh, "Thickness and surface morphology of GaAs LPE layers grown by supercooling, step-cooling, equilibrium-cooling, and two-phase solution techniques," J. Crystal Growth 27, 49 (1974).

5. H. Kressel and J. K. Butler, Semiconductors Lasers and Heterojunction LEDs, Chapter 7, Section 5 (Academic Press, New York, 1977), pp. 230-234.

6. K. Aiki, M. Nakamura, T. Kuroda, J. Umeda, R. Ito, N. Chinone, and M. Maeda, "Transverse mode stabilized $Al_xGa_{1-x}As$ injection lasers with channeled-substrate-planar structure," IEEE J. of Quantum Electron., QE-14 (2), 89-94 (Feb. 1978).

7. S. P. Kowalczyk, J. R. Waldrop, and R. W. Grant, "Interfacial chemical reactivity of metal contacts with thin native oxides of GaAs," J. Vac. Sci. Technol., 19 (3), 611 (1981).

8. I. Ladany and H. Kressel, "Influence of device fabrication parameters on gradual degradation of AlGaAs cw laser diodes," Appl. Phys. Lett. 25 (12), 708 (15 December 1974).

9. I. Ladany and H. Kressel, "GaAs and related compounds, 1974," Inst. Phys. and Phys. Soc., Conf. Ser. No. 24, London, pp. 192, 1975.

10. H. Kressel and J. K. Butler, Semiconductors Lasers and Heterojunction LEDs, Chapter 7, Section 5 (Academic Press, New York, 1977), pp. 543.

11. R. G. Hunsperger, Integrated Optics Theory and Technology, Chapter 13 (Springer-Verlag, New York, 1985), pp 215.

12. D. Botez, J. C. Connolly, M. Ettenberg, D. G. Gilbert, and J. J. Hughes, "Reliability of constricted double-heterojunction AlGaAs diode lasers," Appl. Phys. Lett., 43 (2) (15 July 1983).

# Appendix A

# A SELF-CONSISTENT ANALYSIS OF GAIN SATURATION IN CHANNELED-SUBSTRATE-PLANAR DOUBLE-HETEROJUNCTION LASERS*

by
Jerome K. Butler** and Gary A. Evans
David Sarnoff Research Center
CN 5300
Princeton, NJ 08543-5300

## ABSTRACT

A self-consistent model for semiconductor lasers (using the CSP-DH laser structure as an example) which does not assume constant optical power along the laser axis is developed. This approach allows for the analysis of high power lasers with low facet reflectivities which produce nonuniform photon densities along the propagation direction. Analytical equations for the modal gain coefficient, the threshold current density, and (for facet reflectivities > 0.2) the radiated power for a specific CSP laser structure are obtained.

*This work was supported in part by NASA, Langley Research Center, Hampton, Virginia under Contract Number NAS1-17441.

**Southern Methodist University, Dallas, TX 75275.

# A SELF-CONSISTENT ANALYSIS OF GAIN SATURATION IN CHANNELED-SUBSTRATE-PLANAR DOUBLE-HETEROJUNCTION LASERS*

by
Jerome K. Butler** and Gary A. Evans
David Sarnoff Research Center
CN 5300
Princeton, NJ 08543-5300

Semiconductor lasers with high reflectivity facets (> 0.3) have an almost uniform density of photons along their longitudinal axis, allowing the assumption of uniform gain in their analysis. However, the highest power from a semiconductor laser is achieved by using a high reflectivity end facet and a low reflectivity (0.05 to 0.1) output facet resulting in large variations of the photon density along the cavity axis[1-4]. In this paper we extend a recent uniform (longitudinal) gain analysis[5] based on the "self-consistent model". This extension, which allows for photon density variations along the longitudinal axis, results in relatively simple phenomenological equations for the modal gain coefficient, the threshold current density, and (in the limit of high facet reflectivities) the radiated power.

In self-consistent models the carrier density in the active layer is derived from a solution of the diffusion equation having both source and sink terms. The source for the injected carriers is the drive current, whereas the sink is the stimulated recombination. The current flow into the active layer varies laterally and lateral carrier diffusion within the active region affects the optical gain profile modifying the shape of the optical field distribution in the laser diode.[6-14] The spatial dependence of the recombination term is computed from the product of the lateral gain profile and the photon density in the active layer as a function of position along the longitudinal axis.

*This work was supported in part by NASA, Langley Research Center, Hampton, Virginia under Contract Number NAS1-17441.

**Southern Methodist University, Dallas, TX 75275.

For wave propagation of the form $\exp(j\omega t - \gamma z)$, the transverse electric field polarized along y can be solved using the effective index method; it is written as

$$E_y = E_0\, u(x,y)\, v(y) \exp(-\gamma z) \tag{1}$$

where the complex function u(x,y) determines the transverse field shape along x, but it is slowly varying (along y) compared to v(y) which defines the lateral field profile. The nonlinear differential equation for the lateral field v(y) satisfies

$$\frac{d^2v}{dy^2} + [\gamma^2 - \gamma_0^2 + k_0^2 \Gamma_c(y)\, \kappa_a(y,P_a)]\, v = 0 \tag{2}$$

where $\Gamma_c(y)$ is the complex confinement factor and $k_0$ is the free-space wavenumber. The complex effective index of refraction is $n_{eff} = -j\gamma_0(y)/k_0$ and $\gamma_0(y)$ is found from the solution of the transverse problem. The value $\kappa_a(y,P_a)$ is the carrier dependent part of the dielectric constant in the active layer and $P_a$ is the optical power in the active layer. In terms of the active layer gain $g(y,P_a)$, the dielectric perturbation can be expressed as

$$\kappa_a(y,P_a) = n_a\, g(y,P_a)(2R + j)/k_0 \tag{3}$$

where $n_a$ is the passive index of the active layer and R is the gain induced index suppression coefficient.

The carrier distribution in the active layer must be found from solutions of the inhomogeneous diffusion equation having both "source" and "sink" terms. The source term is $R_{pump} = J_x(y)/qd_a$, where $J_x(y)$ is the current density, q is the electronic charge, and $d_a$ is the active layer thickness. For typical stripe geometry laser structures with Zn diffusion fingers, the lateral variation of the current density can be fit to the simple analytic formula[15]

$$J_x(y) = \begin{cases} J_0 & ;|y| < S/2 \\ \dfrac{J_0}{[1+(|y| - S/2)/y_0]^2} & ;|y| > S/2 \end{cases} \tag{4}$$

where $J_0$ is the current density under the stripe; $y_0$ is primarily a function of the Zn diffusion depth, the stripe contact width, and the resistivities of the various epitaxially

grown layers. Further, the injected current density is assumed to be invariant with z. The sink term is $R_{st} = P\,\Gamma(y)\,|v|^2\,g(y,P_a)$ where P is the intracavity power, $\Gamma(y)$ is the intensity confinement factor of the active layer, and $|v|^2$ is normalized to unity over $(-\infty,\infty)$.

The diffusion equation governing the pair density N(y) is

$$D_e \frac{d^2N}{dy^2} - \frac{N}{\tau_s} - B\,N^2 = -R_{pump} + R_{st} \qquad (5)$$

where $D_e$ is the effective diffusion coefficient, $\tau_s$ is the carrier lifetime, and B is the bimolecular recombination coefficient. The gain coefficient is $g(y,P_a) = aN(y) - b$ where $a = 2.5 \times 10^{-16}$ cm$^2$ and $b = 190$ cm$^{-1}$. In general, the stimulated recombination term $R_{st}$ will be functionally dependent on z. However, we have neglected carrier diffusion along the longitudinal direction since $|\partial N/\partial z| << N/L_D$, where $L_D$ is the carrier diffusion length.

At a given point z, the intracavity power $P(z) = P^+(z) + P^-(z)$ is the sum of the forward and backward waves. The power in the active layer $P_a$ is computed from a fraction of the intracavity power P. In lasers with high facet reflectivities, the intracavity power is almost constant along the z direction, however, when reflectivities are small, P(z) has relativity large changes along the axis. The modal power gain coefficient $G = -2\,\mathrm{Re}\{\gamma\}$ is computed from the self-consistent solutions of the carrier diffusion and Maxwell's equations.

Solutions of the optical fields of the CSP-DH structure with the material parameters shown in Fig. 1 are obtained with an index supression coefficient R = -2. The parameters used in the diffusion equation are $L_D = \sqrt{D_e\tau_s} = 3$ μm, $\tau_s = 3$ ns, $B = 10^{-10}$ cm$^3$/s, the stripe width S = 6 μm, and $y_0 = 0.5$ μm. The points in Fig. 2 show numerically computed values of the modal gain coefficient as a function of the intracavity power for different values of drive current which has been normalized for a laser length L = 100 μm.

Although the numerical data can be used to calculate the longitudinal variation of the gain in a laser with known facet reflectivities, it is useful to fit the numerically calculated modal gain coefficient points to an analytical expression (motivated by the form of the equation for gain saturation in homogeneously and inhomogeneously broadened systems)[16] written as

$$G(P) = \left(\frac{I}{I_0}\right)^c \frac{G_0}{(1 + P/P_s)^d} - \alpha_l \qquad (6)$$

where c, d, $G_0$, $P_s$, and $\alpha_l$ are unknown constants. An optimization procedure for a least-squares fit of (6) to the computed values of the self-consistant model gives c = 0.708, d = 0.687, $G_0$ = 51.4 /cm, $P_s$ = 41.2 mW, and $\alpha_l$ =49.6 /cm. (The value of $I_0$ is arbitrary but we used $I_0$ = 10 mA for the computed $G_0$ above. Note that $G_0$ and $I_0$ can be combined to form a single constant.) The resulting gain curves for these parameters are also illustrated in Fig. 2. It is interesting to note that the value of c is not unity due to the fact that bimolecular recombination is significant. The value of d is unity for a classical two-level system which is broadened homogeneously, whereas, it is 1/2 for an inhomogeneously broadened laser. $P_s$ is the saturation power and $\alpha_l$ is the modal loss coefficient in the absence of gain. At threshold, the intracavity power P = 0, and the threshold current is

$$I_{th} = I_0\left(\frac{G_{th} + \alpha_l}{G_0}\right)^{1/c} \qquad (7)$$

where $G_{th} = (1/2L)\ln(1/R_1R_2)$, and $R_1$ and $R_2$ are the facet reflectivities. In the event the reflectivities are high, the intracavity power is almost constant along z and the gain $G \approx G_{th}$. The emission power from the $R_1$ facet is is obtained from (6)

$$P_{rad} = P_s\left(\frac{1-R_1}{1+R_1}\right)\left[\left(\frac{I}{I_{th}}\right)^{c/d} - 1\right] \qquad (8)$$

This is just the expression for the emission power versus drive one would obtain for uniform photon densities. When one or both of the facet reflectivities is small, the intracavity power varies considerably along the laser axis and must be computed from the integral equation

$$P(z) = P_0\left[\exp\left(\int_0^z G(P)\,dz'\right) + \frac{1}{R_2}\exp\left(-\int_0^z G(P)\,dz'\right)\right] \qquad (9)$$

where $P_0$ is an eigenvalue, facet 2 lies at $z = 0$ and facet 1 lies at $z = L$. The boundary condition on G(P) requires its integral over the length of the cavity be $1/2\ \ln(1/R_1R_2)$.

Figure 3 shows the results for a laser with $L = 250\ \mu m$ and an emission power, $P_{rad} = 50$ mW. The back facet has a reflectivity $R_2 = 1$, and the output facet reflectivity $R_1$ is treated as a parameter. (The threshold current can be computed using Eq. (7).) When the output facet reflectivity is 0.3, P is almost constant along the laser axis; however, for $R_1 = 0.05$, the intracavity power varies from about 24 mW at $z = 0$ to about 55 mW at $z = L$. Figure 4 shows power versus current for the different reflectivities.

In conclusion we have developed the self-consistent model for semiconductor lasers (using the CSP-DH laser structure as an example) without assuming constant optical power along the laser axis. The advantage of the present approach allows for the analysis of lasers (typically high-power) with small facet reflectivities which produce nonuniform photon densities along the propagation direction. Generally, the hole burning effects will be larger at the output facet because the optical density is highest there. Further, hole burning is nonuniform in the direction of propagation. However, in long contemporary lasers these nonuniformities are slow compared to the carrier diffusion length. We also have developed analytical equations for the modal gain coefficient, the threshold current density, and (in the limit of high facet reflectivities) the radiated power for a specific CSP laser structure.

The authors wish to thank R. Amantea, M. Ettenberg and M. Lurie for many helpful technical discussions.

# REFERENCES


1. G. P. Agrawal, W. B. Joyce, R. W. Dixon, and M. Lax, Appl. Phys. Lett., 43, 11, 1983.
2. R. Baets and P. E. Lagasse, Electron. Lett. 20, 41, 1984.
3. P. Meissner, E. Patzak, and D. Yevick, IEEE J. Quantum Electron. QE-20, 899, 1984.
4. R. Baets, J. P. van de Capelle, and P. E. Lagasse, IEEE J. Quantum Electron. QE-21, 693, 1985.
5. J. K. Butler, G. A. Evans, B. Goldstein, IEEE J. Quantum Electron. (to be published in November 1987).
6. J. Buus, IEEE J. Quantum Electron., QE-15, 734, 1979.
7. W. Streifer, D. R. Scifres and R. D. Burnham, Appl. Phys. Lett. 37, 877, 1980.
8. W. Streifer, D. R. Scifres and R. D. Burnham, IEEE J. Quantum Electron. QE-17, 1521, 1981.
9. W. Streifer, D. R. Scifres and R. D. Burnham, IEEE J. Quantum Electron. QE-17, 736, 1981.
10. M. Ueno, R. Lang, S. Matsumoto, H. Kawano, T. Furuse, and I. Sakuma, IEE Proc., 129, Pt. I, 218, 1982.
11. S. Wang, C. Y. Chen, A. S. Liao, and L. Figueroa, IEEE J. Quantum Electron. QE-17, 453, 1981.
12. K. A. Shore, Opt. and Quantum Electron. 15, 371, 1983.
13. G. P. Agrawal, IEEE J. Lightwave Technol. LT-2, 537, 1984.
14. J. Buus, IEE Proc. 132, 42, 1985.
15. R. Papannareddy, W. E. Ferguson, and J. K. Butler, IEEE J. Quantum Electron (Submitted for publication).
16. A. Yariv, Quantum Electronics, 2nd Edition, John Wiley &Sons, Inc., New York, 1975.

## FIGURES

Fig. 1 The CSP-DH geometry used for the laser device.

Fig. 2 Optical gain characteristics of the fundamental mode as a function of the intracavity power. The drive current is for a device of length L = 100 μm. The dots are computed from a self-consistent model[5] and the solid curves are obtained from Eq. (6).

Fig. 3 The intracavity power computed from Eq. (9) for a laser of length L = 250 μm. The back facet has $R_2 = 1$ while the front facet reflectivity is treated as a parameter. The total emission power from the front facet is 50 mW.

Fig. 4 Emission power from the front facet versus drive current This data was obtained from repeated solutions of Eq. (9).

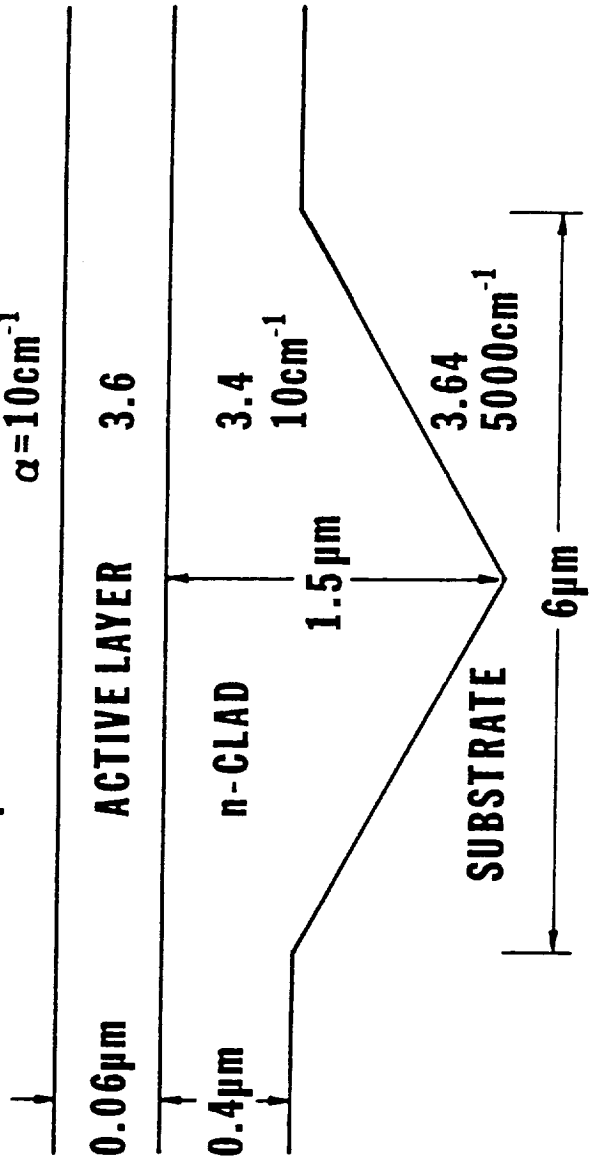
p-CLAD
n=3.4
α=10cm⁻¹
ACTIVE LAYER
3.6
n-CLAD
3.4
10cm⁻¹
SUBSTRATE
3.64
5000cm⁻¹
0.06μm
0.4μm
1.5μm
6μm

Figure 1

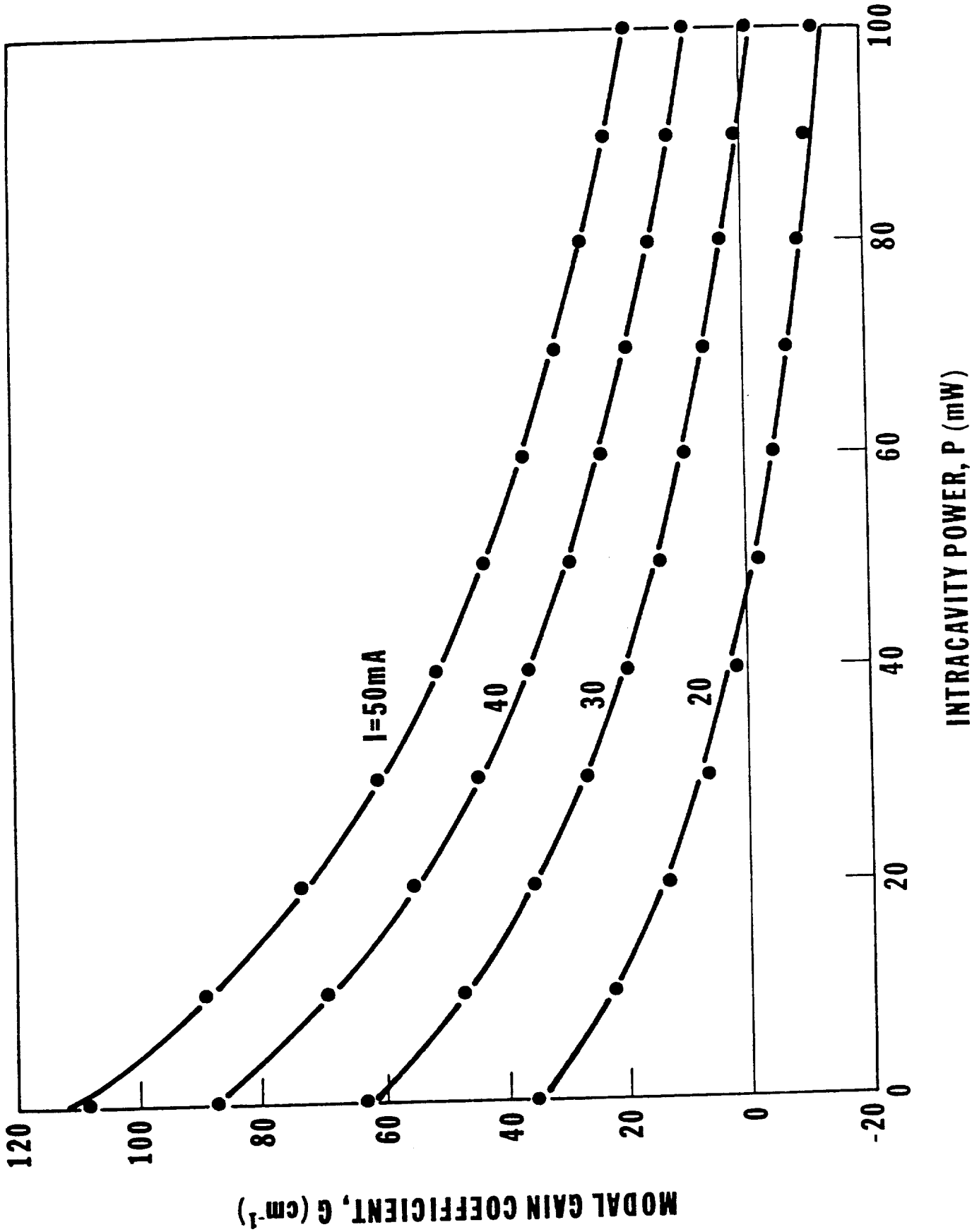
MODAL GAIN COEFFICIENT, G (cm⁻¹)
120
100
80
60
40
20
0
-20
I=50mA
40
30
20
0
20
40
60
80
100
INTRACAVITY POWER, P (mW)

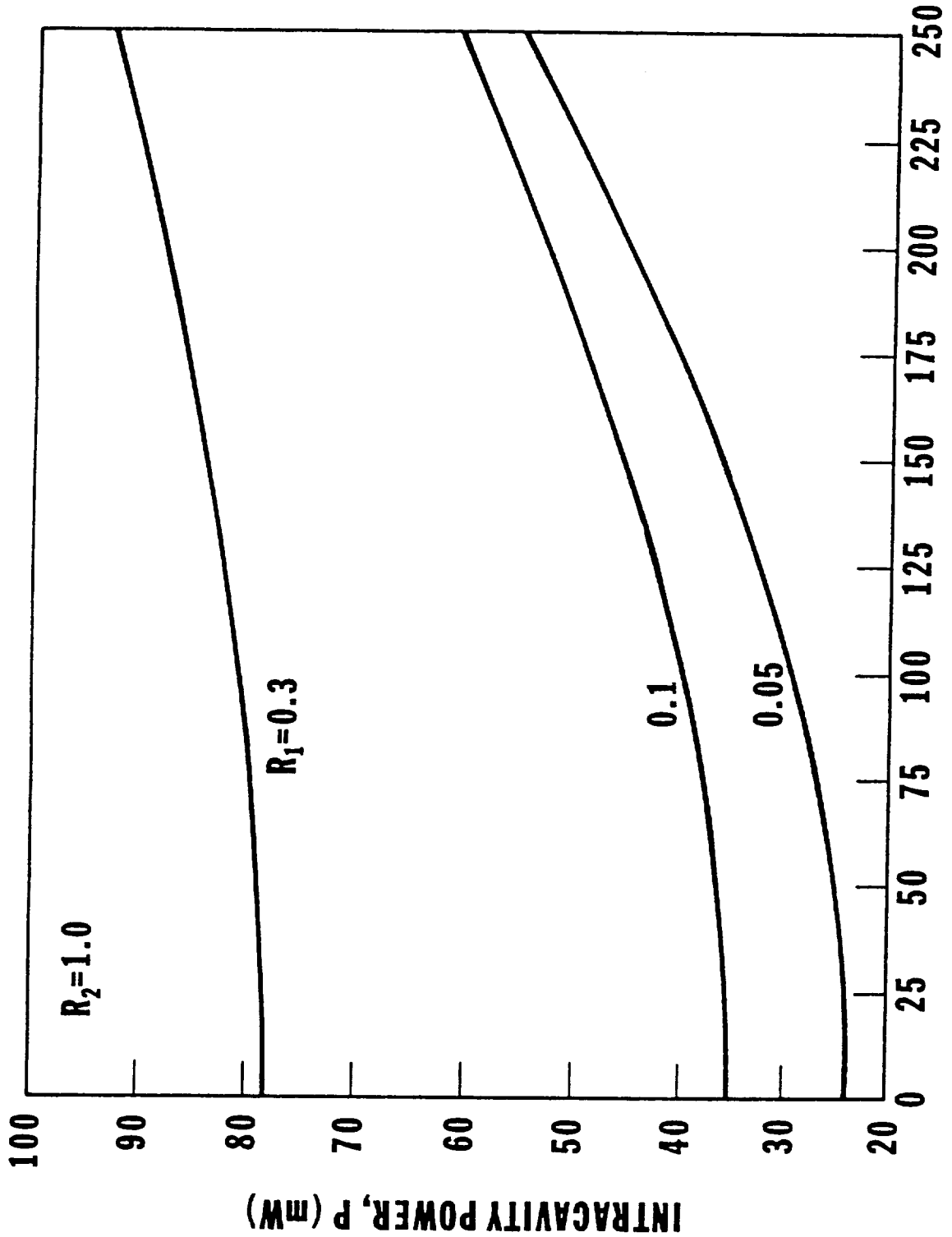
INTRACAVITY POWER, P (mW)
100
90
80
70
60
50
40
30
20
0
25
50
75
100
125
150
175
200
225
250
AXIAL POSITION, Z (μm)
R2=1.0
R1=0.3
0.1
0.05

Figure 3

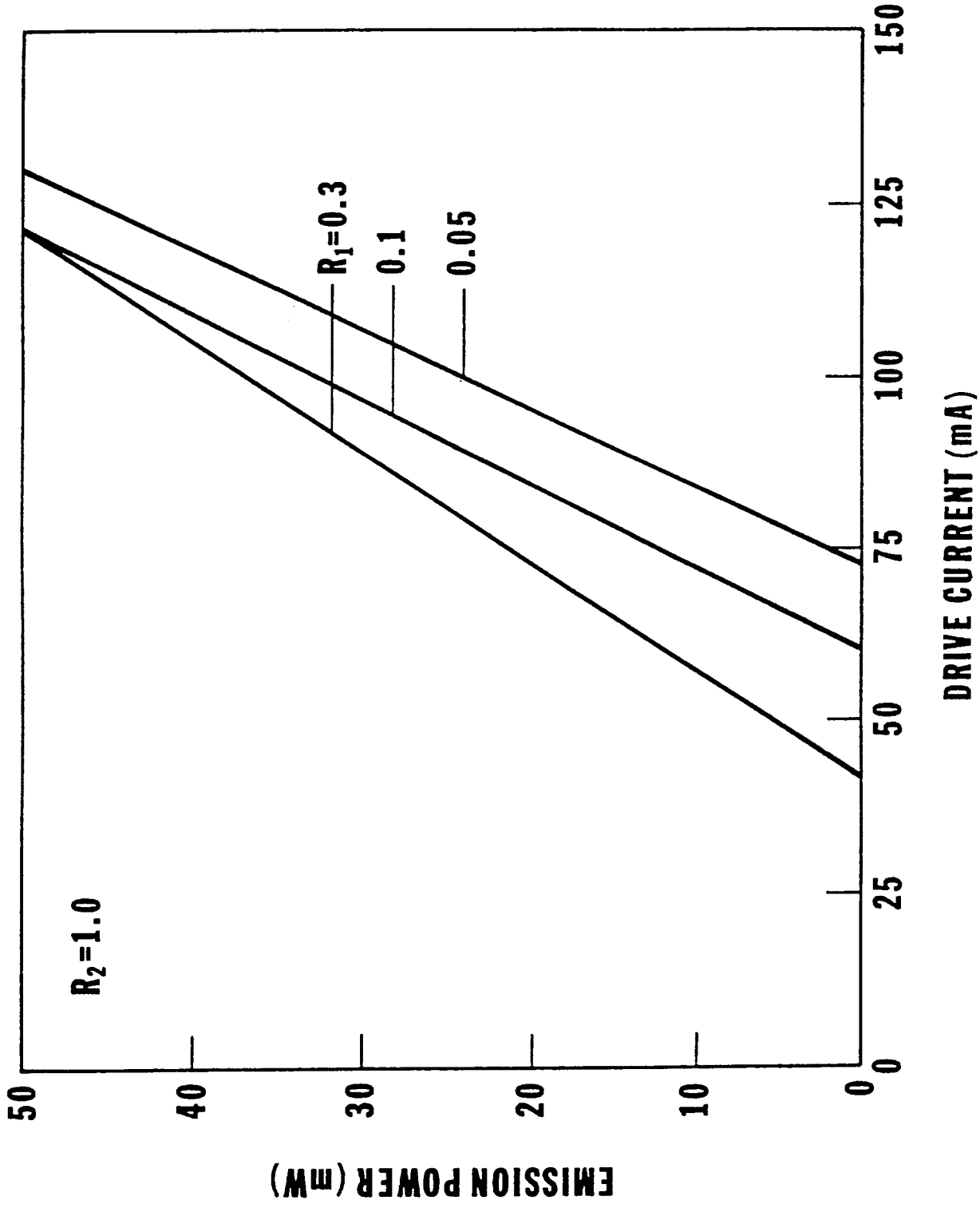
EMISSION POWER (mW)
DRIVE CURRENT (mA)
$R_1$=0.3
0.1
0.05
$R_2$=1.0
0
10
20
30
40
50
25
50
75
100
125
150

Figure 4

# Appendix B

# Observations and Consequences of Non-Uniform Aluminum Concentrations in the Channel Regions of AlGaAs Channeled-Substrate-Planar Lasers*

Gary A. Evans, Bernard Goldstein** and Jerome K. Butler***
David Sarnoff Research Center
CN 5300
Princeton, NJ 08543-5300

## ABSTRACT

Compositional changes in the n-clad layer within the channel region of channel substrate planar (CSP) type semiconductor lasers have been observed. As a consequence, a large optical cavity (LOC) or an enhanced substrate loss (ESL) version of the CSP geometry may result, both of which may have significantly different characteristics from those of a conventional CSP laser. The CSP-LOC generally has a larger near field spot size, while the ESL-CSP is characterized by an off-axis, asymmetric far-field pattern.

---

*This work was supported in part by the National Aeronautics and Space Administration under Contract Number NAS1-17441.

**Presently with Solarex Corp., Newtown, PA 18940

***Southern Methodist Univ., Dallas, TX 75275

# Observations and Consequences of Non-Uniform Aluminum Concentrations in the Channel Regions of AlGaAs Channeled-Substrate-Planar Lasers*

Gary A. Evans, Bernard Goldstein** and Jerome K. Butler***
David Sarnoff Research Center
CN 5300
Princeton, NJ 08543-5300

## I. INTRODUCTION

Generally, in the design and analysis of liquid-phase-epitaxy grown channeled-substrate-planar (CSP) lasers (1,2), the Al concentration within each epilayer is assumed to be uniform. Experimentally this is often not the case: within the channel of the n-clad layer (Fig. 1a), significant non-uniformities in the direction perpendicular to the junction can exist in the Al/Ga ratio. This paper presents and discusses this evidence, and examines the consequences of these non-uniformities. We find that the AlAs non-uniformities in the channel can change a conventional CSP double heterostructure (DH) into either a CSP-LOC (large optical cavity) (3,4) or a CSP structure with increased losses in the substrate which we have called an Enhanced Substrate Loss (ESL) CSP. The resulting CSP-LOC laser generally has a wider perpendicular full-width-half-power (FWHP) near-field distribution, and similar or larger perpendicular far-field beam divergence compared to a conventional CSP laser. The ESL-CSP laser has an asymmetric perpendicular far field and can have either a larger or smaller FWHP perpendicular far field compared to a conventional CSP laser.

---

*This work was supported in part by the National Aeronautics and Space Adminstration under contract number NAS1-17441.

**Presently with Solarex Corp., Newtown, PA 18940

***Southern Methodist Univ., Dallas, TX 75275

Asymmetries in the perpendicular far fields of conventional DH lasers are theoretically unexpected: The large real index steps perpendicular to the junction in AlGaAs DH lasers (Fig. 1a) require that the near-field solution to the electromagnetic wave equation be almost real with only a negligible imaginary component due to active layer gain and material losses. Since the far field pattern is related to the near field distribution by a Fourier transform, the far field pattern should be symmetric about an axis normal to the laser facet because the Fourier transform of a real function is symmetric. However, double-heterostructure lasers with a thin (< 1.0 μm) cladding layer will have asymmetric, off-axis far-fields (5,6,7) due to radiation losses in the cap or substrate.

Experimental measurements of our CSP lasers indicate that in some channels the gradient is from high Al to low Al starting at the bottom of the channel, while in other channels on the same wafer, the gradient is reversed. Both types of aluminum composition grading can occur in the channels of CSP lasers from portions of a wafer that otherwise produce conventional CSP-DH lasers. Aluminum composition grading has been observed in channels etched in both the V-groove (Fig. 2a) and the dovetail (Fig. 2b) directions.

## II. EXPERIMENTAL MEASUREMENTS AND ANALYSIS

### A. Higher AlAs Concentration at the Bottom of the Channel

The principal experimental technique used for the surface compositional analysis on the cleaved facets of the lasers was Auger Electron Spectroscopy using a primary electron beam with a resolution of about 1000 Å. Figure 1b shows Auger spectra that indicate the surface composition on a cleaved facet of a CSP type laser at the points x = 0.3 μm and x = 1.2 μm shown in Fig. 1a. The magnitudes of the Ga, As and Al lines shown on the spectra reflect the concentration of these constituents at the two points and indicate that the Al concentration at the bottom of the channel is about twice that just below the active region. Note that the change in the magnitude of the Al line is tracked by a corresponding change in the magnitude of the Ga line while the As line has remained essentially

unchanged. Examining a random sampling of CSP lasers has established that the magnitude of the concentration variations indicated in Fig. 1b ranges from zero to about a factor of two.

The Al concentration variation we are reporting can also be seen qualitatively in the scanning electron micrograph of the cleaved facet shown for a dovetail channel in Fig. 2b. Here, part of the backscattered electron signal is due to the average atomic number Z of the surface under examination. Thus, brighter regions in the micrograph are regions of material with a higher atomic number compared to neighboring darker regions, so that regions of higher Al concentration will be darker than those of lower Al concentration. The difference in atomic number between Al and Ga is 2.5. In the SEM micrograph of Fig. 2b, the laser structure is clearly defined. The 0.9 μm cap layer and 0.1 μm active layer are delineated by the bright horizontal images (0 and 7% AlAs content, respectively), while the two cladding layers (both nominally 33% AlAs) show up as darker regions on either side of the active layer. Within the channel shown in Fig. 2b, the dark region indicates a significantly higher AlAs content at the channel bottom, while the lighter region indicates a significantly lower AlAs content adjacent to the active layer--in agreement with the Auger analysis data shown in Fig. 1b.

A non-uniform Al/Ga ratio within the channel will effect the dielectric profile perpendicular to the junction. Figure 3 contains a series of possible index profiles together with their electric field distributions for a) a uniform Al/Ga ratio in the channel (CSP); b) a higher Al/Ga ratio at the channel bottom (CSP-LOC); and c) a lower Al/Ga ratio at the channel bottom (ESL-CSP). Graded index profiles are also possible. However, their characteristics are qualitatively similar to the abrupt step profiles discussed in this paper. The aluminum concentrations and corresponding index values for the three structures shown in Fig. 3 are tabulated in Tables 1, 2, and 3. The loss of each epi-layer is taken to be 10 $cm^{-1}$. The value used for the substrate loss $\alpha_s$ (at $\lambda = 0.83$ μm), for all calculations

was 5000 $cm^{-1}$ (8). However, there is insignificant difference in all calculated results as $\alpha_s$ varies from 1000 to 10000 $cm^{-1}$, in agreement with earlier reports (2,9).

The electric field distribution perpendicular to the p-n junction in the channel, $E_y(x)$, is obtained by solving the one dimensional wave equation (assuming region A of Fig. 1a is infinitely wide):

$$\partial^2 E_y/\partial x^2 + (\varepsilon_r k_o^2 - \beta^2)E_y = 0 \qquad [1]$$

with the usual boundary conditions (1,2) using an algorithm for calculating complex modes in plane-layered, complex dielectric structures (10). Here, $\varepsilon_r(x)$ is the complex relative electric permittivity, $k_o = 2\pi/\lambda_o$, and $\lambda_o$ is the free space wavelength. An $\exp[-i(\beta z-\omega t)]$ longitudinal and time variation of the electric field is assumed. The real part of the complex index of refraction $n^*(x)$, shown in Fig. 3, is the real part of the square root of the complex relative electric permittivity. The effective index of region A (Fig.1a) is

$$n^A_{eff} = Re(\beta/k_o) \qquad [2]$$

and the effective absorption coefficient of region A is

$$\alpha = -2k_o\, Im(\beta/k_o) \qquad [3]$$

The theoretical calculations of the electric field and near field intensity distributions are both normalized according to

$$1 = \int_{-\infty}^{\infty} E_y(x)\, E^*_y(x)\, dx \qquad [4]$$

The far field intensity distribution $I(\theta)$ is calculated from the complex electric field distribution according to

$$I(\theta) = \left| g(\theta) \int_{-\infty}^{\infty} E_y(x) \exp(j \sin\theta \, k_o x) dx \right|^2 / \left| g(0) \int_{-\infty}^{\infty} E_y(x) \, dx \right|^2 \qquad [5]$$

where $g(\theta)$ is the obliquity factor (11).

The confinement factor $\Gamma$ is defined for any layer as

$$\Gamma_{layer} = \int_{layer} E_y(x) \, E^*_y(x) dx / \int_{-\infty}^{\infty} E_y(x) \, E^*_y(x) \, dx \qquad [6]$$

The data in Figs. 1 and 2 indicate cases in which the aluminum concentration is highest in the bottom of the channels. In these cases, the resulting perpendicular index profile is no longer that of a simple double heterostructure (Fig. 3a), but that of a large optical cavity (Fig. 3b). Such a dielectric profile was originally introduced intentionally (3) to lower the optical power density by producing a wider perpendicular near-field distribution than that of a conventional DH configuration . In Fig. 4a the FWHP of the near field intensity is plotted as a function of AlAs composition (or index at $\lambda = 0.83$ μm) of the LOC layer assuming the AlAs mole fraction of the p- and n-clad layer is 0.33 and that of the active layer is 0.07. The CSP-LOC FWHP near field intensity of the fundamental mode reaches a maximum of about 0.4 μm (for a 0.4 μm thick LOC layer) and 0.72 μm (for a 0.9 μm thick LOC layer) at AlAs compositions of the LOC layer of about 18%. These curves are not meant to be design curves for LOC structures. They are meant to indicate general patterns of behavior and do not consider, for example, higher order modes which are possible in very thick (> 0.5 μm) LOC layers (3,4).

Parenthetically, if the aluminum content is greater at the bottom of the channel than in the p-clad layer, it is possible for a LOC layer of a CSP-LOC to actually decrease the FWHP of the near field intensity. This is shown in Fig. 5a, which is a plot similar to that in Fig. 4a except that the n-clad region has an AlAs mole fraction of 45%: the FWHP of the near field intensity initially decreases as the Al is increased in the LOC layer. In both Figs. 4 and 5, as the AlAs composition of the LOC layer is decreased below 33%, the CSP-LOC FWHP near field spot size is always greater than that for a conventional CSP laser.

Figure 6 contains experimentally observed photographs of the near-fields of three CSP lasers operating at 20 mW cw, all from the same wafer, showing considerable variation in the perpendicular spot size. The near fields in Fig. 6b and c show some asymmetry in the direction of the channel, which is not characteristic of a conventional CSP DH with equal AlAs compositions in the p- and n- clad layers. These experimental results are in qualitative agreement with the calculated near-fields shown in Fig. 7a for a conventional CSP laser, a CSP-LOC laser (LOC composition =22% AlAs, n-clad composition = 33% AlAs), and an ESL-CSP laser (ESL-LOC layer composition =33% AlAs, ESL n-clad layer composition = 26%). The far fields corresponding to the near field intensity and phase distributions of Fig. 7a and b are shown in Fig. 7c.

An additional consequence of aluminum composition changes in the channel region is a variation in the FWHP perpendicular beam divergence. The FWHP of the far-field radiation lobe of the laser corresponding to Fig. 6(a) is 35°, while that of the laser corresponding to Fig. 6(c) is 28°. While this range in FWHP perpendicular beam divergence could be explained by a variation in active layer thickness from 650 Å to 1000 Å for a conventional CSP laser, an alternative explanation is a nonuniform Al compositon in the channel region as shown in Figs. 5b and 8. In Fig. 8 the FWHP perpendicular beam divergences are plotted (for the same parameters used in Fig. 4 to plot the FWHP of the near field) as the Al composition of the LOC layer (CSP-LOC structures) or n-clad layer

(ESL-CSP structures) varies from 33% to 7%. Figure 8 shows that nonuniformities in the Al composition in the channel region can cause a range in FWHP perpendicular beam divergences from about 20° to more than 50° for a fixed active layer thickness of 800 Å. These calculations indicate that observed variations in FWHP perpendicular beam divergences can result not only from variations in active layer thicknesses, but also from variations in Al compositions in the LOC or n-clad layers of any semiconductor laser.

Finally, the larger perpendicular near-field spot sizes shown in Fig. 6 (and calculated in Figs. 4 and 5) result in a decreased optical power density which might be expected to result in longer operating life at moderate to high power. This expectation was found experimentally for the three lasers (all from the same wafer) whose near-field photos are shown in Fig. 6 . Operating at 20 mW cw and at 30° C, the first unit (6a) lasted 50 hours, the second unit (6b) about one thousand hours, while the third (6c) is still operating after 17,000 hours.

### B. Lower AlAs Concentration at the Bottom of the Channel

Shown in Fig. 9 is a schematic drawing of the channel region of a CSP laser together with Al concentrations as given by Auger Electron Spectroscopy data. Here, the Al content is lower at the bottom of the channel. The resulting index profile (Fig. 3c) can be thought of as "pulling" some of the mode power into the substrate, increasing the mode loss. This mechanism, which we call Enhanced Substrate Loss (ESL), can also be explained by realizing that all of the modes supported by the index profiles shown in Fig. 3 are complex modes (12) (i.e., the longitudinal and transverse wave vectors have a real and imaginary component), because the field solutions to the electromagnetic wave equation [1] are "sinusoidal" in the substrate (13). Usually, the n-clad region separating the active region (and LOC layer, if present) from the substrate is thick enough (> 1 μm) that field penetration of the laser mode into the substrate is negligible (see Fig. 3a, b). However, if the mole fraction of AlAs is lower at the bottom of the channel than at the top of the

channel, the higher index portion (layer 4 of Fig. 3c) in the channel acts like an anti-reflection coating (14) between the high aluminum, low index portion (layer 3) and the no aluminum, very high index substrate (layer 5), thereby coupling or redistributing a larger fraction of the mode power into the substrate. In Fig.10, the ratio of energy confined in the laser substrate to the total mode energy ($\Gamma_s$, the substrate confinement factor) is plotted as a function of the mole fraction of AlAs (or index of refraction at $\lambda = 0.83$ μm) of the bottom half of the channel region (layer 4) for the index profile shown in Fig. 3c. The peaks in this plot correspond to index values that optimize the coupling of light into the substrate for the 0.9 μm thickness of the index "matching" layer (layer 4). In the vicinity of these peaks, the mode has significant energy directed both along the waveguide axis and into the substrate, and the corresponding far field pattern is no longer peaked perpendicular to the facet, but is tilted towards the substrate on the order of a few degrees as shown by the calculated far fields--see Fig. 7c and insets in Fig. 10. This far-field tilt is consistent with the asymmetric near-field phase of the ESL-CSP laser (Fig. 7b) which, unlike that of the CSP-LOC or CSP laser, is not flat over the region ($0.4 < x < 2.0$) where the optical field has a significant amplitude. The asymmetric far field pattern for the ESL-CSP laser in Fig. 7c is caused by the asymmetry of the near field phase variation in Fig. 7b.

For both the ESL-CSP and CSP-LOC lasers, the thicknesses and refractive indices of the LOC and n-clad layers chosen for the theoretical models are not unique. The cases illustrated in this paper correspond to fixed layer thicknesses with a varying index of refraction in one layer (Fig. 4, 5, and 10). However, a curve similar to Fig. 10 is obtained by assuming an index $n_4$ ($n_3 < n_4 < n_5$) for the n-clad layer and varying the thickness of the n-clad layer.

Experimentally observed far-field intensity patterns of several ESL-CSP lasers (with V-groove channels) from the same wafer are shown in Fig. 11. The experimental asymmetric profiles agree qualitatively with the theoretical profiles shown in Fig. 10. In general, the asymmetric far field profile for a given ESL-CSP laser does not change as a

function of power even at power levels above 100 mW. The shift of the peak of the experimental far fields from the normal to the facet ranges from less than $2^{o}$ to about $9^{o}$, in agreement with the calculated shifts (up to $8^{o}$) shown in Figs. 7c and 10. The experimental range in FWHP of the far field patterns range from $18^{o}$ to $33^{o}$ compared to a theoretical range of $20^{o}$ to $42^{o}$ for the parameters assumed in Fig.8. Distinct sidelobes appear in the experimental far field shown in Fig. 11a and in some of the calculated far fields shown in Fig. 10 and 7c. These sidelobes can be explained as the interference pattern in the far field between two peaks of the near field intensity. For example, the near field distribution of the ESL-CSP laser shown in Fig. 7a can be approximated by two point sources separated by 1.3 μm. From Fig. 7b, the smaller peak is shifted in phase by an average of about 90° relative to the main peak. The interference pattern from this simple two point approximation has a central peak at 9.2° and sidelobes at 28.6° and -52.9°, in general agreement with the ESL-CSP far field pattern shown in Fig. 7c.

Asymmetries and radiation pattern shifts in the perpendicular far field have been observed in many types of AlGaAs semiconductor lasers and we suggest that non-uniform Al compositions are often the explanation.

## III. DISCUSSION

The cause of a non-uniform Al/Ga ratio occurring within the channel of a CSP laser during the LPE growth of the first cladding layer is not fully understood. However, we do know 1) that the layer growth must be faster at the bottom of the channel than at the top in order to result in flat growth profiles, 2) that there must be a lateral component of growth within the channel as well as a perpendicular component, 3) that the wall and bottom curvatures of the channel present crystallographic planes to the growth nucleation that are different from those above the channel where the growth is planar (15), and 4) that there can be varying degrees of meltback at the channel walls and shoulders as shown in Fig. 2. Any of these conditions can readily affect the composition of the ternary compound that

initially nucleates and freezes out from the AlGaAs melt, and can alter this composition as the growth proceeds and overall growth conditions change. Furthermore, if the Al/Ga ratio changes during the initial growth, then changes in the local melt composition may occur which might further change the Al/Ga ratio later along in the growth. From the AlAs-GaAs phase diagram (16), very small changes in Al in the melt produce very significant changes in the Al content in the grown material. The basis for a non-uniform Al/Ga ratio within the channel of a CSP laser discussed above is also consistent with the variability of this effect from channel to channel since it would be the local conditions around each channel (shape, initial freeze-out rate, local melt composition) that would determine the magnitude of the effect. The lasers discussed in this paper were grown at 800°C with about 4°C of supersaturation and a cooling rate of 0.75°C/minute. The p- and n- dopants were Ge and Sn.

While the CSP-LOC structure produced by higher Al concentrations at the bottom of the channels has generally familiar and well understood consequences, the ESL-CSP structure produced by lower Al concentrations at the bottom of the channel has some peculiar properties. First, the internal losses of the perpendicular component of the ESL mode can be almost an order of magnitude higher than that of the conventional CSP or CSP-LOC, as shown in Fig. 12, which could noticeably increase the threshold current and decrease both efficiency and lifetime. (However, we have not seen a clear correlation between increases in threshold current and decreases in differential quantum efficiency with asymmetries in the far field pattern of our lasers.) Second, the near field and far field FWHP plots summarized in Figs. 4,5,7 and 8 are not those intuitively expected from plane wave, uniform intensity diffraction theory which equates the far field beam divergence $\theta_B$ to $\lambda/D$, where D is the near field aperture: The ESL-CSP structure can have a narrower FWHP perpendicular near field intensity and a narrower FWHP perpendicular beam divergence than a CSP or CSP-LOC structure. Additionally, while the FWHP of the perpendicular near field spot sizes for the CSP-LOC structures are 2 to 3 times larger than

that for a conventional CSP (Fig. 4), the CSP-LOC FWHP beam divergences are larger by typically $10^{o}$ (Fig. 8). Finally, both the CSP-LOC FWHP beam divergences (Fig. 5b and 8) and the FWHP near field intensities (Fig. 4a and 5a) simultaneously increase over some ranges of AlAs variation. These apparent contradictions result because the FWHP, by itself, of the various near field intensities can be a misleading and inappropriate representation of the near field aperture. For example, the ESL-CSP structure has a very narrow FWHP beam divergence of about $24^{o}$ (Fig. 7c) and a narrow FWHP near field spot size of about 0.26 μm. However, because of an irregular distribution of mode power, the effective near field aperture (Fig. 7a) is actually about 1.5 μm. The reason for these apparent contradictions is primarily because the FWHP of the near field intensities contain varying fractions of the mode power. Such apparent contradictions would be largely eliminated (17) by a definition of near field aperture and far field beam divergence corresponding to near and far field widths enclosing the same percentage (for example, 80%) of mode power, instead of the experimentally convenient measurement of FWHP.

The effect of Al variations on lateral mode confinement has not been investigated in detail. However, since only the fundamental lateral mode is observed experimentally, the difference between the magnitude of the complex effective index in the channel (region A of Fig. 1a) and outside the channel (region B of Fig.1a), $\Delta n_{eff}$ ($= |n^{*}A_{eff}| - |n^{*}B_{eff}|$), must be much less than 0.1 for channel widths ranging from 4 to 7 μm. Figure 13 shows that while the effective index in the channel region ($n^{*}A_{eff}$) for the ESL-CSP structure changes negligibly with changes in Al concentration ($\sim 4 \times 10^{-4}$), the effective index in the channel region of the CSP-LOC structure changes significantly ($\sim 2 - 6 \times 10^{-2}$). Thus, the observed absence of higher order lateral modes, for the CSP-LOC structure, suggests that Al composition changes may occur in the n-clad layer outside the channel that follow, at least partially, those inside the channel, and result in a corresponding increase in $n^{*}B_{eff}$.

## IV. CONCLUSIONS

The net result of the effect described here is that due to compositional changes in the n-clad layer within the channel, a CSP-LOC or ESL-CSP can be inadvertently grown instead of a conventional CSP laser, all three of which have significantly different characteristics. We also give a theoretical explanation for asymmetric perpendicular far-field patterns which have been experimentally observed in CSP and other AlGaAs laser structures.

## ACKNOWLEDGEMENTS

We are indebted to D. Szostak for the Auger surface analysis measurements, N. Dinkel for the growth of the lasers, V. Masin for computer program development and technical discussions, E. DePiano, D. Tarangioli, and M. Harvey for laser processing, and to D. Carlin, N. Carlson, J. Connolly, M. Ettenberg, J. Hammer, F. Hawrylo, M. Lurie, and S. Palfrey for technical discussions.

# REFERENCES


1) K. Aiki, M. Nakamura, Takao Kuroda, J. Umeda, R. Ito, Naoki Chinone, and M. Maeda, "Transverse Mode Stabilized $Al_xGa_{1-x}As$ Injection Lasers with Channeled-Substrate-Planar Structure," IEEE Journal of Quantum Electronics, Vol. QE-14, No. 2, pp.89-94, Feb. 1978.

2) T. Kuroda, M. Nakamura, K. Aiki, and J. Umeda, "Channeled-substrate-planar structure $Al_xGa_{1-x}As$ lasers: an analytical waveguide study," Applied Optics, Vol. 17, No. 20, pp. 3264-3267, 15 October 1978.

3) H. Kressel and J. K. Butler, Semiconductor Lasers and Heterojunction LEDs, Chapter 7, Section 5, Academic Press, New York, pp. 230-234, 1977.

4) Toshiro Hayakawa, Takahiro Suyama, Hiroshi Hayashi, Saburo Yamamoto, Seiki Yano, and Toshiki Hijikata, "Mode Characteristics of Large-Optical-Cavity V-Channeled Substrate Inner Stripe Injection Lasers," IEEE Journal of Quantum Electronics, Vol. QE-19, No. 10, pp. 1530-1536, October 1983.

5) J. K. Butler, H. Kressel, and I. Ladany, "Internal Optical Losses in Very Thin CW Heterojunction Laser Diodes," IEEE Journal of Quantum Electronics, Vol. QE-11, No. 7, pp. 402-408.

6) William Streifer, Robert D. Burnham, and Donald R. Scifres, "Substrate Radiation Losses in GaAs Heterostructure Lasers," IEEE Journal of Quantum Electronics, Vol. QE-12, No. 3, pp. 177-182, March 1976.

7) D. R. Scifres, W. Streifer, and R. D. Burnham, "Leaky wave room-temperature double heterostructure GaAs:GaAlAs diode laser," Appl. Phys. Lett., Vol. 29, No. 1, pp.23-25, July 1976.

8) H. C. Casey, Jr., D. D. Sell, and K. W. Wecht, "Concentration dependence of the absorption coefficient for n- and p-type GaAs between 1.3 and 1.6 eV," J. Appl. Phys., vol. 24, pp.63-65, Jan. 1974.

9) D. R. Scifres, R. D. Burnham, and W. Streiffer, "Output coupling and distributed feedback utilizing substrate corregations in double-heterostructure GaAs lasers," Appl. Phys. Lett., Vol. 27, No. 5, pp.295-297, 1975.

10) R. B. Smith and G. L. Mitchel, "Calculation of Complex Propagating Modes in Arbitrary, Plane-Layered, Complex Dielectric Structures. I. Analytic Formulation. II. Fortran Program MODEIG," EE Technical Report No. 206, University of Washington, Seattle, Washington.

11) L. Lewin, "Obliquity-factor correction to solid-state radiation patterns," Journal of Applied Physics, Vol. 46, No. 5, pp. 2323-2324, May 1975.

12) Theodor Tamir and Foon Yeon Kou, "Varieties of Leaky Waves and Their Excitation Along Multilayered Structures," IEEE Journal of Quantum Electronics, Vol. QE-22, No. 4, pp. 544-551, April 1986.

13) This feature of the perpendicular waveguide mode for $x > 0.38$ outside the channel (region B in Figure 1a) is the reason CSP lasers have a higher effective index inside the channel region than outside.

14) M. Born and E. Wolf, Principles of Optics, Chapter 1, pp. 61-66, Pergamon Press, New York, 1975.

15) J. W. Cahn and D. W. Hoffman, "A Vector Thermodynamics For Anisotropic Surfaces--II. Curved and Faceted Surfaces", Acta Metallurgica, Vol. 22, pp. 1205-1214, October 1974.

16) H. Kressel and J. K. Butler, Semiconductor Lasers and Heterojunction LEDs, Chapter 11, p. 372, Academic Press, New York, 1977.

17) The far field beam divergence from a fixed aperture D will, however, have slight to moderate variations as either the near field intensity distribution or the near field phase is changed.

# FIGURE CAPTIONS

Figure 1. a) Geometry of a typical CSP type laser; x = 0 is the top of the active layer and x = 1.8 μm is the bottom of the channel. b) Auger analysis of a cleaved facet of a CSP type laser showing a higher aluminum composition near the bottom of the channel (x = 1.4 μm, dashed line) than near the top of the channel (x = 0.4 μm, solid line).

Figure 2. Scanning electron micrographs of a cross section of a CSP type laser with the channel etched in a) the V-groove direction, and b) the dovetail direction. The dashed black lines indicates the channel profiles before growth.

Figure 3. Index profiles (----) and corresponding electric field distributions (—) for a) a conventional CSP laser; b) a CSP-LOC laser; and c) an ESL-CSP laser. The layer compositions, thicknesses, and effective index for each structure are listed in Tables 1-3. The dashed rectangles in a) and b) show the field distributions on expanded scales for x > 1.8 μm.

Figure 4. a) Calculated near field FWHP as a function of the % AlAs (or index of refraction at λ = 0.83 μm) of a 0.4 μm (----) and 0.9 μm (—) thick LOC layer (CSP-LOC geometry) or of the 0.9 μm (....) thick n-clad layer (ESL-CSP geometry). The n-clad layer (layer 4, Figure 3b) for the CSP-LOC layer has an AlAs mole fraction of 0.33, and the LOC layer (layer 3, Figure 3c) for the ESL-CSP has an Al As mole fraction of 0.33. b) The calculated near field FWHP as a function of AlAs or index of refraction for the ESL-CSP structure on an expanded scale. The common point to all three curves (at an

index value = 3.40657) corresponds to the conventional CSP laser described in Table 1.

Figure 5. Calculated a) near field FWHP and b) far field FWHP as a function of the % AlAs (or index of refraction at $\lambda = 0.83$ μm) of a 0.4 μm (----) and a 0.9 μm (—) thick LOC layer of a CSP-LOC with an n-clad AlAs mole fraction of 0.45.

Figure 6. Near field micrographs of CSP type lasers operating at the same power output showing significantly different perpendicular near fields.

Figure 7. Calculated a) near field intensities, b) near field phases, and c) far field intensities perpendicular to the junction for a conventional CSP laser (—), a CSP-LOC laser (....), and an ESL-CSP laser (----) for the parameters listed in Tables 1-3.

Figure 8. Calculated far field FWHP as a function of the % AlAs (or index of refraction at $\lambda = 0.83$ μm) of a 0.4 μm (----) and 0.9 μm (—) thick LOC layer (CSP-LOC geometry) or of the 0.9 μm (....) thick n-clad layer (ESL-CSP geometry). As in Figure 4, the n-clad layer for the CSP-LOC layer has an AlAs mole fraction of 0.33, and the LOC layer (layer 3) for the ESL-CSP has an Al As mole fraction of 0.33. The common point to all three curves (at an index value = 3.40657) corresponds to the conventional CSP laser described in Table 1.

Figure 9. Composition measured by Auger analysis at four positions along a cleaved facet of a CSP type laser showing a lower aluminum composition near the bottom of the channel than near the top of the channel.

Figure 10. The substrate confinement factor $\Gamma_s$ as a function of the % AlAs (or index of refraction at $\lambda = 0.83$ μm) of the n-clad layer at the bottom of the channel of an ESL-CSP laser. The inset far field intensity vs angle patterns show a large variation in asymmetry as a function of % AlAs of the n-clad layer.

Figure 11. Experimentally measured far field intensity patterns for ESL-CSP lasers.

Figure 12. The perpendicular mode loss in region A of Figure 1a as a function of the % AlAs (or index of refraction at $\lambda = 0.83$ μm) of the n-clad layer at the bottom of the channel of an ESL-CSP laser. The right hand ordinate is the imaginary part of the effective index.

Figure 13. The calculated effective index in the channel as a function of the % AlAs (or index of refraction at $\lambda = 0.83$ μm) of a 0.4 μm (....) thick LOC layer (CSP-LOC geometry) or of a 0.9 μm (----) thick n-clad layer (ESL-CSP geometry). The n-clad layer for the CSP-LOC layer has an AlAs mole fraction of 0.33, and the LOC layer (layer 3) for the ESL-CSP has an Al As mole fraction of 0.33. The common point to both curves (at an index value = 3.40657) corresponds to the conventional CSP laser described in Table 1. The effective index of the ESL-CSP laser changes by less than $4 \times 10^{-4}$ over the index range of the n-clad layer shown. Also shown are typical design values for the effective index in the channel $n^{A(CSP)}_{eff}$ and outside the channel $n^{B(CSP)}_{eff}$ for a conventional CSP laser.

TABLE 1. CSP STRUCTURE

| layer | thickness (μm) | %AlAs | index (λ=0.83μm) | $\Gamma_{layer}$ | $Re\{n^*_{eff}\}$ | $Im\{n^*_{eff}\}$ |
|---|---|---|---|---|---|---|
| 1 p-clad | >1.0 | 33 | 3.40657 | .389 | | |
| 2 active | 0.08 | 7 | 3.62805 | .222 | 3.43401 | $6.6 \times 10^{-5}$ |
| 3 n-clad | 1.8 | 33 | 3.40657 | .389 | | |
| 4 substrate | ~75 | 0 | 3.64 | $3.4 \times 10^{-6}$ | | |

TABLE 2. CSP-LOC STRUCTURE

| layer | thickness (μm) | %AlAs | index (λ=0.83μm) | $\Gamma_{layer}$ | $Re\{n^*_{eff}\}$ | $Im\{n^*_{eff}\}$ |
|---|---|---|---|---|---|---|
| 1 p-clad | >1.0 | 33 | 3.40657 | .19043 | | |
| 2 active | 0.08 | 7 | 3.62805 | .19205 | | |
| 3 LOC | 0.4 | 22 | 3.48276 | .59205 | 3.46932 | $6.6 \times 10^{-5}$ |
| 4 n-clad | 1.8 | 40 | 3.364 | .02546 | | |
| 5 substrate | ~75 | 0 | 3.64 | $2.9 \times 10^{-9}$ | | |

TABLE 3. ESL-CSP STRUCTURE

| layer | thickness (μm) | %AlAs | index (λ=0.83μm) | $\Gamma_{layer}$ | $Re\{n^*_{eff}\}$ | $Im\{n^*_{eff}\}$ |
|---|---|---|---|---|---|---|
| 1 p-clad | >1.0 | 33 | 3.40657 | .331 | | |
| 2 active | 0.08 | 7 | 3.62805 | .190 | | |
| 3 LOC | 0.9 | 33 | 3.40657 | .346 | 3.43405 | $5.11 \times 10^{-4}$ |
| 4 n-clad | 1.8 | 26.3 | 3.45245 | .125 | | |
| 5 substrate | ~75 | 0 | 3.64 | .008 | | |

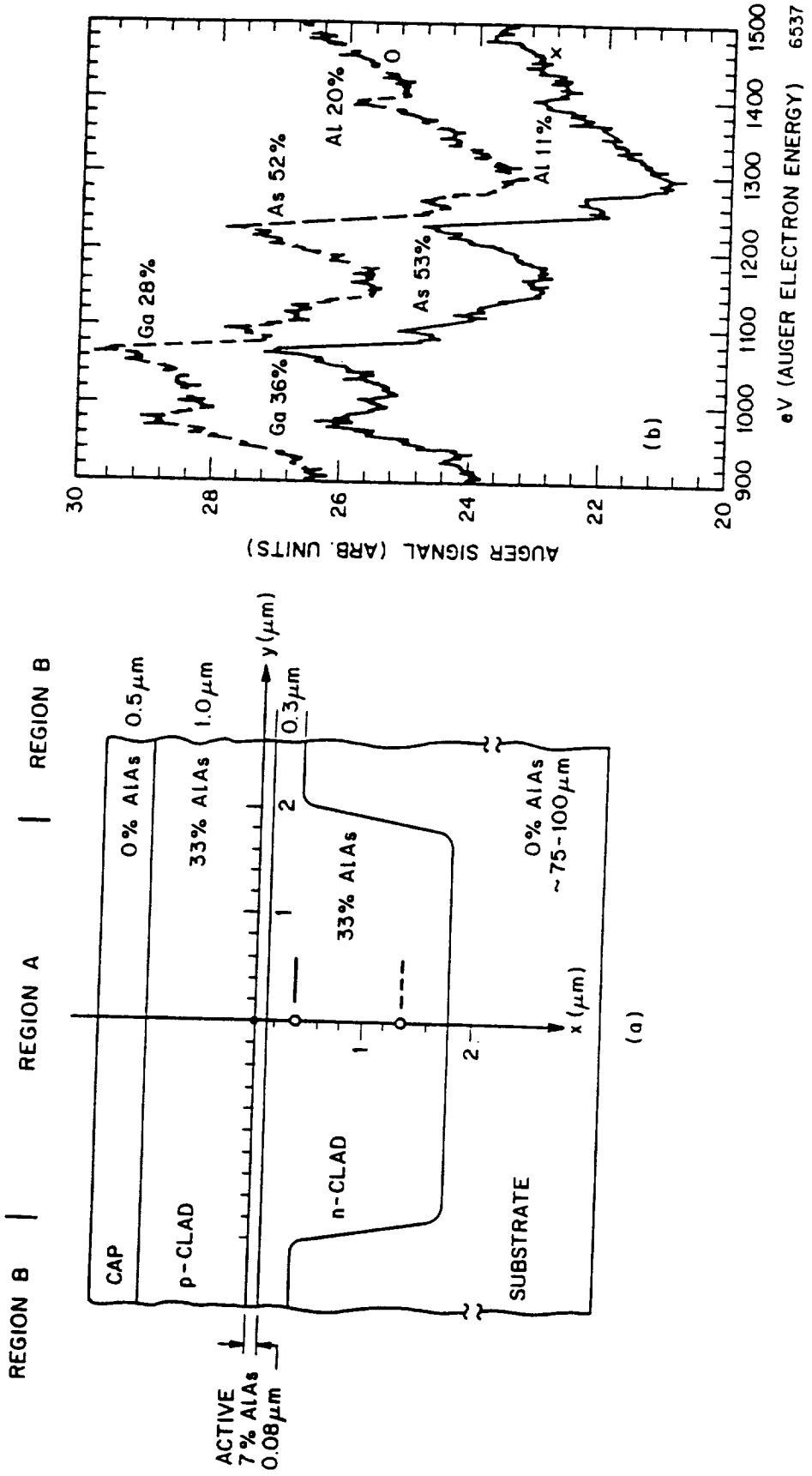
REGION B
REGION A
REGION B
ACTIVE
7% AlAs
0.08μm
CAP
p-CLAD
n-CLAD
SUBSTRATE
0% AlAs
0.5μm
33% AlAs
1.0μm
0.3μm
33% AlAs
0% AlAs
~75-100μm
y (μm)
x (μm)
(a)
AUGER SIGNAL (ARB. UNITS)
Ga 28%
Ga 36%
As 52%
As 53%
Al 20%
Al 11%
O
(b)
eV (AUGER ELECTRON ENERGY)
6537

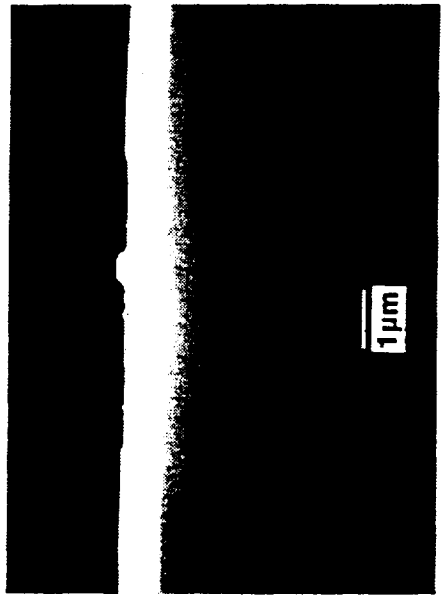

ORIGINAL PAGE IS
OF POOR QUALITY

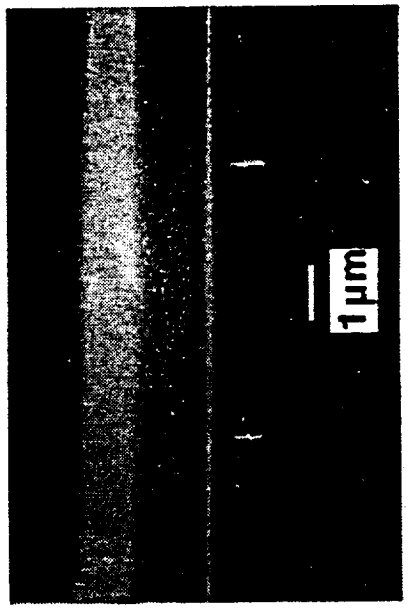

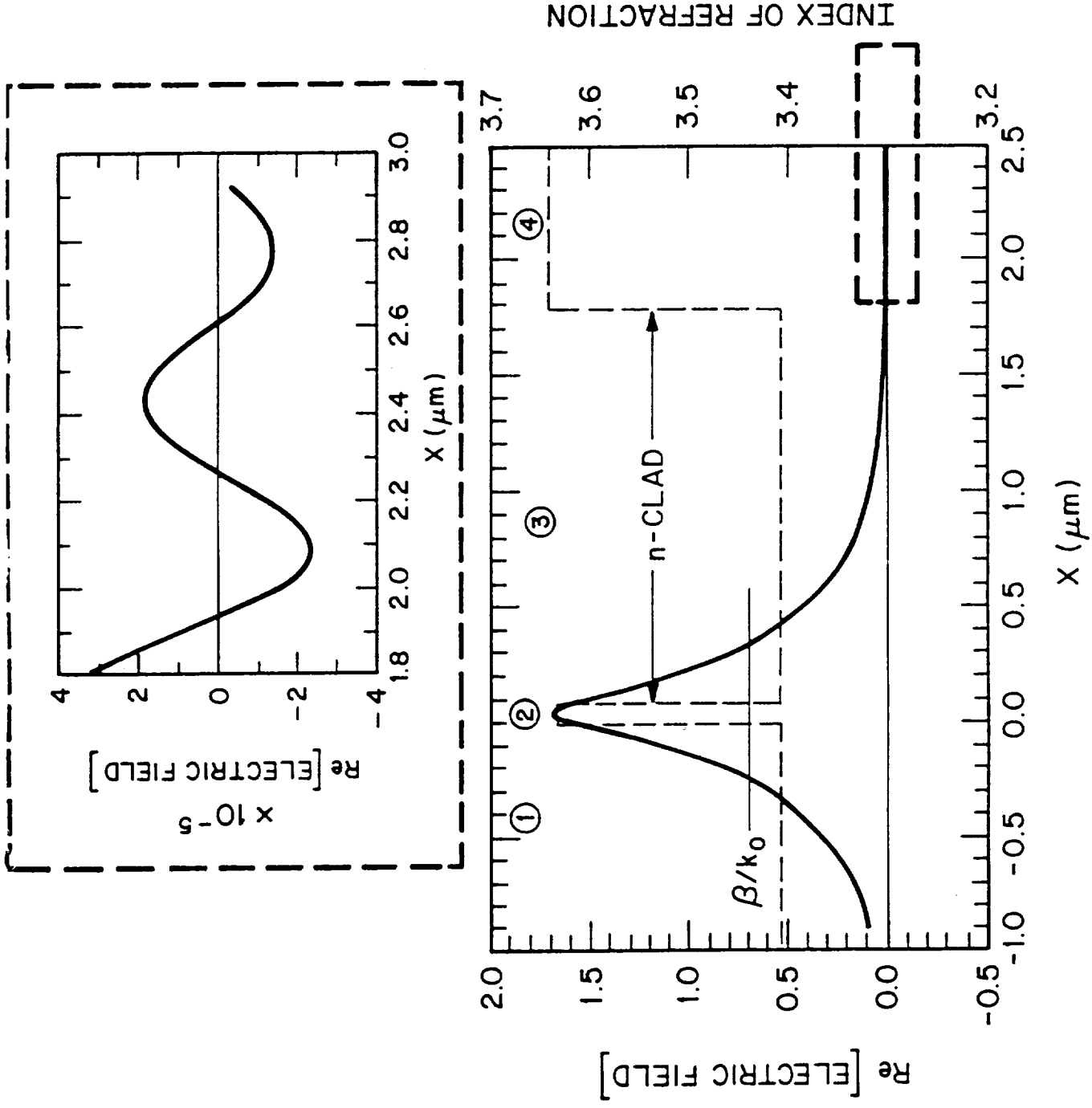
INDEX OF REFRACTION
3.7
3.6
3.5
3.4
3.2
2.5
2.0
1.5
1.0
0.5
0.0
-0.5
-1.0
-0.5
0.0
0.5
1.0
1.5
2.0
X (μm)
Re [ELECTRIC FIELD]
n-CLAD
β/k₀
①
②
③
④
× 10⁻⁵
Re [ELECTRIC FIELD]
4
2
0
-2
-4
1.8
2.0
2.2
2.4
2.6
2.8
3.0
X (μm)

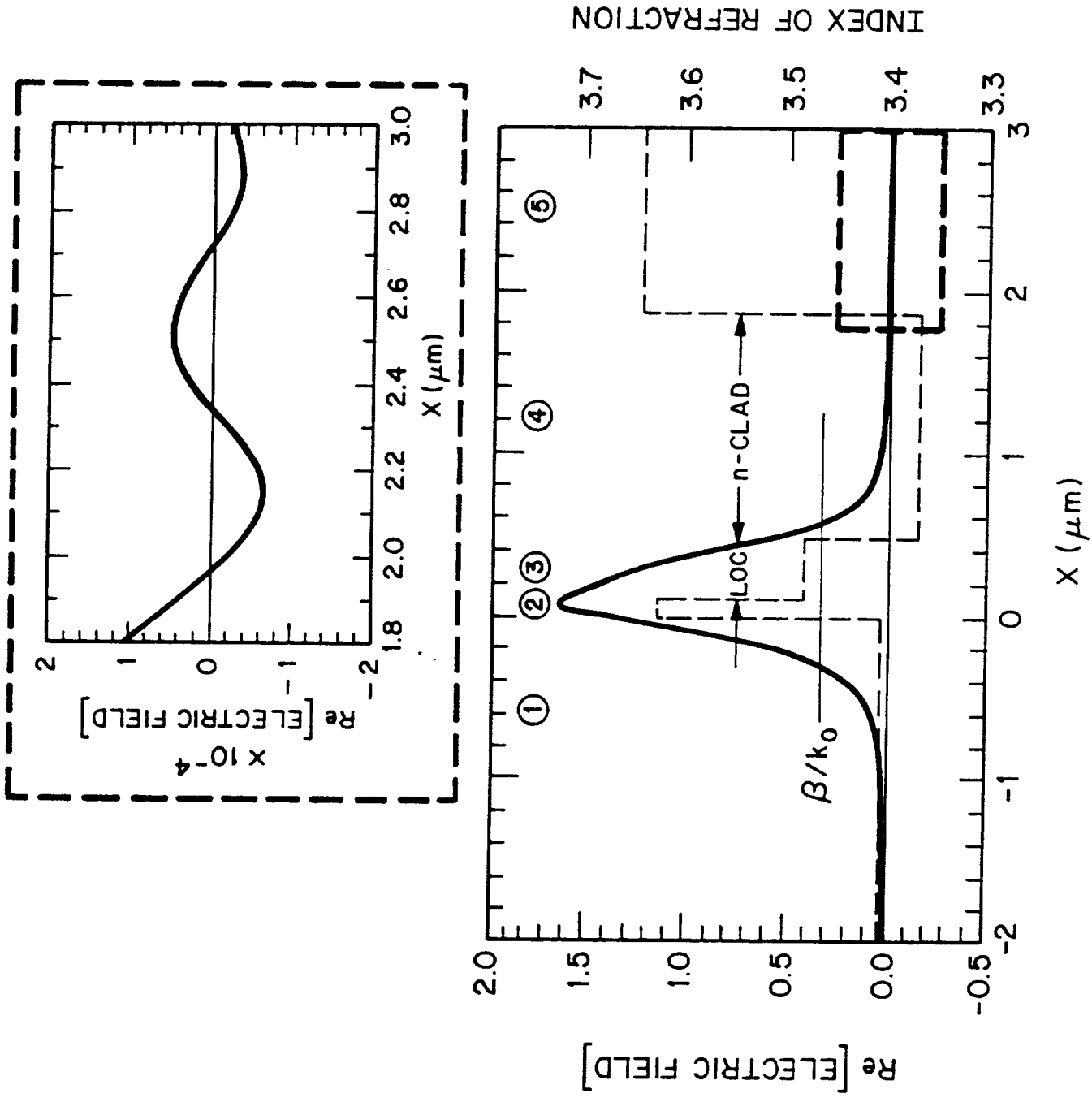
INDEX OF REFRACTION
3.7
3.6
3.5
3.4
3.3
n-CLAD
LOC
β/k₀
①
②③
④
⑤
Re [ELECTRIC FIELD]
2.0
1.5
1.0
0.5
0.0
-0.5
3
2
1
0
-1
-2
X (μm)
Re [ELECTRIC FIELD]
x 10⁻⁴
2
1
0
-1
-2
1.8
2.0
2.2
2.4
2.6
2.8
3.0
X (μm)

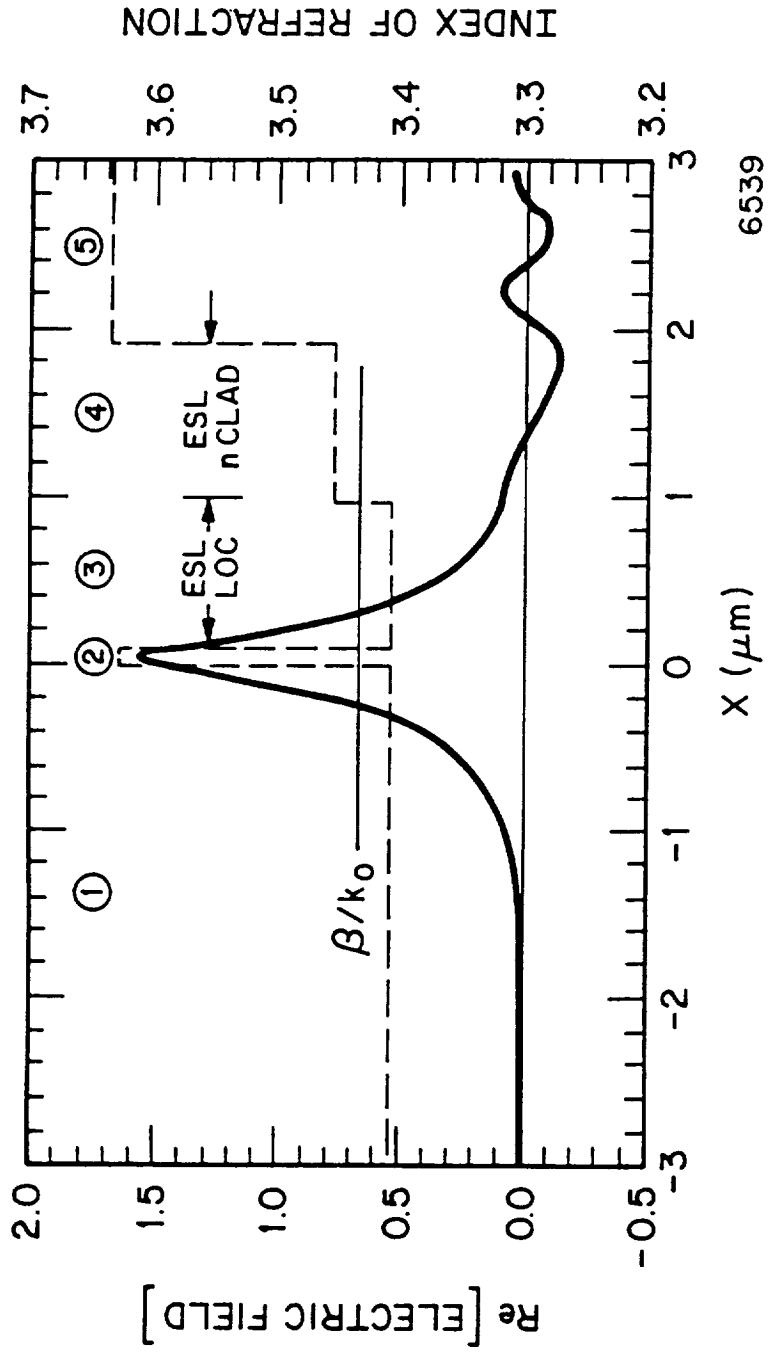
INDEX OF REFRACTION
3.7
3.6
3.5
3.4
3.3
3.2
ESL nCLAD
ESL LOC
β/k₀
①
②
③
④
⑤
2.0
1.5
1.0
0.5
0.0
-0.5
-3
-2
-1
0
1
2
3
X (μm)
Re [ELECTRIC FIELD]
6539

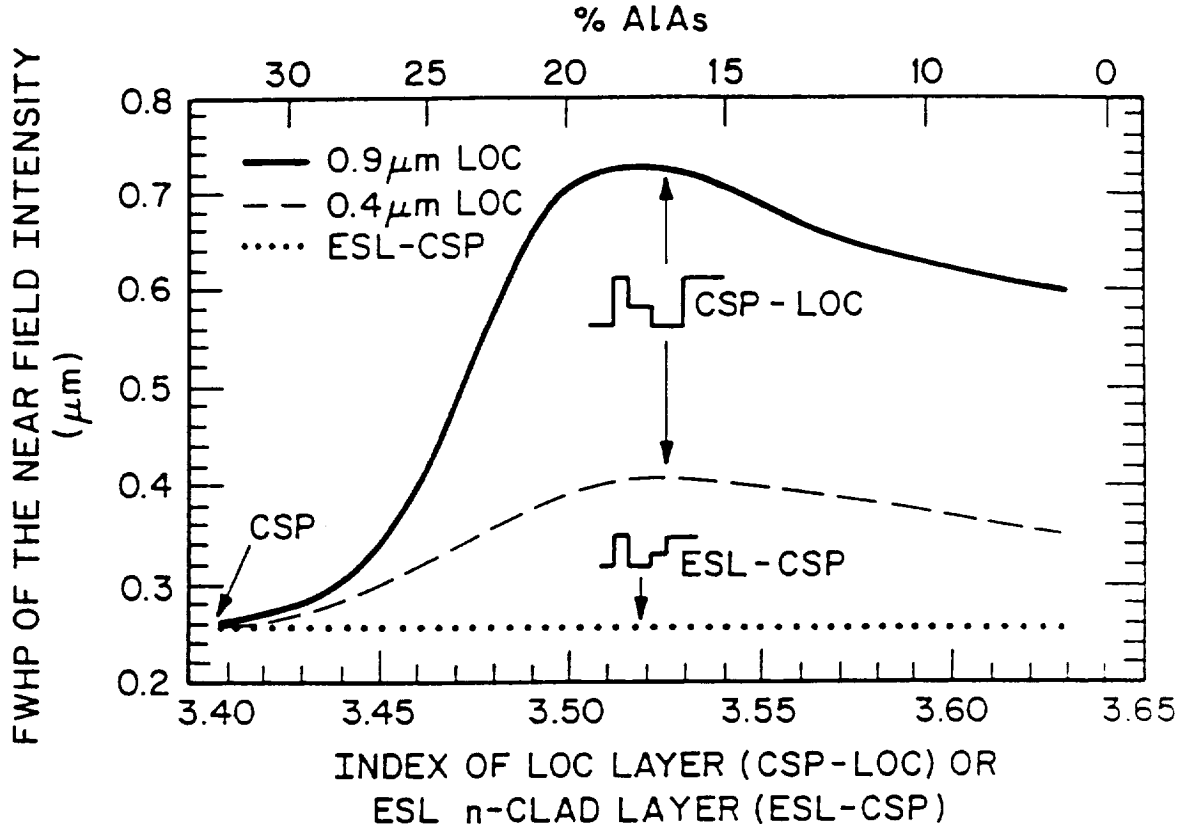
% AlAs
30
25
20
15
10
0
0.8
0.7
0.6
0.5
0.4
0.3
0.2
0.9μm LOC
0.4μm LOC
ESL-CSP
CSP - LOC
CSP
ESL-CSP
FWHP OF THE NEAR FIELD INTENSITY (μm)
3.40
3.45
3.50
3.55
3.60
3.65
INDEX OF LOC LAYER (CSP-LOC) OR
ESL n-CLAD LAYER (ESL-CSP)

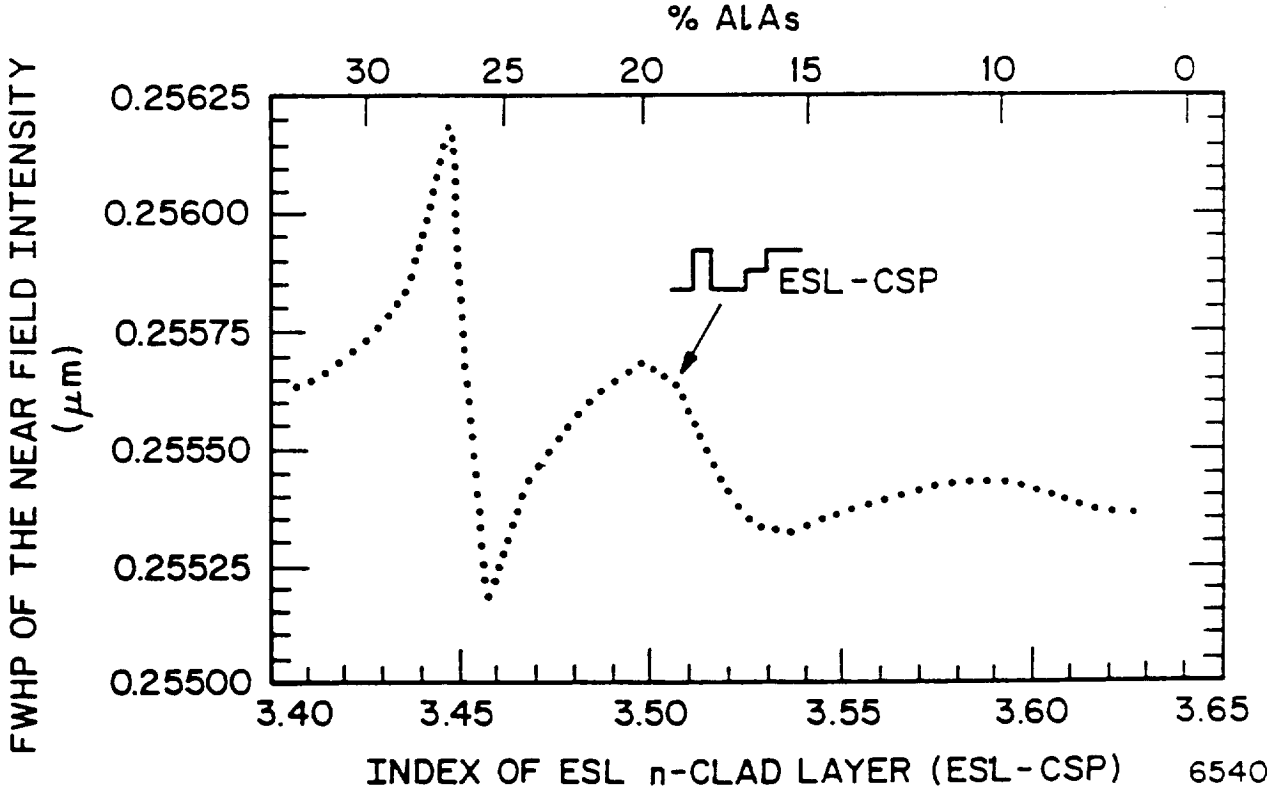
% AlAs
30
25
20
15
10
0
0.25625
0.25600
0.25575
0.25550
0.25525
0.25500
ESL-CSP
FWHP OF THE NEAR FIELD INTENSITY (μm)
3.40
3.45
3.50
3.55
3.60
3.65
INDEX OF ESL n-CLAD LAYER (ESL-CSP)
6540

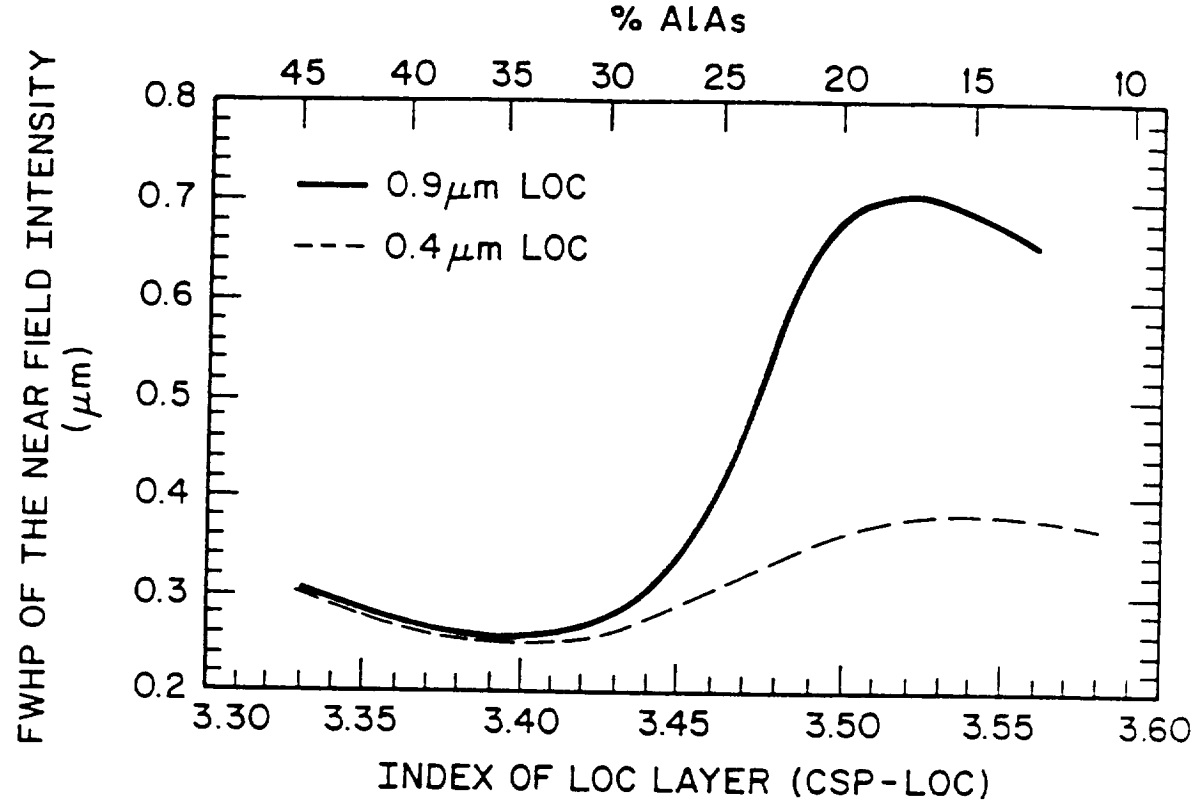
% AlAs
45 40 35 30 25 20 15 10
0.8
0.7
0.6
0.5
0.4
0.3
0.2
0.9μm LOC
0.4μm LOC
FWHP OF THE NEAR FIELD INTENSITY (μm)
3.30 3.35 3.40 3.45 3.50 3.55 3.60
INDEX OF LOC LAYER (CSP-LOC)

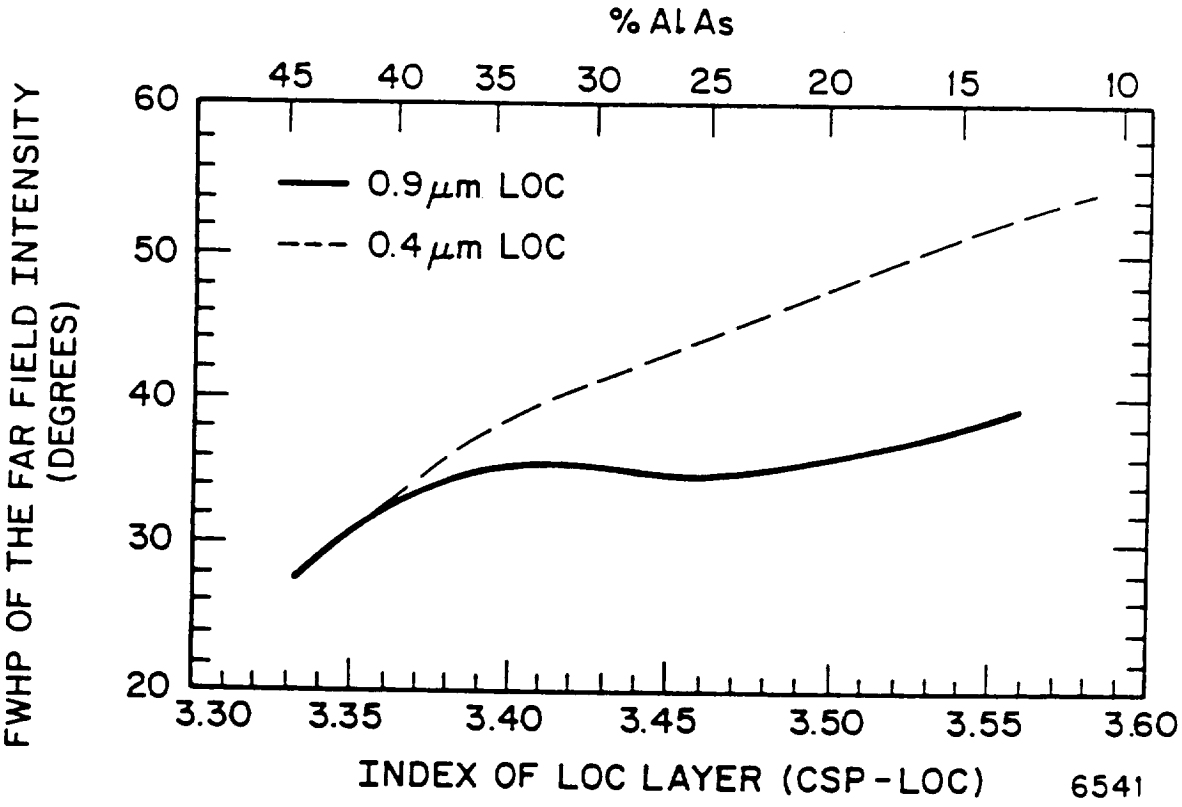
% AlAs
45 40 35 30 25 20 15 10
60
50
40
30
20
0.9μm LOC
0.4μm LOC
FWHP OF THE FAR FIELD INTENSITY (DEGREES)
3.30 3.35 3.40 3.45 3.50 3.55 3.60
INDEX OF LOC LAYER (CSP-LOC)
6541

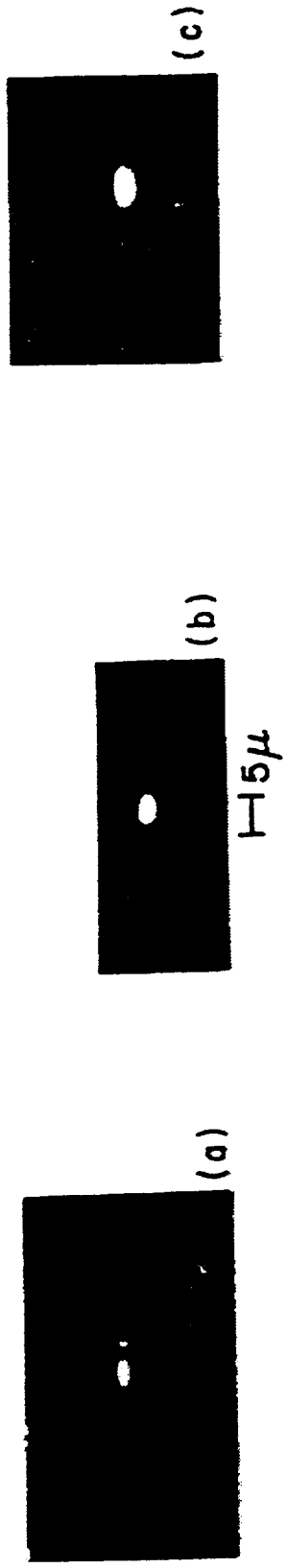

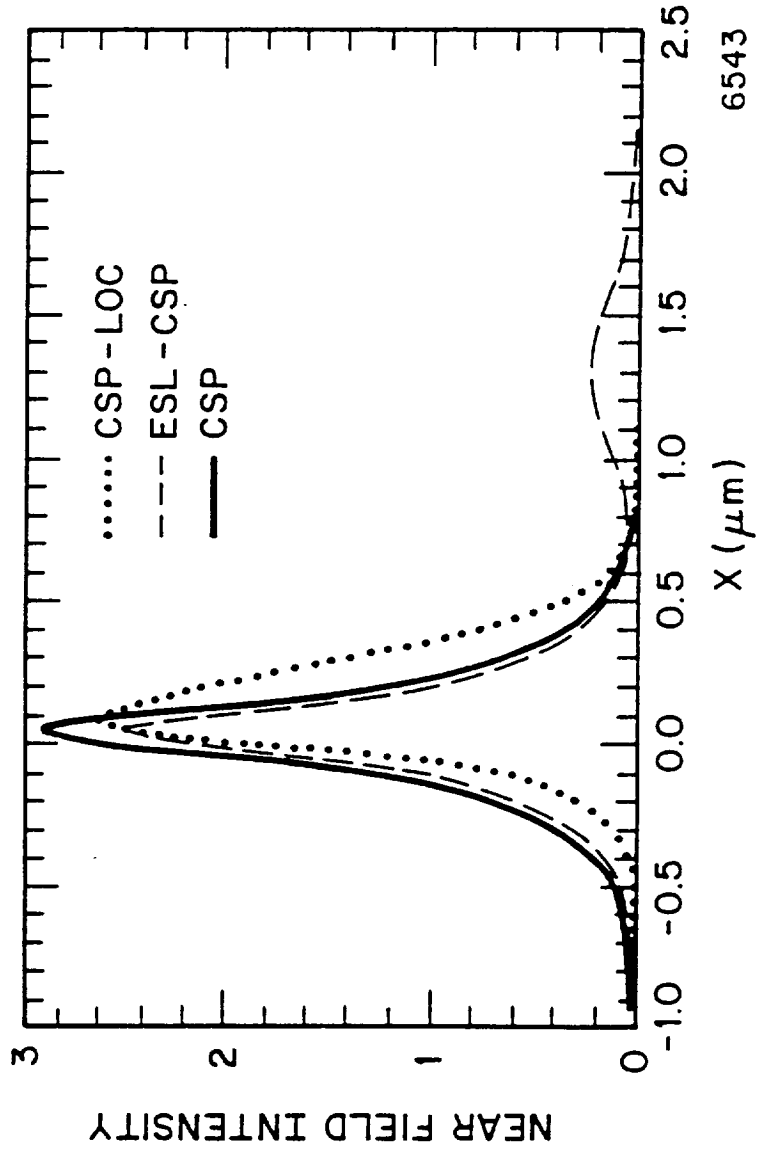
CSP-LOC
ESL-CSP
CSP
NEAR FIELD INTENSITY
X (μm)
6543
3
2
1
0
-1.0
-0.5
0.0
0.5
1.0
1.5
2.0
2.5

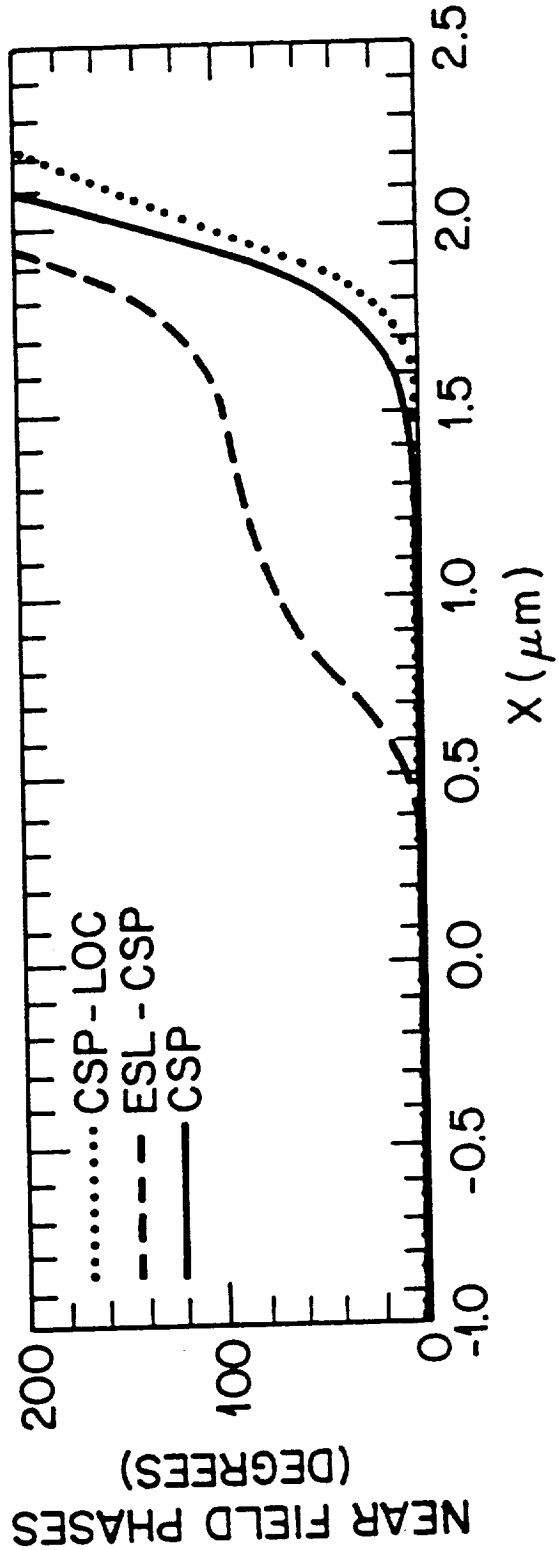
NEAR FIELD PHASES
(DEGREES)
200
100
0
-1.0
-0.5
0.0
0.5
1.0
1.5
2.0
2.5
X (μm)
CSP-LOC
ESL-CSP
CSP

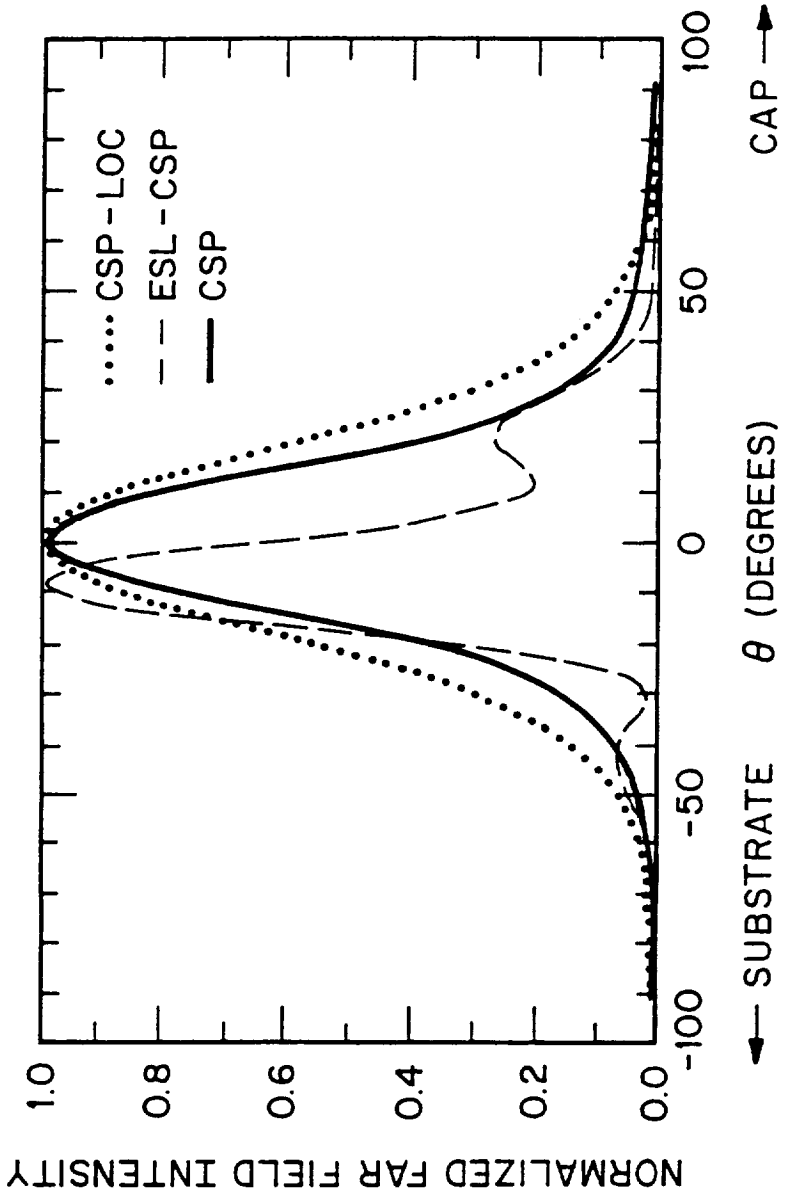
CSP-LOC
ESL-CSP
CSP
NORMALIZED FAR FIELD INTENSITY
1.0
0.8
0.6
0.4
0.2
0.0
-100
-50
0
50
100
SUBSTRATE
θ (DEGREES)
CAP

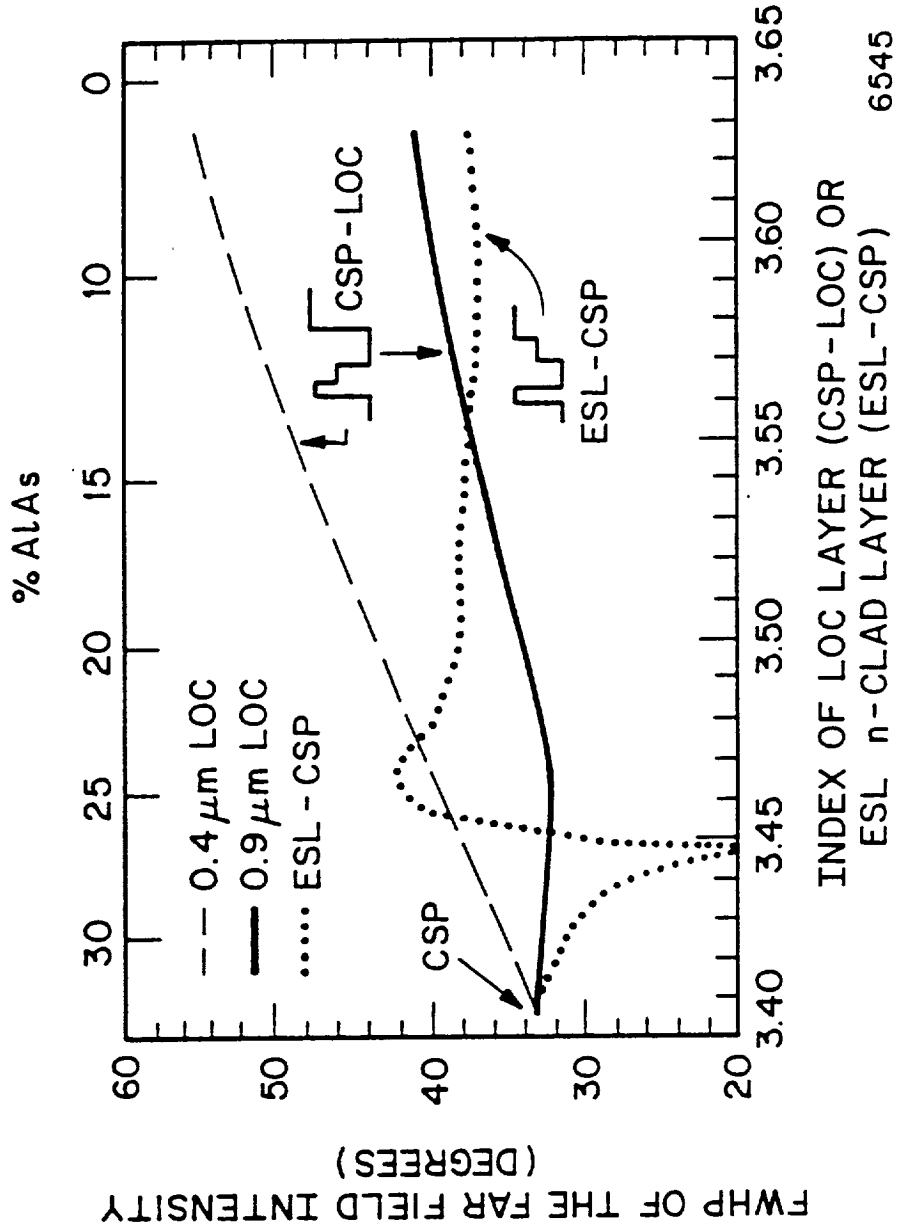
FWHP OF THE FAR FIELD INTENSITY
(DEGREES)
60
50
40
30
20
% AlAs
0
10
15
20
25
30
3.40
3.45
3.50
3.55
3.60
3.65
INDEX OF LOC LAYER (CSP-LOC) OR
ESL n-CLAD LAYER (ESL-CSP)
0.4 μm LOC
0.9 μm LOC
ESL-CSP
CSP-LOC
CSP
ESL-CSP
6545

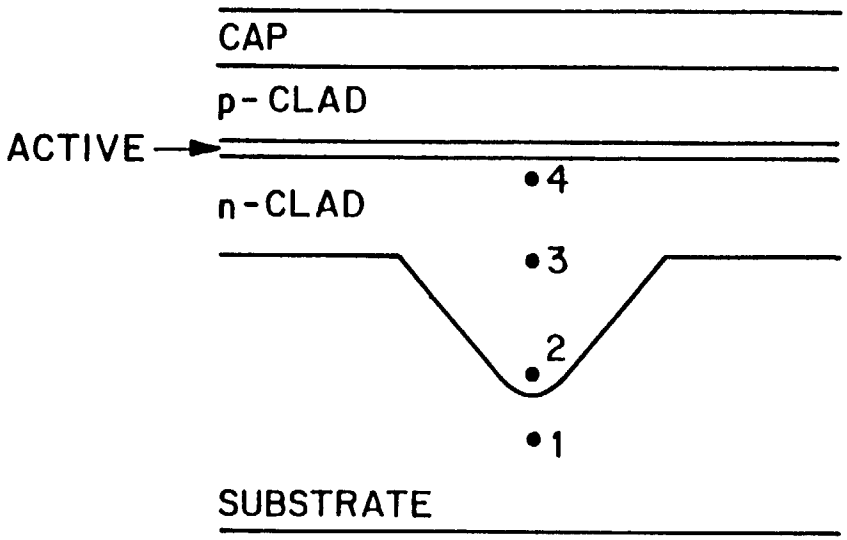


| FACET POSITION | COMPOSITION % Al | % Ga | % As |
|---|---|---|---|
| 1 | 0 | 50 | 50 |
| 2 | 14 | 35 | 53 |
| 3 | 20 | 29 | 52 |
| 4 | 18 | 32 | 52 |

6546

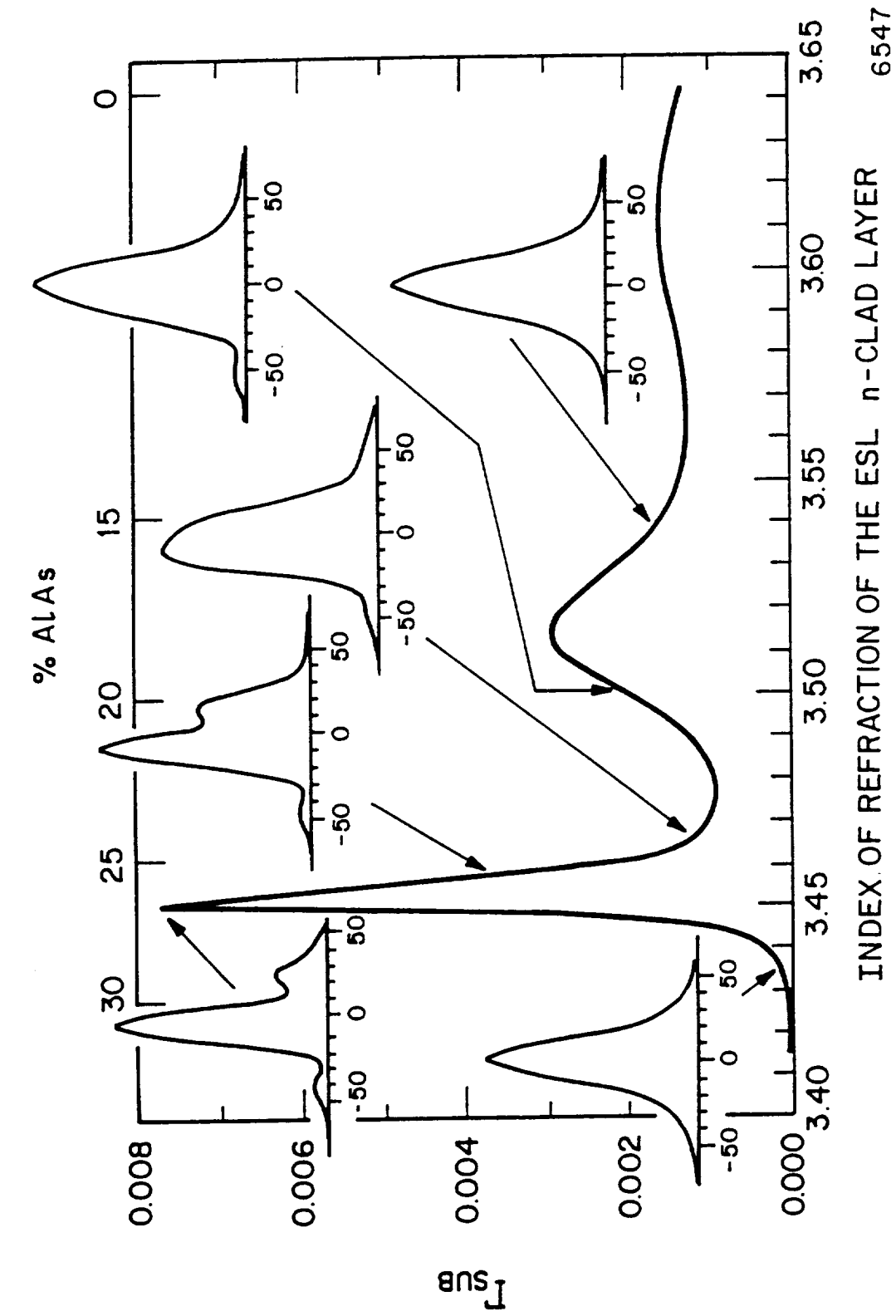
% AlAs
0
15
20
25
30
0.008
0.006
0.004
0.002
0.000
$\Gamma_{SUB}$
3.40
3.45
3.50
3.55
3.60
3.65
INDEX OF REFRACTION OF THE ESL n-CLAD LAYER
6547
-50
0
50

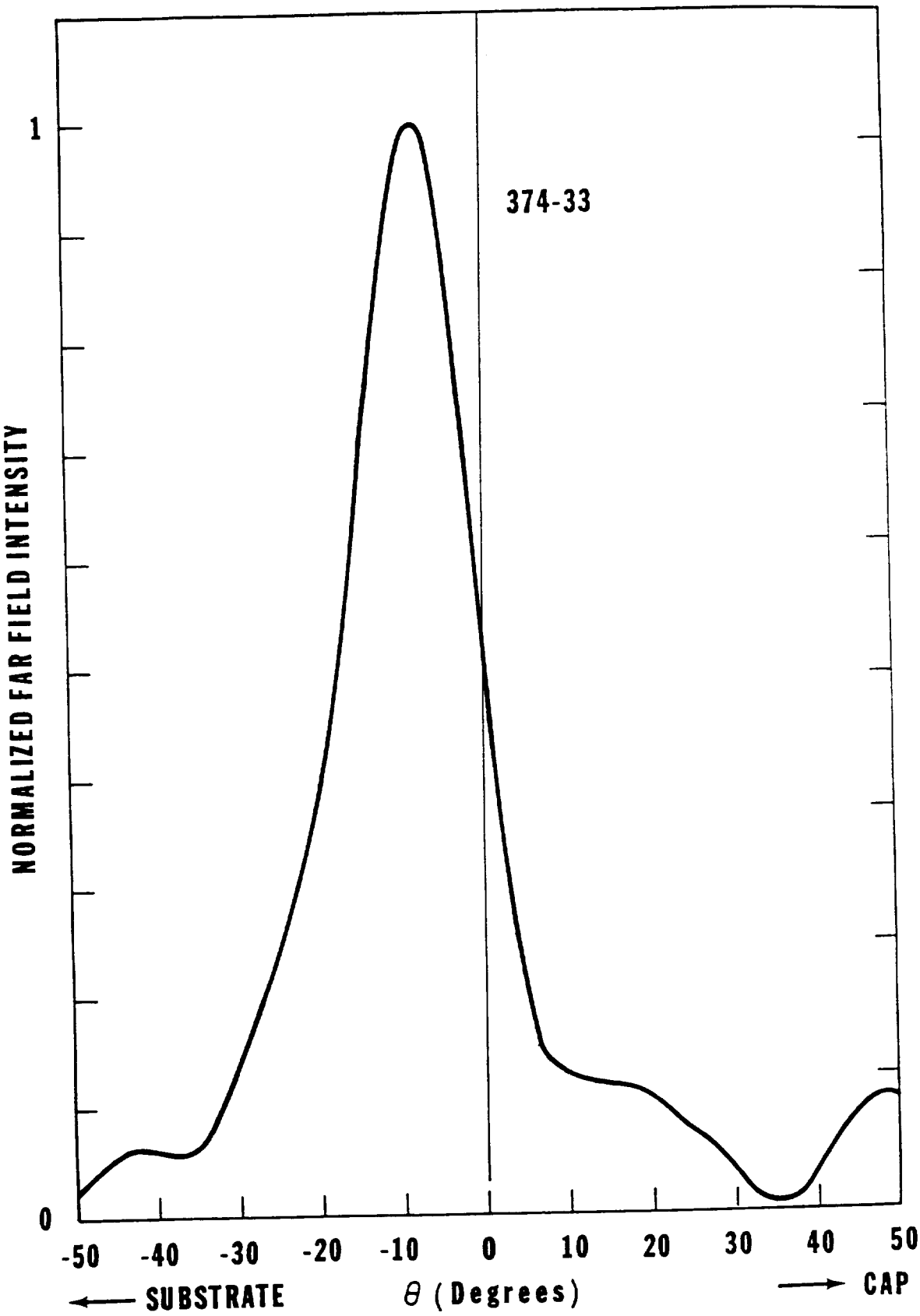
NORMALIZED FAR FIELD INTENSITY
1
0
374-33
-50
-40
-30
-20
-10
0
10
20
30
40
50
← SUBSTRATE
θ (Degrees)
→ CAP

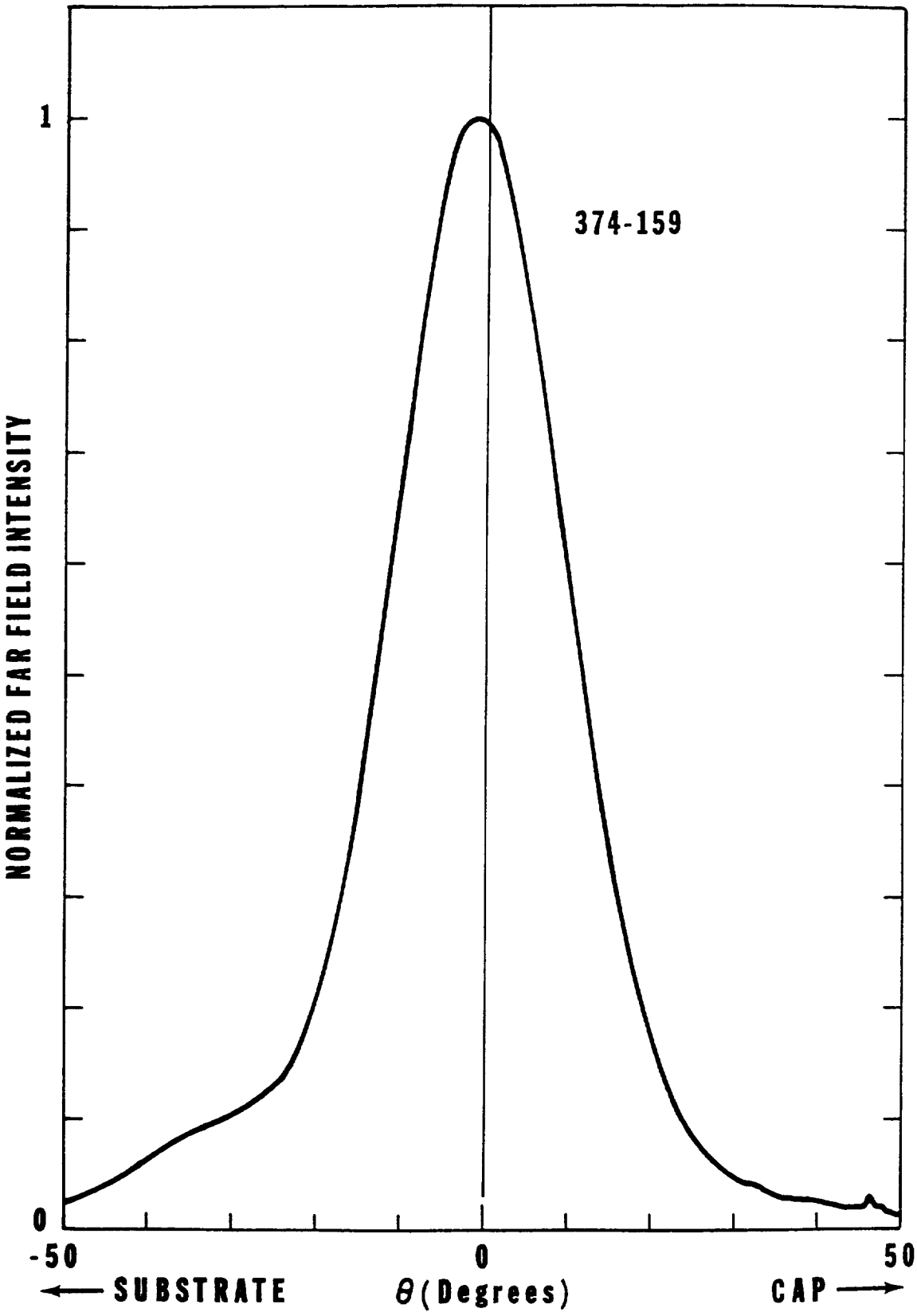
1
0
374-159
NORMALIZED FAR FIELD INTENSITY
-50
0
50
← SUBSTRATE
θ (Degrees)
CAP →

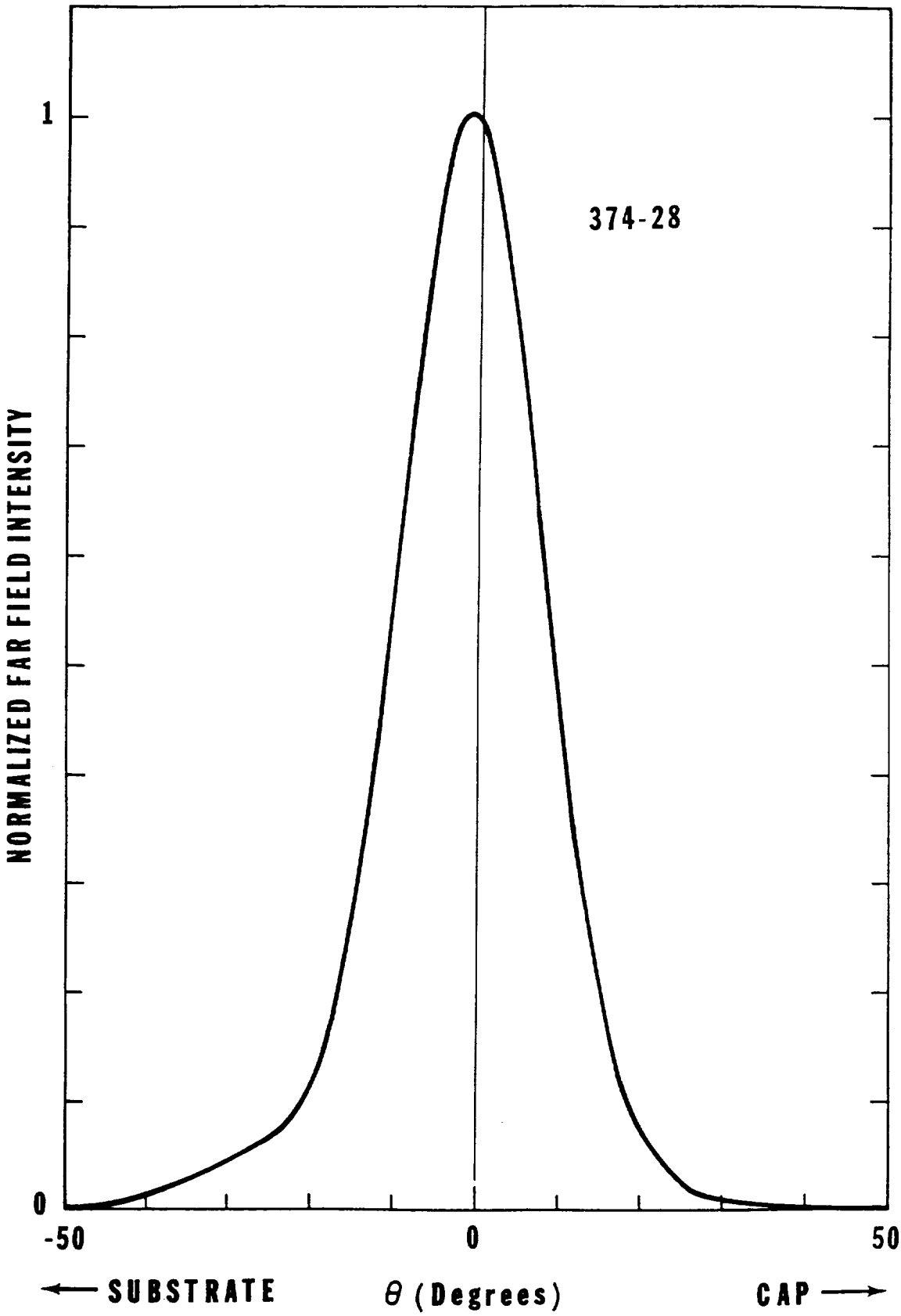
1
0
374-28
NORMALIZED FAR FIELD INTENSITY
-50
0
50
← SUBSTRATE
θ (Degrees)
CAP →

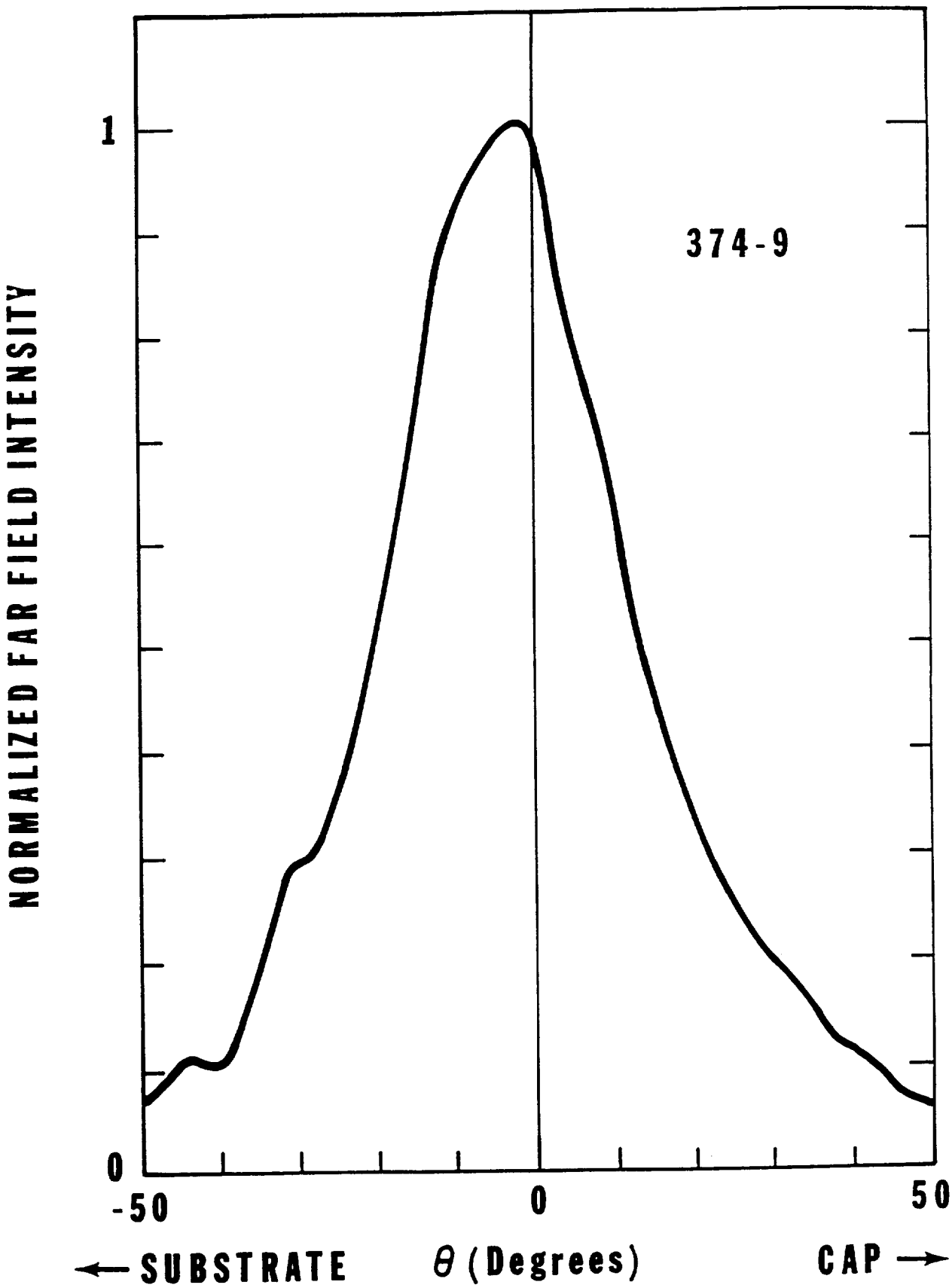
NORMALIZED FAR FIELD INTENSITY
1
0
374-9
-50
0
50
← SUBSTRATE
θ (Degrees)
CAP →

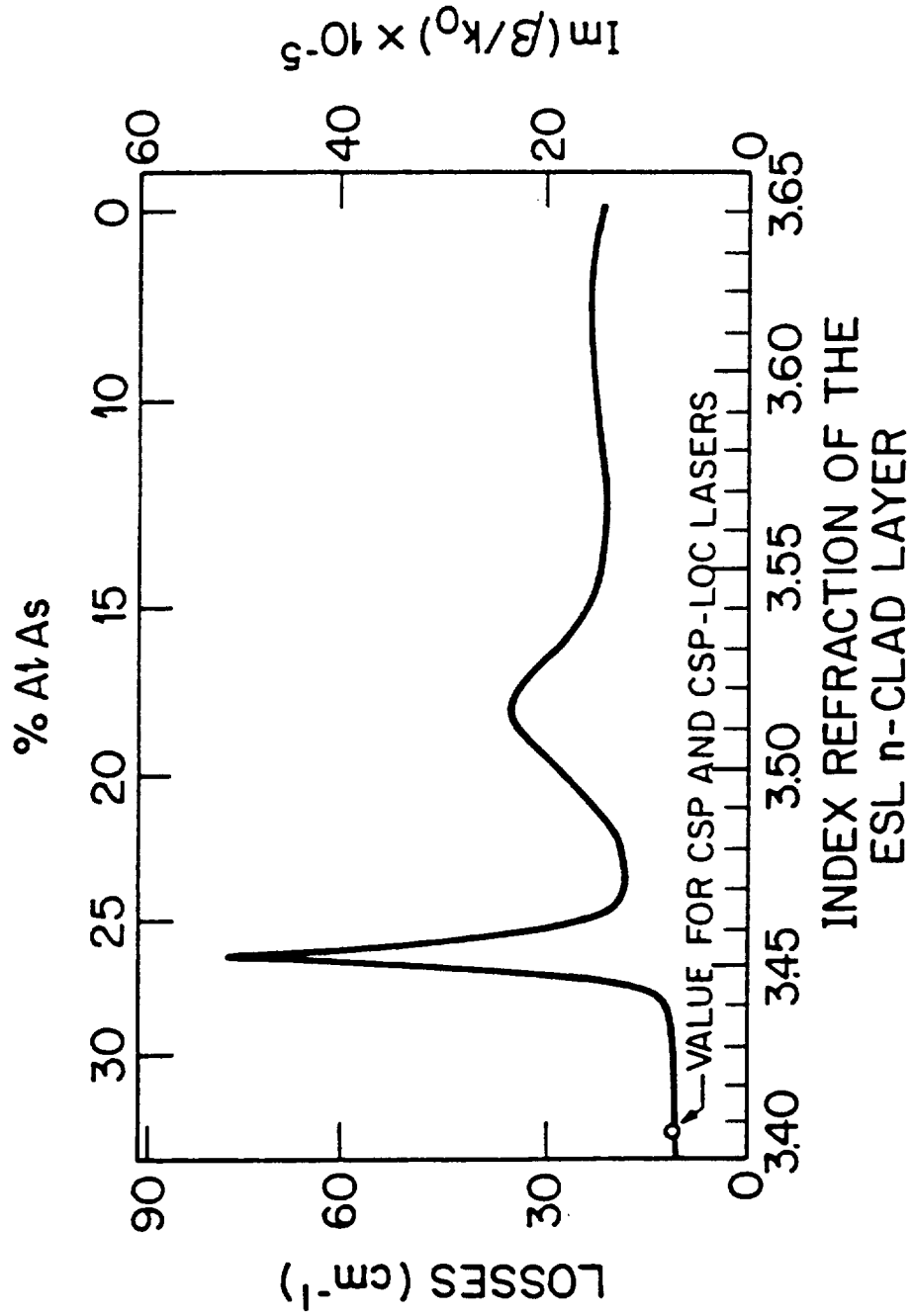
LOSSES (cm⁻¹)
90
60
30
0
% Al As
0
10
20
25
30
Im (β/k₀) × 10⁻⁵
60
40
20
0
3.40
3.45
3.50
3.55
3.60
3.65
VALUE FOR CSP AND CSP-LOC LASERS
INDEX REFRACTION OF THE
ESL n-CLAD LAYER

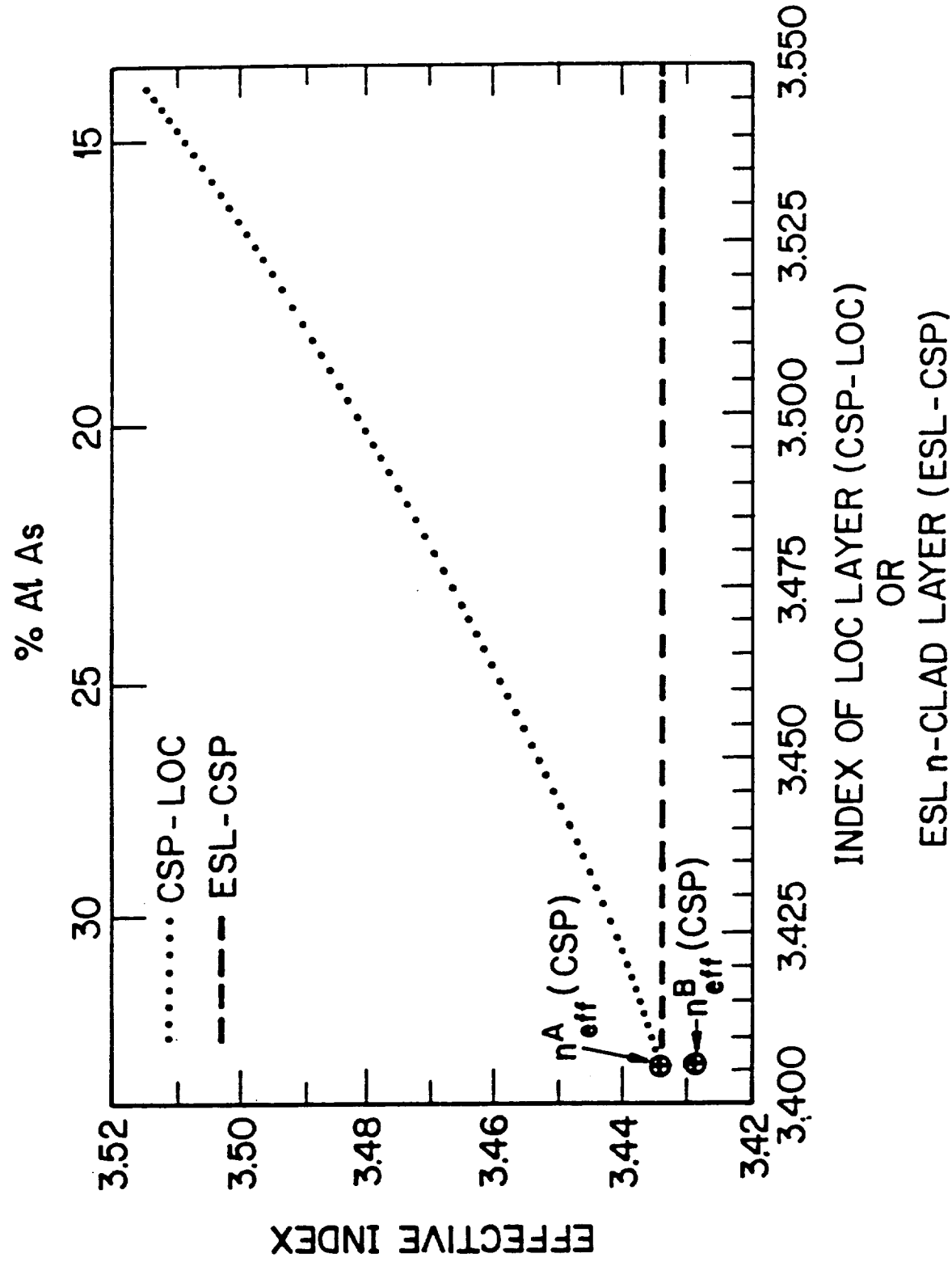
EFFECTIVE INDEX
3.52
3.50
3.48
3.46
3.44
3.42
% Al As
15
20
25
30
CSP-LOC
ESL-CSP
$n^A_{eff}$ (CSP)
$n^B_{eff}$ (CSP)
3.400
3.425
3.450
3.475
3.500
3.525
3.550
INDEX OF LOC LAYER (CSP-LOC)
OR
ESL n-CLAD LAYER (ESL-CSP)

# Appendix C

# Effects of Ion Sputtering on the Surface Composition of GaAs Laser Diode Facets

S. E. Slavin, A. R. Triano, and L. A. DiMarco

RCA Laboratories, Princeton, NJ 08540

## INTRODUCTION

In recent years ion sputtering has been investigated for application in various phases of opto-electronic device fabrication processes[1,2]. One principle interest involves the creation of a clean and stoichiometric GaAs surface for subsequent processing. Much of the previous work cited in the literature involves the use of some combination of ion sputtering and thermal annealing to produce high quality surfaces[3-8]. Temperatures on the order of several hundred degrees celsius are reportedly necessary to remove ion damage and recover surface stoichiometry[3-5,8]. Ion sputtering without any thermal treatment has generally resulted in deviations from stoichiometry[4-6,8-10].

We have examined argon ion sputtering for the purpose of removing the native oxide and any adsorbed impurities from the cleaved mirror facets of GaAs laser diodes prior to the deposition of passivation coatings[11]. Pre-deposition surface cleaning should result in increased adhesion of the facet coatings and improved device reliability. Unfortunately, the thermal sensitivity of the device structure at this advanced stage in the fabrication process precludes the possibility of high temperature annealing to restructure the surface after ion sputtering.

In the present study, we employ Auger spectroscopy to quantify changes in the surface composition of (011) GaAs generated by argon ion bombardment in the absence of any thermal annealing. Deviations from stoichiometry and surface oxide removal rates are examined for argon ion current densities between 0.02 and 0.04 mA/sq.cm. and ion energies in the range of 200 to 1000 eV.

## EXPERIMENTAL

The ion sputtering experiments were performed in a conventional Airco Temescal cryopumped electron beam deposition system with a base pressure of $10^{-7}$ torr. The ion source used was a broad beam type of the Kaufman design manufactured by the Commonwealth Scientific Corporation. Physical constraints within the deposition chamber resulted in placement of the ion gun at an angle of five degrees off normal to the sample surface. The argon flow rate to the ion source was adjusted via a mass flow controller to give an operating pressure of $10^{-4}$ torr during the ion sputtering process, without cold head valve throttling . A biased plasma probe with a grounded shield could be interchanged with the sample thus enabling in situ measurements of the ion current density prior to actual sample exposure to the beam.

A gate valve isolates the deposition system from an attached analytical chamber with a base pressure of $10^{-10}$ torr, containing a scanning Auger spectrometer (PHI model 15-110B) and a secondary electron detector (PHI model 04-202). A magnetically coupled linear-rotary feedthrough is used to transfer samples between the two systems, enabling Auger analysis of the ion sputtered samples without atmospheric exposure. A schematic diagram of the combined E-beam deposition and Auger analysis system is shown in figure 1.

Samples used in this investigation were cleaved in atmosphere from AlGaAs laser diode wafers grown by liquid phase epitaxy. Chemical cleaning was not employed prior to loading samples into the deposition system for ion sputtering. Each sample was examined in the analytical chamber via Auger spectroscopy prior to any ion sputtering. Subsequently they were transferred back to the deposition system and ion sputtered under a fixed set of conditions for a total time of 20 min. Ion sputtering was interrupted

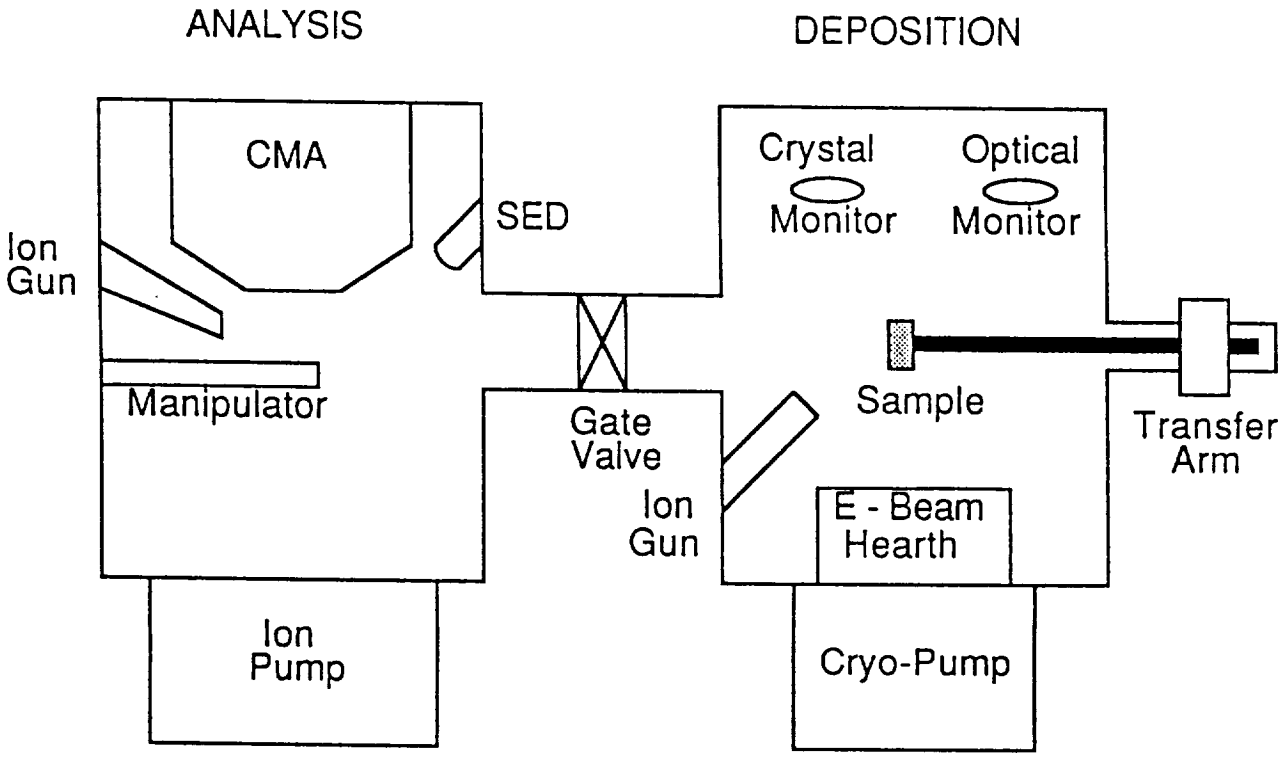


Figure 1 - Schematic diagram of the combined

E-beam deposition and Auger analysis system.

periodically to allow transfer of the sample back to the analytical chamber for examination.

Auger spectra were excited with a 5 KeV electron beam at a beam current of 150 nA. Two regions of each sample were analyzed and the compositional information averaged to obtain the gallium to arsenic ratios and oxide removal rates reported in this manuscript. The largest observed variation in either the gallium or arsenic concentration between two points on any single surface was one percent. Relative elemental sensitivity factors for gallium and arsenic were determined empirically by comparing the 351 eV silver peak height from an ion sputtered silver sample to the appropriate LMM gallium and arsenic peaks from in situ cleaved (011) GaAs samples run under identical conditions. The gallium and arsenic concentrations varied from stoichiometry by a maximum amount of 0.3 percent on these samples.

## DISCUSSION

Figure 2(a) shows an Auger spectrum, taken prior to ion milling, from one of the (011) GaAs facets that was cleaved in the atmosphere. Carbon and oxygen are the only impurities observed to be present on the samples surface before ion sputtering. Calculations indicate that the atomic ratio of gallium to arsenic on this surface is 1.03.

A spectrum from the same sample taken after 20 min of sputtering with 400 eV argon ions at a current density of 0.03 mA/sq.cm. is shown in Figure 2(b). Examination of this spectrum reveals that the carbon has been removed entirely, while trace amounts of oxygen still remain on the sample's surface. The inability to completely remove oxygen is likely due to adsorption of residual water in the deposition system prior to the transfer operation. Trace amounts of argon are also observed to be present after sputtering. In this particular case, calculations indicate that the argon ion bombardment has caused

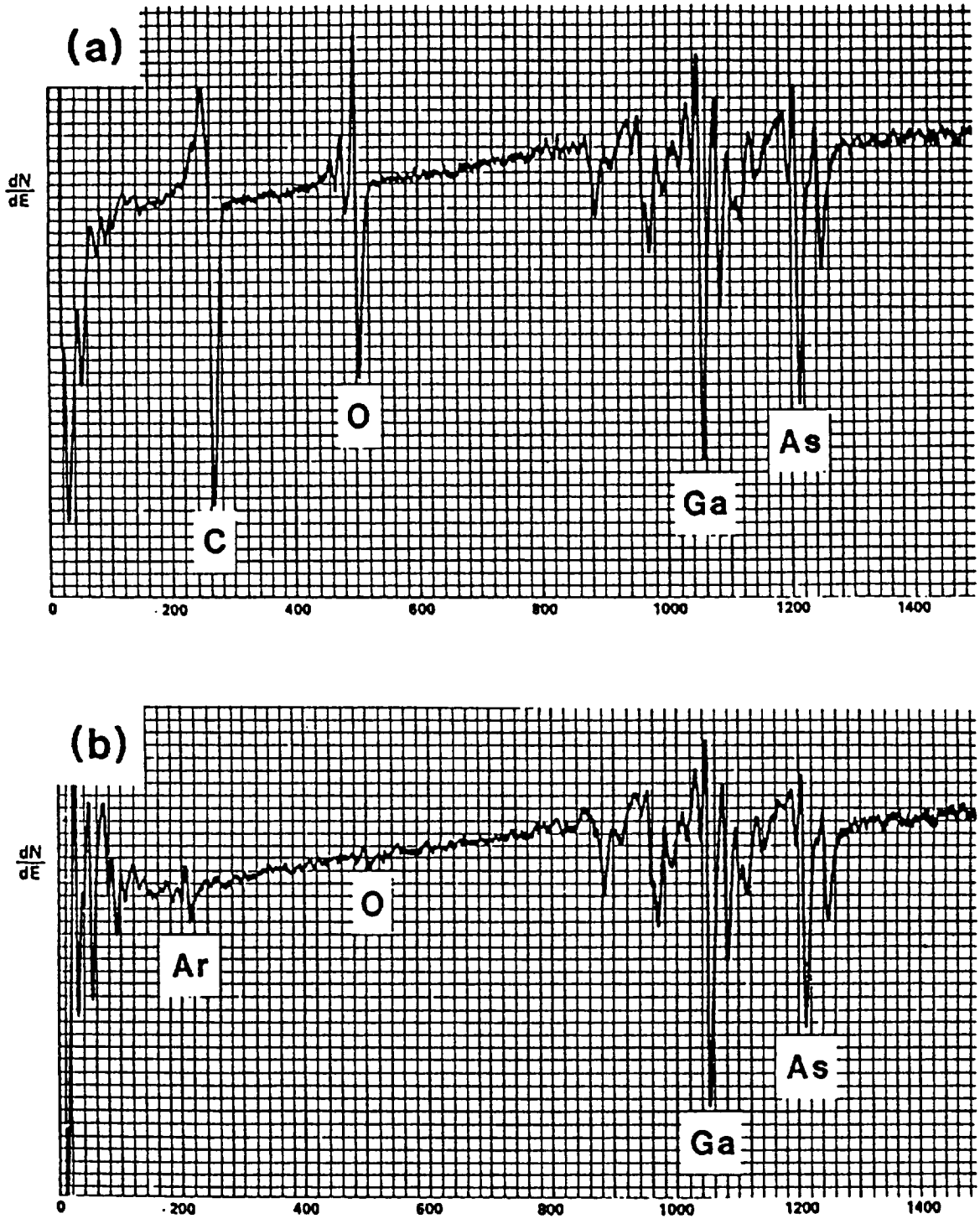


Figure 2 - (a) Auger spectrum from an (011) GaAs sample cleaved in atmosphere, taken prior to ion sputtering. (b) Auger spectrum from the same sample after 20 min. of sputtering with 400 eV argon ions at a current density of 0.03 mA/cm$^2$.

the gallium to arsenic atomic ratio to increase to 1.2.

Gallium to arsenic ratios after 20 minutes of ion sputtering at two different current densities are plotted against the argon ion energy in Figure 3. Examination of this figure reveals that the magnitude of the gallium surface enrichment increases with increasing argon ion energy over the entire range of ion energies investigated. The steady state surface compositions, which were obtained for total sputtering times greater than 10 min, did not appear to vary systematically with the ion current density.

Preferential sputtering in GaAs has been examined by several researchers under a variety of ion sputtering conditions[9,10]. Ion-energy dependent gallium surface enrichment on (100) oriented GaAs, for ion energies above 600 eV, has been observed previously[12]. The fact that no deviations from stoichiometry were seen at lower ion energies was attributed to insufficient penetration of the argon ions into the GaAs lattice. Calculations using the LSS method[13] imply that at energies below 600 eV the argon ion range in gallium arsenide is on the order of the LMM electron escape depths[14]. Structural and electronic damage may well extend to even greater depths[15]. We therefore expect to observe deviations from stoichiometry at ion energies below 600 eV.

Our data suggests that gallium surface enrichment, whose magnitude is proportional to the ion energy, is occuring at ion energies as low as 200 eV on (011) GaAs. Differences in the surface binding energy of gallium and arsenic, as shown by the volitility of arsenic, should result in differences in the energy dependence of the partial sputtering yields. It is therefore not surprising to observe ion-energy dependent surface enrichment at energies as low as 200 eV, which is substantially above the sputtering threshold (approximately 35 eV).

Figure 4 shows a plot of the normalized oxygen peak height vs. the ion sputtering time for 1000 eV argon ions at three different ion current densities. The rate at which

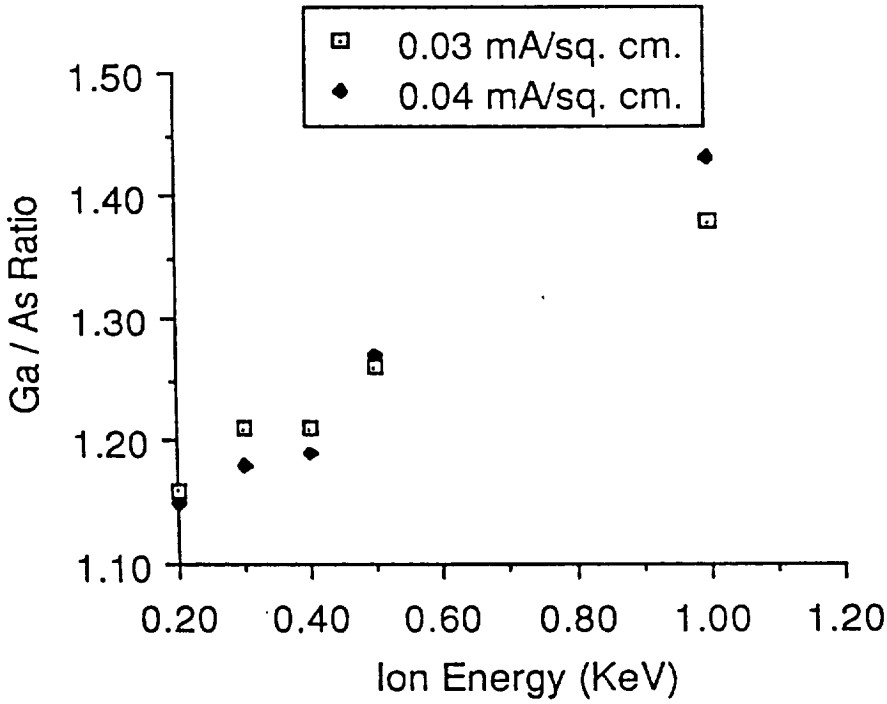


Figure 3 - Ga / As Ratio After 20 Min. of Ion Sputtering

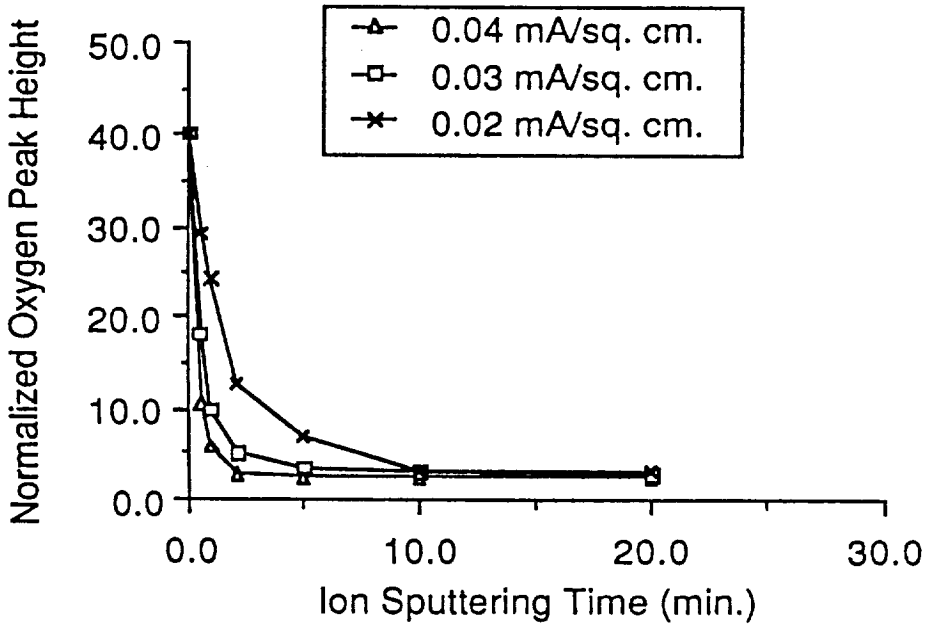


Figure 4 - Oxygen Removal Rates for 1000 eV Argon Ions.

oxygen is removed from the surface is clearly proportional to the ion current density as expected. Similar results are observed at ion energies between 200 and 1000 eV.

An estimate of 10 Å for the native oxide thickness was determined based on the sputter rates of $Al_2O_3$ and $Ta_2O_5$ standards. Using this thickness, oxide removal rates of approximately 1,2,and 5 Å/min. were obtained for ion current densities of 0.02, 0.03, and 0.04 mA/sq. cm. respectively. The tracking of the gallium and oxygen concentrations during sputtering was suggestive of a gallium-rich mixed oxide. The oxide composition and thickness estimates compare favorably with those observed previously[16].

## SUMMARY

Argon ion sputtering has been examined as a method of cleaning the cleaved mirror facets of AlGaAs diode lasers prior to the application of passivation coatings. Auger electron spectroscopy was employed to monitor the surface composition at various intervals during the sputtering process. Prior to sputtering, the cleaved (011) surfaces were found to contain carbon and oxygen. After sufficient ion sputtering to obtain steady state surface compositions, trace amounts of argon and oxygen remained on the surfaces. Quantitative analysis involving the magnitudes of the gallium and arsenic LMM electron transitions revealed that the ion sputtered surfaces show evidence of gallium enrichment whose magnitude appears to be proportional to the ion energy. The oxygen removal rates, on the other hand, show a first order dependence on the argon ion current density.

## ACKNOWLEDGEMENT

The authors wish to express their gratitude to Drs. M. Ettenberg, J. H. Thomas III and C. W. Magee for many useful discussions during the preparation of this manuscript.

# REFERENCES

[1]W. Chen, L. M. Walpita, C. C. Sun, and W. S. C. Chang, J. Vac. Sci. Technol. B **4** (3), 701 (1986).

[2]G. A. Lincoln, M. W. Geis, S. Pang, and N. N. Efremow, J. Vac. Sci. Technol. B **1** (4), 1043 (1983).

[3]J. Massies, P. Devoldere, and N. T. Linh, J. Vac. Sci. Technol. **15** (4), 1353 (1978).

[4]K. Jacobi and W. Ranke, J. Elect. Spect. and Rel. Phenom. **8**, 225 (1976).

[5]S. Sinharoy and R. A. Hoffman, IEEE Trans. Elect. Dev. **31** (8), 1090 (1984).

[6]P. Drathen, W. Ranke, and K. Jacobi, Surf. Sci. **77**, L162 (1978).

[7]W. Ranke and K. Jacobi, Prog. Surf. Sci. **10**, 1 (1981).

[8]P. Oelhafen, J. L. Freeouf, G. D. Pettit, and J. M. Woodall, J. Vac. Sci. Technol. B **1** (3), 787 (1983).

[9]Topics in Applied Physics, Vol. 52, Sputtering by Particle Bombardment II, Edited by R. Behrisch, (Springer-Verlag, Berlin, 1983), pp. 73

[10]I. L. Singer, J. S. Murday, and L. R. Cooper, J. Vac. Sci. Technol. **15** (2), 725 (1978).

[11]I. Ladany, M. Ettenberg, H. F. Lockwood, and H. Kressel, Appl. Phy. Lett. **30,** 87 (1977).

[12]A. van Oostrom, J. Vac. Sci. Technol. **13** (1), 224 (1976).

[13]J. Lindhard, M. Scharff, and H. E. Schiott, Kgl. Danske Videnskab. Selskab, Mat-Fys. Medd. **33** (14), (1963).

[14]G. Ertl and J. Kuppers in: Low Energy Electrons and Surface Chemistry, (Chemie, Weinheim, 1974).

[15]Y. Sekino, M. Owari, M. Kudo, and Y. Nehei, Jap. J. Appl. Phys. **25** (4), 538 (1986).

[16]S. P. Kowalczyk, J. R. Waldrop, and R. W. Grant, J. Vac. Sci. Technol. **19** (3), 611 (1981).

## FIGURE CAPTIONS

Figure 1 - Schematic diagram of the combined E-beam deposition and Auger analysis system.

Figure 2 - (a) Auger spectrum from an (011) GaAs sample cleaved in atmosphere, taken prior to ion sputtering. (b) Auger spectrum from the same sample after 20 min. of sputtering with 400 eV argon ions at a current density of 0.03 $mA/cm^2$.

Figure 3 - Ga/As atomic ratio after 20 minutes of ion sputtering.

Figure 4 - Oxygen removal rates for 1000 eV argon ions.

# Appendix D

# Intrusions in the Active Layer of CSP Lasers

S. E. Slavin
F. Z. Hawrylo
J. J. Hughes

## ABSTRACT

CSP laser diodes from various wafers were observed to develop a node or dark spot in their near-field patterns after failure during lifetesting. "Node" devices from each wafer were angle lapped and stained in an attempt to uncover a physical mechanism for this common failure symptom. Optical microscopic examination of the beveled cross sections revealed that an intrusion, in the form of a spike at the tip of the zinc diffusion front, had penetrated into the active layer of these diodes. The node observed in the near-field pattern appears to be in a position corresponding to the location of the spike in the active region.

In addition, cathodoluminescence measurements on other "node" diodes revealed a dark line defect approximately 2 μm wide running parallel to and in the middle of the 5 μm contact stripe. We believe that this dark line defect is representative of a region of non-radiative recombination which occurs in the portion of the active layer containing the intrusion.

## Introduction

The diffusion of zinc into gallium arsenide and aluminum gallium arsenide is an important part of the fabrication process of various electronic and optoelectronic devices [1-10]. In stripe geometry laser diodes, the zinc diffused region provides additional current confinement and improved ohmic contacting with the external metallization. Reliability studies performed by various researchers[11-14] have suggested that the presence of zinc in some way contributes to the degradation of laser diodes. Various mechanisms have been postulated in an attempt to explain this phenomenon.

The present study was undertaken in response to the observation of a common failure symptom which was seen during lifetesting of CSP laser diodes from various wafers. These devices developed a node or dark spot in their near-field patterns after lifetest failure. An example of a typical pre-lifetest near-field pattern is shown twice on the left side of Figure 1(a). The right side of this figure shows the linear intensity scans of the lateral and transverse mode patterns. The gaussian intensity profile is characteristic of single spatial mode lasers. Figure 1(b) shows the post-lifetest near-field pattern and lateral mode pattern intensity scan from the same laser diode. The reduced intensity at the center of the pattern in Figure 1(b) is the feature referred to as a node.

Several "node" devices from different wafers were chosen for examination an attempt to isolate a single common physical feature which would account for the observed node development.

## Sample Preparation

### A) Beveled Cross Sections

One degree angle lapping was the method chosen to prepare the samples for examination via optical microscopy. This procedure produces a 57 X magnification of the epilayer structure in one dimension. Figure 2 shows a schematic representation (not to scale) of a laser diode and the direction of the one degree bevel surface relative to the device structure.

Individual laser diodes are removed from their heat sinks, stripped of their solder layers, and wax mounted on one edge of a steel angle block. Gallium arsenide feedstock material is mounted adjacent to the device to protect it during the polishing process. A piece of sapphire is affixed to the opposite side of the block to provide the desired bevel angle. A schematic representation of the angle block containing the mounted components is seen in Figure 4. Angle lapping is done on a spiral-grooved tin wheel charged with one micron diamond grit. The bevel angle is measured with an autocollimator, which bounces a collimated beam of light off the back surface of the angle block onto a scale calibrated in minutes of arc.

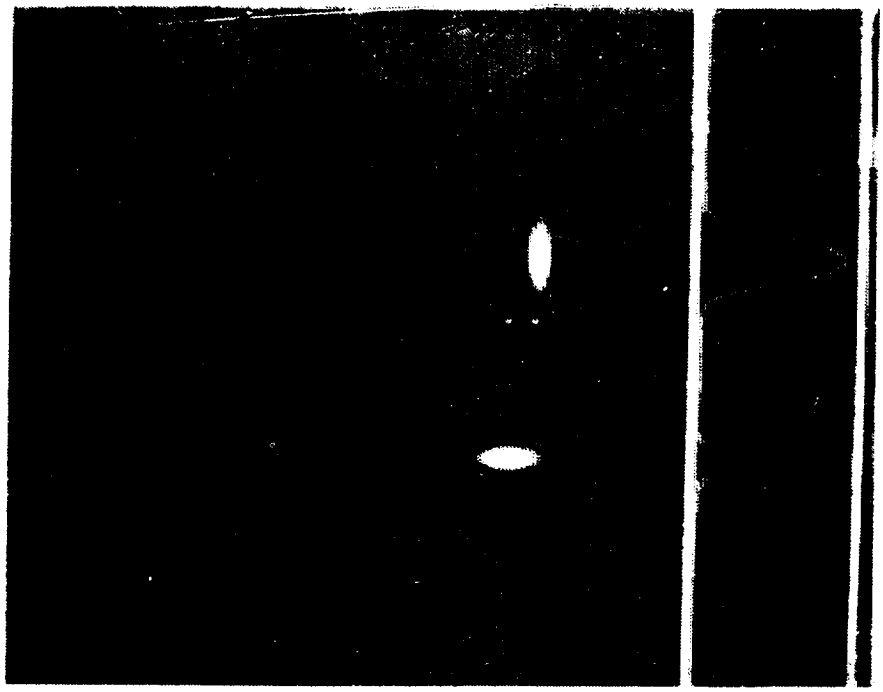


Figure 1(a) - Pre-lifetest near-field patterns (left) and intensity scans (right)

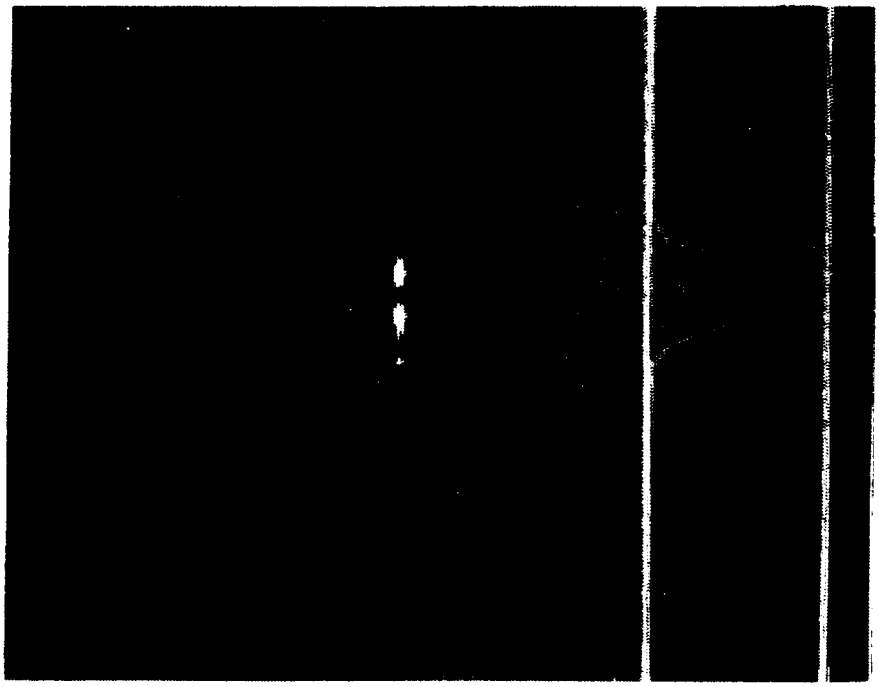


Figure 1(b) - Post-lifetest near-field pattern (left) and intensity scan (right)

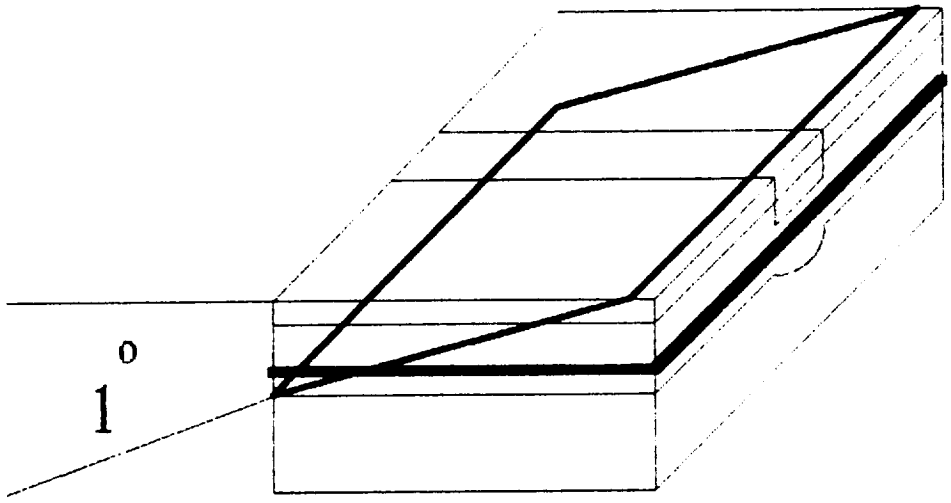


Figure 2 - Schematic representation (not to scale) of a CSP laser diode showing the one degree angle lap cross section plane.

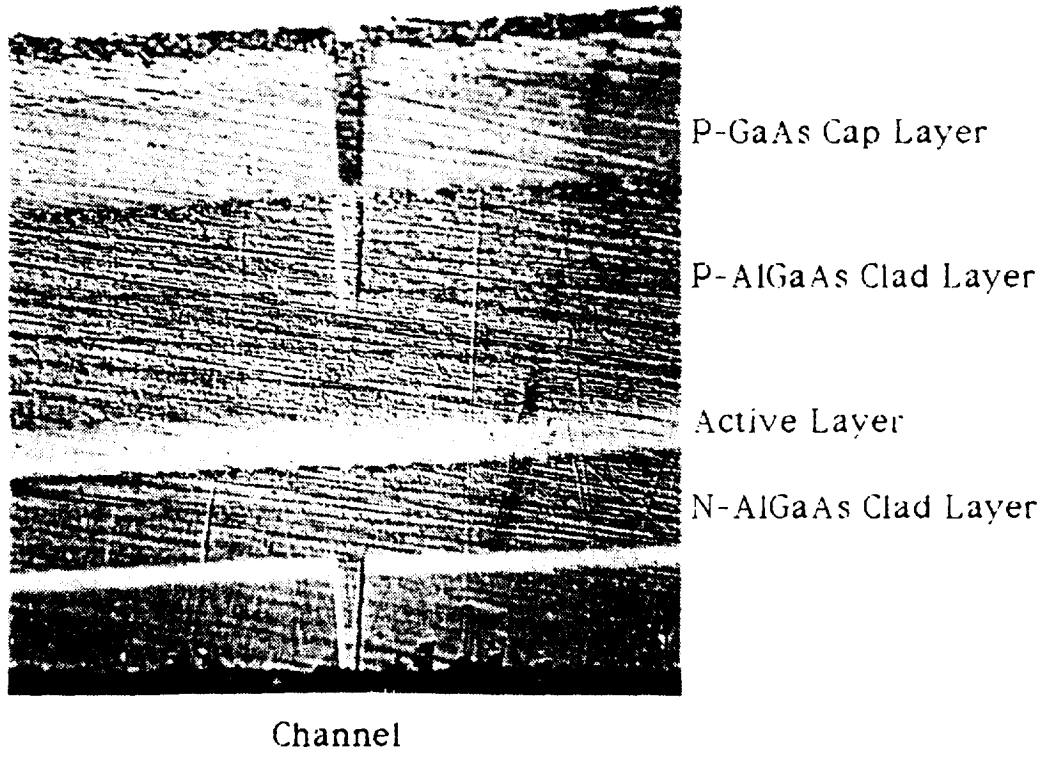


Figure 3 - 500 X photomicrograph of a stained angle lapped cross section of a good CSP laser diode

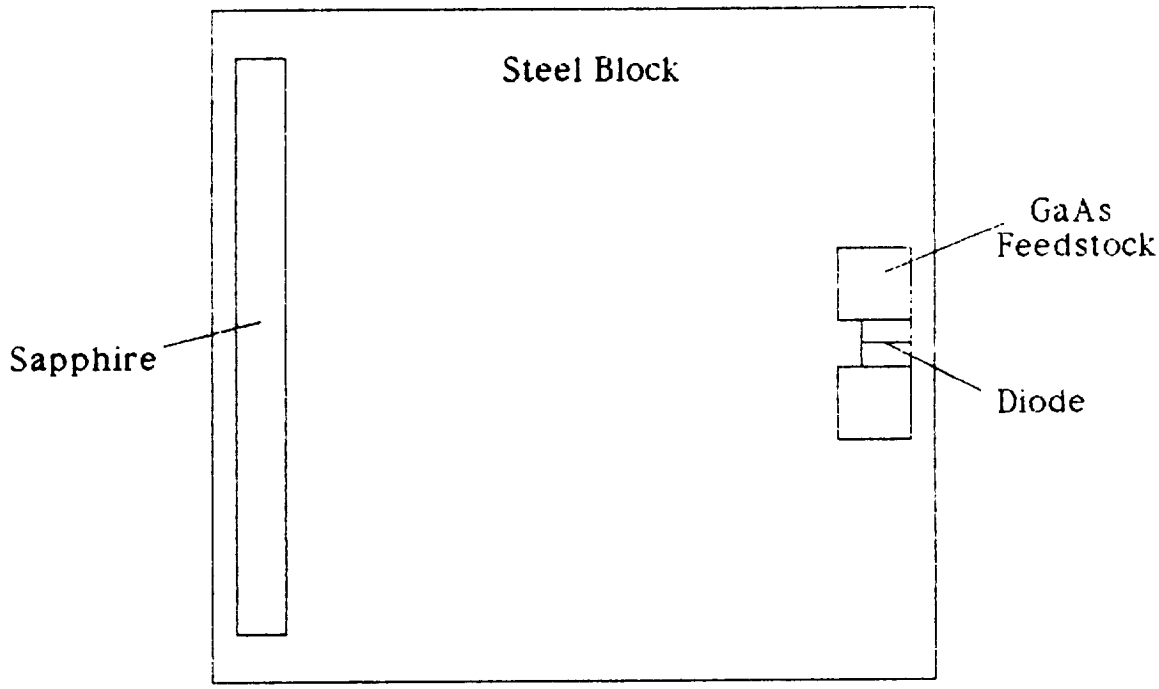


Figure 4 - Schematic representation of the angle block structure

A two component "AB" etchant[15] is used to delineate the epilayer structure on the beveled surface of the diode. The optical micrograph in Figure 3 shows the device structure revealed on the polished surface of a working laser diode after staining.

B) Cathodoluminescence Samples

Samples for cathodoluminescence analysis are prepared by removing the device from the heat sink and stripping the contact metals from the p-surface to expose the p-GaAs cap layer. Etching of the cap layer in the zinc diffused stripe region is achieved using a $K_3FeCN_6$-KOH etchant. Five to ten seconds of exposure to the etchant is generally sufficient to generate pits in the stripe which extend through the p-GaAs cap layer into the p-AlGaAs clad layer. The differing aluminum contents of the various epilayers enables the use of energy dispersive x-ray analysis to estimate the location of the base of an etch pit in the laser diode structure.

## Discussion

Shown in Figure 5 is a stained angle lapped cross section of a laser diode which had developed a node in its near-field pattern after failure during lifetesting. The two problematic features which can be observed in this micrograph are the proximity of the zinc diffusion front to the active layer and the spike which protrudes from the tip of the diffusion front into the cavity. As seen in Figure 3 (good device), a separation distance greater than 0.5 m is desired between the active layer and the zinc diffusion front in the CSP laser structure. A beveled cross section of a diode from another wafer which produced devices that failed via node formation is shown in Figure 6. This particular device was never operated prior to its being angle lapped and stained. The micrograph reveals that prior to operation, this device possesses a zinc diffusion front that is immediately adjacent to the active layer. The major structural difference between the devices in Figures 5 and 6 is that the lifetested device contains an intrusion in the active layer in the form of a spike at the tip of the diffusion front. Examination of the post-life near-field patterns

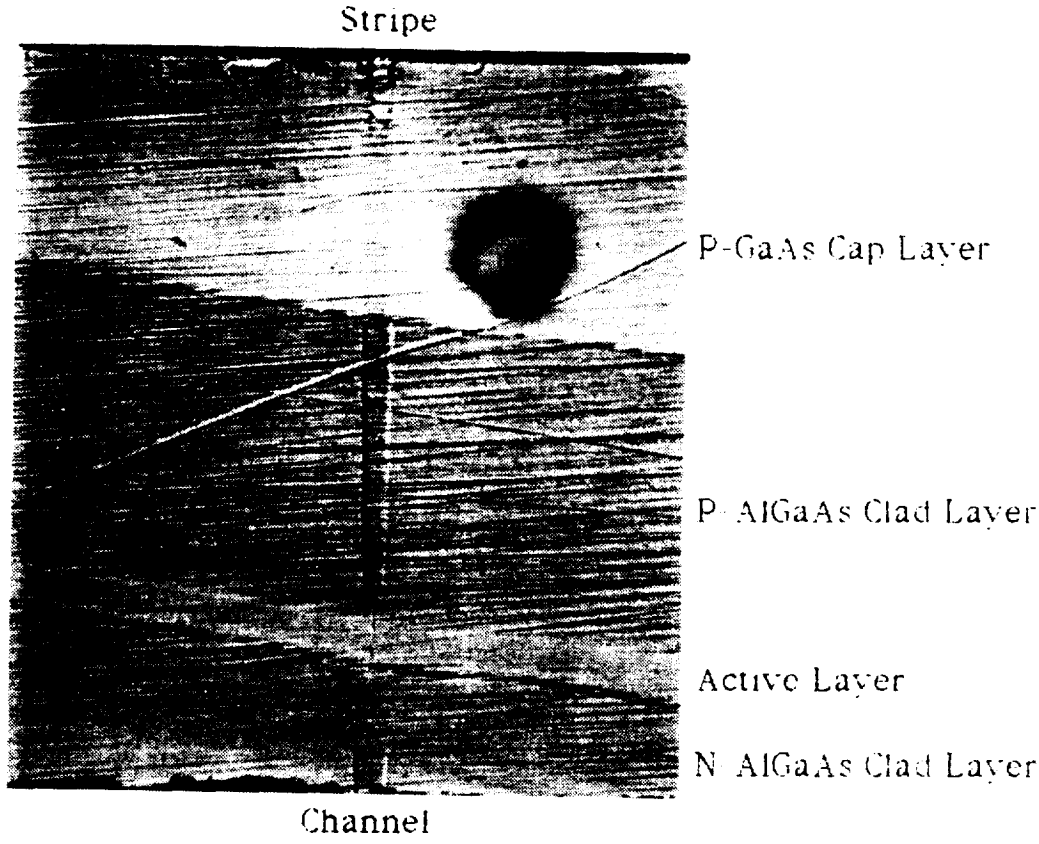


Figure 5 - 500 X photomicrograph of a stained angle lapped cross section of a failed CSP laser diode containing a spike in the active layer

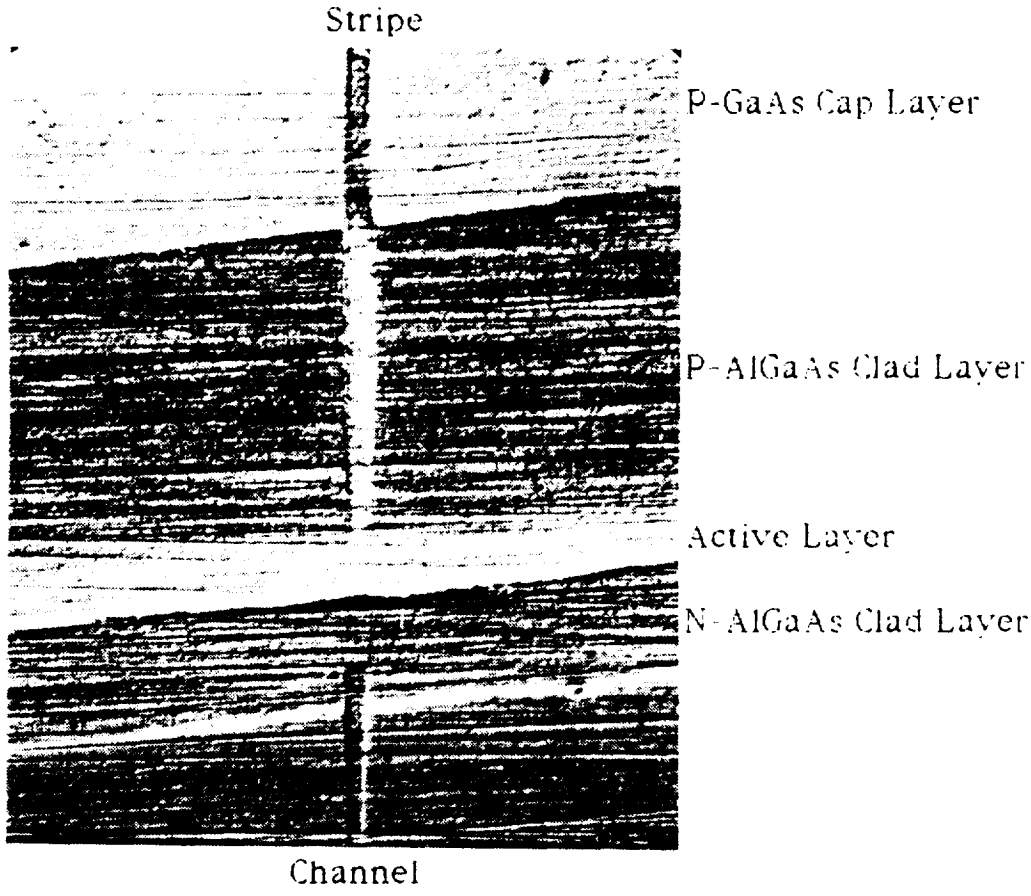


Figure 6 - 500 X photomicrograph of an angle lapped cross section of a CSP laser diode which was not operated prior to beveling and staining

from several node devices reveals that the node which develops during lifetesting appears to be in a position which corresponds to the location of the spike in the active layer. This evidence suggests that the spike forms during the operation of the laser diode and is involved in its degradation.

Supplementary information about this failure mode has been obtained via cathodoluminescence analysis of diodes that developed a node after lifetest failure. The micrographs in Figure 7 show the corresponding secondary electron image and the cathodoluminescence image of one such device. A dark line defect is seen in the center of the stripe along its entire length in the cathodoluminescence image. The dark line is most obvious in the stripe etch pits and at the ends of the stripe. Energy dispersive x-ray analysis revealed that aluminum is present at these locations, and we therefore conclude that the etchant has opened up optical windows into the p-AlGaAs clad layer in these areas. Little or no aluminum was detected outside of the stripe region, indicating the continued presence of some portion of the p-GaAs cap layer. A high-pass filter that transmits photons with wavelengths greater than 780 nm was placed between the sample and the detector to ensure that any observed radiation originated in the active layer.

A more highly magnified SEM micrograph of the largest etch pit towards the center of the stripe is seen in Figure 8. A cathodoluminescence image of this same etch pit and the adjacent one is shown in Figure 9. A dark line defect which is in the center of the stripe and runs parallel to it is observed in the pit. Absorption of photons originating in the active layer by zinc in the stripe region above can be ruled out as the cause of the dark line, since the dark line does not cover the full width of the zinc diffused stripe. The position of the dark line in the stripe corresponds to the location of the node in the near-field pattern.

Figure 7 - SEM micrographs of a GaP layer grown on a GaP substrate etched at -50 and a dark line defect.

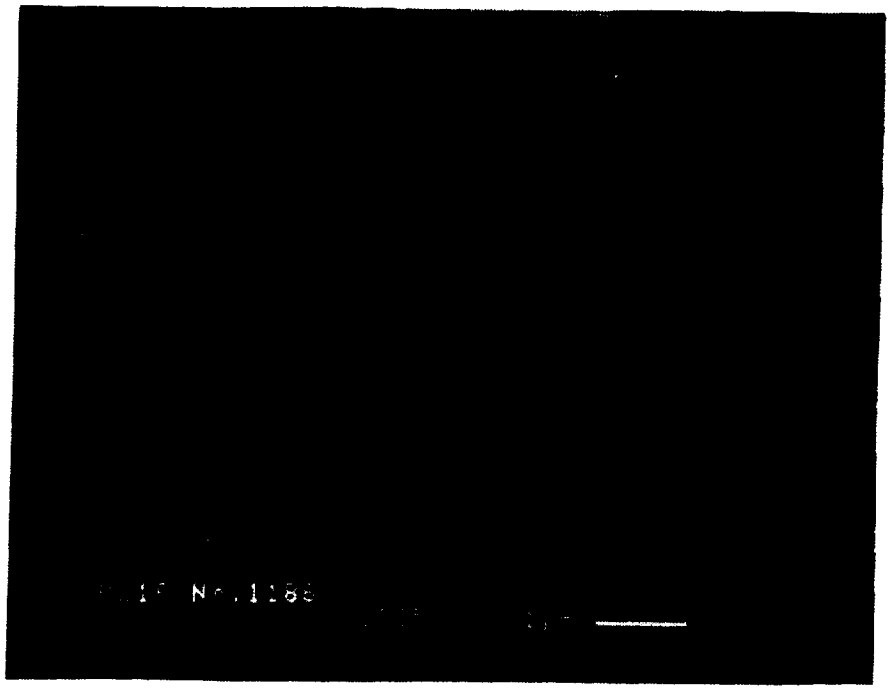

Figure 8 - SEM micrograph of the largest etch pit in the center of the stripe of the diode shown in figure 7

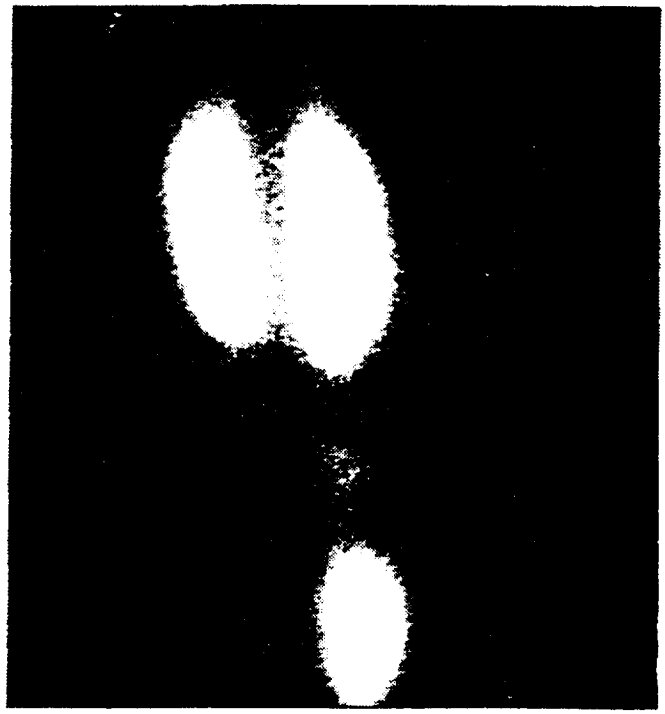

Figure 9 - 3600 X cathodoluminescence image of the largest etch pit and the adjacent etch pit in center of the stripe of the diode shown in figure 7

## Summary

The fact that the position of a node in the near-field pattern corresponds to the location of either a spike in the active layer or a dark line defect in the stripe, strongly suggests that the three features are related and involved in the degradation of these devices. Observation of the node only after device failure in lifetesting implies that the spike and the corresponding dark line defect are forming during the operation of the diode. The exact composition and structure of the spike are not yet known and are being investigated. The available evidence tends to indicate that the spike contains zinc from the diffusion front and that it provides non-radiative recombination sites which result in the observed dark line defect. The heat generated during device operation may cause zinc migration into the cavity when the diffusion front is sufficiently close to the active layer.

Ladany and Kressel[11,16,17] suggest that a highly doped zinc diffused region is a potential source of the defects that are involved in laser diode degradation. They observed improved reliability in devices in which zinc was eliminated from the active region. Our own preliminary lifetest data on deep zinc diffused laser diodes implies a similar conclusion. Shallower diffusions have been implemented since the discovery of the spikes in the active layer and no nodal failures have been observed during lifetesting of devices from wafers with the reduced zinc diffusion front depth.

## Acknowledgement

The authors would like to express their appreciation to Edwin R. Levin for his assistance with the cathodoluminescence analysis and to Vito Rossi for his aid in developing the angle lapping procedure.

References

1) J. J. Hsieh, "Zn Diffused, Stripe Geometry Double-Heterostructure GainAsP/InP Diode Lasers", IEEE J. Quantum Electronics, Vol. QE-15, pp. 694, August 1979.

2) G. Vassilieff and B. Saint-Cricq, "Zn Incorporation in GaAlAs Grown by Liquid Phase Epitaxy and its Electrical Properties", J. Appl. Phys. 54(8), pp. 4581, August 1983.

3) J. R. Shealy and S. R. Chinn, "Simultaneous Diffusion of Zinc and Indium into GaAs", Appl. Phy. Lett. 47(4), pp. 410, 15 August 1985.

4) Y. Yuan, K. Eda, G. A. Vawter, and J. L. Merz, "Open Tube Diffusion of Zn into AlGaAs and GaAs", J. Appl. Phys. 54(10), pp. 6045, October 1983.

5) A. H. van Ommen, "Examination of Models for Zn Diffusion in GaAs", J. Appl. Phys. 54(9), pp. 5055, September 1983.

6) S. E. Blum, M. B. Small, and D. Gupta, "Shallow Zn Diffusion in Liquid Phase Epitaxial GaAs and GaAlAs at 600$^{o}$C", Appl. Phys. Lett. 42(1), pp. 108, 1 January 1983.

7) U. Gosele and F. Morehead, "Diffusion of Zinc into Gallium Arsenide", J. Appl. Phys. 52(7), pp. 4617, July 1981.

8) S. K. Ageno, R. J. Roedel, N. Mellen, and J. S. Escher, "Diffusion of Zinc into GaAlAs", Appl. Phy. Lett. (11), pp. 1193, 1 December 1983.

9) H. K. Choi and S. Wang, "GaAs/GaAlAs Deep Zinc-Diffused Channel Substrate Laser", J. Appl. Phys. 54(6), pp. 3600, June 1983.

10) S. B. Phatak, "An Open Tube Method of Zinc Diffusion in III-V Compounds", IEEE Elect. Dev. Lett. 3(5), pp. 132, 5 May 1982.

# Appendix E

# A HIGH-POWER CHANNELED-SUBSTRATE-PLANAR AlGaAs LASER*

B. Goldstein, M. Ettenberg
N. A. Dinkel and J. K. Butler†
RCA Laboratories
Princeton, NJ 08540 (USA)

## Abstract

A channeled-substrate-planar AlGaAs laser has been operated to 190 mW cw. Principal optoelectronic behavior (power-current curves, single spatial and spectral mode behavior, far-field characteristics, modulation and astigmatism properties) will be discussed. Evidence for "hole-burning" is seen. Life-test data at power levels up to 100 mW is presented.

We report the principal results to date of an ongoing study of high-power CSP laser structures which, in our best case, has produced laser operation up to 190 mW cw (as given by the power-current curve), single fundamental spatial and spectral mode operation up to about 90 mW cw, with single spatial lobe operation continuing to 150 mW; beyond 70 mW there are increasing line broadening effects in the parallel far-field patterns accompanied by the appearance and growth (in a minor way) of spectral sidebands. The basic laser structure, grown by standard multi-bin LPE methods, is shown in Fig. 1(a) in schematic form, together with the pertinent dimensional and compositional information.

*This work was supported in part by NASA Langley Research Center, Hampton, Virginia, under Contract No. NAS1-17441.

†Southern Methodist University
Dallas, Texas 75275

Figure 1(b) is a photograph of a cleaved facet stained to delineate the contours of the channel, the cladding layers and the cap. Of critical importance is the avoidance of perturbations in the planarity of the active layer over the channel, and means of achieving this will be discussed.

We show in Fig. 2 the power-output/current-input (P-I) curves, the spectral content of the output, and the parallel and perpendicular far-field patterns at different output power levels. The laser facets for these measurements were coated with an $Al_2O_3$/Si dielectric stack to produce 90% reflectance on the back facet, and an approximately $\lambda/4$ $Al_2O_3$ layer to produce an approximately 10% reflectance on the front or emitting facet. The room temperature (23°C) cw threshold current is 48 mA and the differential quantum efficiency, $\eta$, at the emitting facet is 41%. The wavelength shift is that expected from the bandgap shift due to joule heating and a 25°C/watt mounted-diode thermal resistance. The full-widths-at-half-maximum (FWHM) at 20 mW for the parallel and perpendicular far-field patterns are, respectively, 6.5° and 27°. It is worth noting that after failure at 190 mW cw the laser facet visually showed no damage and the laser continued to be operable up to ~100-120 mW cw.

In Fig. 3 we have plotted both the FWHM for the parallel far-field pattern and the spectral side-band power (relative to the main spectral line) as a function of operating cw power; both increase with power in a similar way, including the almost identical slope changes at about 70 mW. Note that the appearance of the far-field pattern continues to be that of a fundamental mode (see inserts), and even though the asymmetry ultimately develops into well-defined structure at 170 mW, nowhere is there any discontinuity in FWHM one should expect if there had been any jump in spatial mode. These data indicate the presence of a strong passive waveguide in the lateral direction

below 70 mW. However, starting at 70 mW "hole-burning" begins to distort the dielectric profile, and any asymmetries in the now active waveguide at high drive levels will produce concomitant distortions in the far-field patterns.

Typical laser modulation behavior is indicated in Fig. 4 where we show the laser response to square current pulses at 14% duty cycle. The fall and rise times are $\lesssim$.5 nsec (the limit of pulse resolution); note the almost complete absence of tailing in both the leading and trailing edges of the output pulse, as well as a minimum of ringing oscillation. Modulation properties were found not to change at power levels up to 80 mW, the limit of the experiment.

Laser astigmatism was determined by measuring the position of minimum beam waist of the focussed far-field radiation. Such a plot is shown in Fig. 5 for both the horizontal and vertical directions, and the fact that the beam-waist minima occur at the same point in both directions indicates no astigmatic change with power level up to 75 mW. The relation between these results and the nature of the guiding in the laser will be discussed.

Life-test results will be discussed, including those from operation at accelerated modes at elevated temperatures (up to 50°C) and powers (up to 100 mW cw). Stability at 20 mW and 30°C is excellent, while even at the accelerated modes it is good. One unit operated at 100 mW for over 700 hrs. It is worth noting that as a rule laser failure is not accompanied by any clear visual signs of external mirror facet damage.

Continuing research will be discussed with emphasis on channel shape and the role of spatial hole-burning on high-power laser operation.

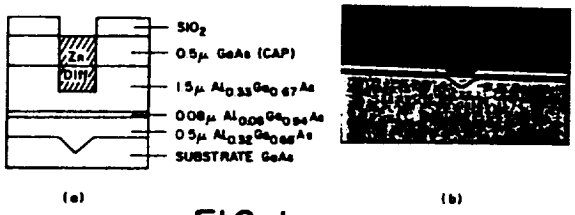


FIG. 1

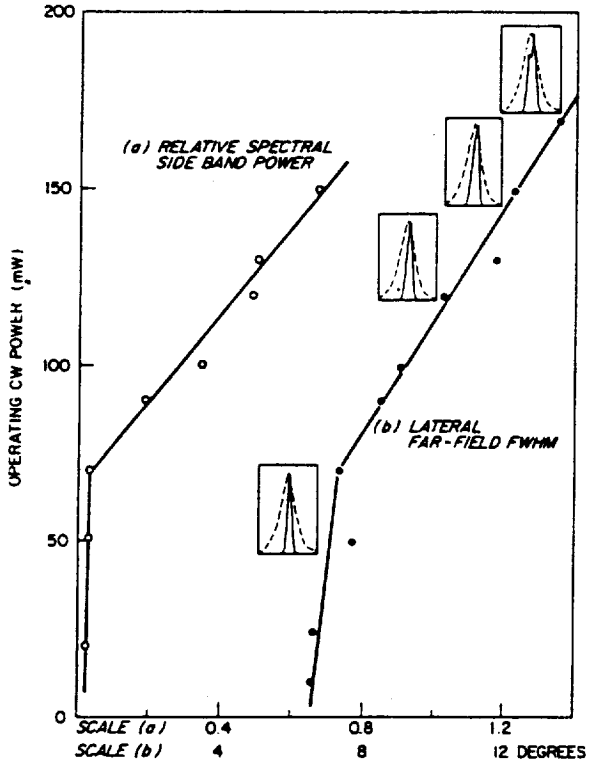


FIG. 3

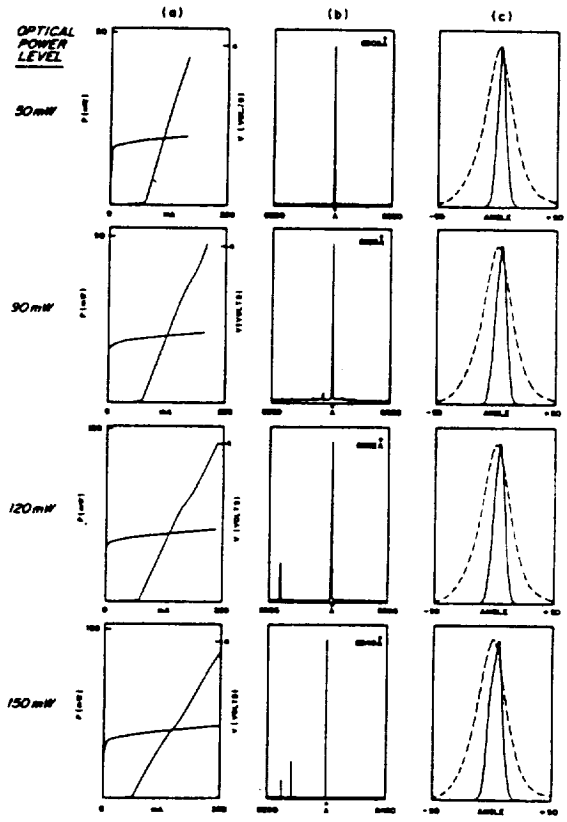


FIG. 2

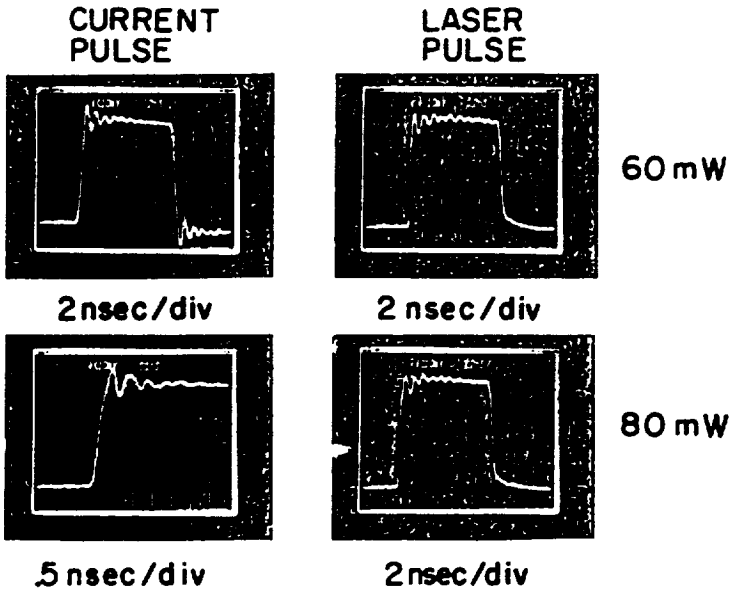


FIG. 4

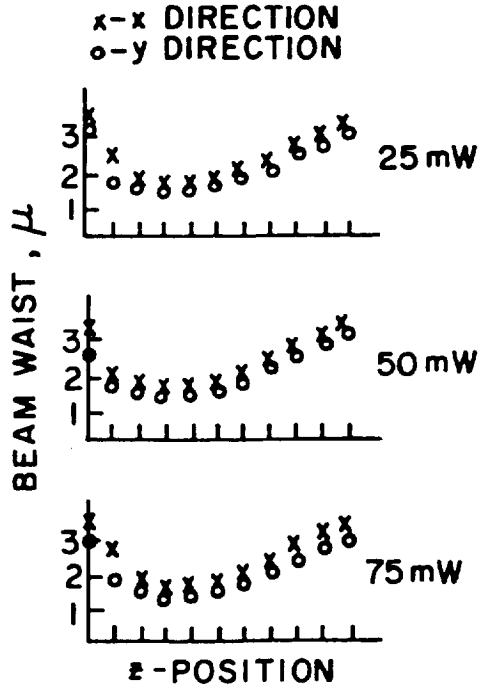


FIG. 5

# Appendix F

# An Efficient AlGaAs Channeled-Substrate-Planar Distributed Feedback Laser

B. Goldstein [a],G. Evans, J. Connolly, N. Dinkel, and J. Kirk

David Sarnoff Research Center

CN 5300

Princeton, N.J. 08853-5300

## ABSTRACT

A wavelength-locked, AlGaAs channeled-substrate-planar distributed feedback laser has been made that operates to 40 mW pulsed. The Bragg grating is situated at the shoulders of the substrate channel and is sandwiched between two protective layers of AlGaAs and GaAs. Overall power efficiencies of 15% have been measured at 40 mW of output power.

a) Present address: Solarex Corporation, 826 Newtown-Yardley Road, Newtown, Pa., 18940

# An Efficient AlGaAs Channeled-Substrate-Planar Distributed Feedback Laser

B. Goldstein, G. Evans, J. Connolly, N. Dinkel, and J. Kirk
David Sarnoff Research Center
CN 5300
Princeton, N.J. 08854-5300

The desirability of high power index-guided diode lasers operating in a wavelength-locked single longitudinal mode and with a well-defined lateral spatial mode is self-evident. Applications to space communications, optical recording and fiber-optics abound. The channeled substrate planar (CSP) AlGaAs laser[1,2,3] has by now been well-established as being routinely capable of supplying all the above mentioned properties except spectral stabilization. Recently, efficient gain-guided distributed feedback (DFB) AlGaAs lasers[4], ridge-guide DFB lasers[5] grown by two-step molecular beam epitaxial (MBE) processes, and buried heterostructure DFB lasers[6] grown by three-step liquid phase epitaxial (LPE) processes have been reported that operate at 8700-8800Å.

In this letter we report a CSP-DFB laser operating at ≈8300Å with good overall efficiency that is grown by a one-step LPE process on a substrate containing a second order ($\Lambda$=2415Å) DFB

grating. The grating is placed between two protective layers grown by metalorganic chemical vapor deposition (MOCVD) with an index step at the interface and is situated on the shoulders of the substrate channel.

The insertion of the $Al_{.15}Ga_{.85}As$ layer (in place of GaAs in a conventional CSP laser) slightly increases (≈15.6%) the magnitude of the complex effective index step which controls the lateral optical confinement: the real part of the complex effective increases from $4.119 \times 10^{-3}$ to $5.999 \times 10^{-3}$, while the imaginary part decreases from $4.40 \times 10^{-3}$ to $3.54 \times 10^{-3}$. Our calculations show that the percentage of the lateral near-field intensity which is outside the channel and interacts with the gratings ranges from 16% to 1% as the channel width increases from 2 μm to 8 μm for the CSP parameters corresponding to Fig. 1. A CSP laser having a channel width of 4.2 μm would have appoximately 4% of the lateral field in the grating region of the structure. Evanescent field interaction with a grating to provide DFB has been previously reported for a buried heterostructure laser[7].

The structure is shown schematically in Fig. 1(a) and in stained cross-sectional cleave in Fig. 1(b). Details of the device can be seen more clearly in Fig. 1(c) where we show a stained cross-section lapped at a 1° angle in the vertical direction. The substrate is prepared by chemically-etching a second-order grating using a photoresist mask obtained by standard holographic

interferometry into a 0.8 μm thick n-type $Al_{.15}Ga_{.85}As$ layer. A 0.12 μm thick GaAs layer is then grown over the grating. These layers are grown using MOCVD growth for improved uniformity and surface morphology. MOCVD growth also improves the nucleation of the GaAs layer on the $Al_{.15}Ga_{.85}As$ grating surface. The $Al_{.15}Ga_{.85}As$ layer prevents meltback of both the vee-channel and the grating while the GaAs layer grown over the grating, provides a nucleating surface during subsequent LPE growth. The index step at the grating interface is approximately 0.1.

After the grating and its protective layers have been fabricated, a 4.2 μm wide vee-channel is chemically etched into the substrate and four layers are grown: 1) $Al_{.33}Ga_{.67}As$ cladding layer (0.3μm, $N_d=1x10^{18}$ $cm^{-3}$); 2) $Al_{.06}Ga_{.94}As$ active layer (0.07μm, $N_d=1x10^{17}$ $cm^{-3}$); 3) $Al_{.33}Ga_{.67}As$ cladding layer (1.5μm, $N_a=5x10^{17}$ $cm^{-3}$); 4) GaAs capping layer (0.7μm, $N_d=5x10^{17}$ $cm^{-3}$). The growth is performed at 800°C using a cooling rate of 1°C. This procedure significantly reduces the complexity of fabricating DFB-CSP structures and lends itself to a high-volume manufacturing process. In addition, the current path in the device does not include a regrowth interface which has been associated with higher than normal series resistance for devices fabricated with one or more growth interfaces in the current flow path[7]. After LPE growth, routine contacting technology completes the device which includes Zn stripe diffusion for current-confinement (see Fig.

1(a)), Ti/Pt/Au for the p-contact and AuGe/Ni/Au for the n-contact.

The CSP-DFB laser displayed DFB operation at pulsed (1% duty cycle; 100 nsec) power levels up to 40 mW and at cw power levels up to 10 mW. We show in Fig. 2, the change in the single longitudinal mode spectrum for a DFB-CSP laser operating over the temperature range of 24-32°C. The pulsed output power from the device was maintained at 10 mW. The facets of the device were coated (front-10%; rear-85%) and no attempt was made to suppress the Fabry Perot modes. Sideband rejection ratios are in the range of 18-23 db. The observed pulsed spectra were characteristic of DFB lasers in that they remained single line for all temperatures[8]. A typical pulsed spectrum for this device operating at 28°C can be seen in Fig. 2. The wavelength temperature dependence for both pulsed and cw operation is about 0.7Å/°C. This behavior is that expected for an AlGaAs laser of the given composition and layer thickness operating at 8300 Å[9]. The fact that the DFB behavior described above occurs over a relatively small temperature range and at powers only up to 40 mW pulsed can be associated with the small grating depth (≈100-200Å) produced by chemical etching in the dovetail direction. Improved performance is expected with deeper (500 Å to 1000 Å) gratings.

Figure 3, (a) and (b) shows the P-I curve and far-field patterns, respectively, demonstrating thresholds as low as 50 mA,

kink-free power curves and well-defined single spatial modes. The overall efficiency of the laser at 40 mW (total input electrical power divided by output optical power) is 15%. Thus, incorporation of the grating and the accompanying extra layers (see Fig. 1) do not interfere with the desirable spatial mode and high-power properties of the basic CSP structure.

In conclusion, a channeled substrate planar laser with distributed feedback has been fabricated using conventional single-step liquid phase epitaxial growth. This DFB-CSP operated in a stable single longitudinal mode up to 40 mW of output power and displayed an overall power conversion efficiency of 15%.

The authors wish to express their appreciation to J. Berkshire, D. Gilbert, M. Harvey, and D. Tarangioli for their technical assistance and to M. Ettenberg for helpful discussions. This work was supported, in part, by the National Aeronautics and Space Administration, Langley, VA, under contract No. NAS1-17441.

## Figure Captions

Figure 1. (a) Schematic diagram of CSP-DFB laser. (b) Stained cross-sectional cleave of CSP-DFB structure. (c) Stained cross-sectional cleave lapped at a 1° angle in the vertical direction. Note especially the beginning of meltback between the n-clad and n-buffer layers.

Figure 2. Wavelength shift as a function of heat-sink temperature for a CSP-DFB laser operating pulsed at an output power of 10 mW.

Figure 3. (a) Power-current curves for a CSP-DFB laser. (b) Far-field radiation patterns for a CSP-DFB laser.

## References

1 T. Kuroda, M. Nakamura, K. Aiki, and J. Umeda, Applied Optics, Vol 17, No. 20, 15 Oct. 1978, pp 3264-3267.

2 B. Goldstein, M. Ettenberg, N. Dinkel, and J. Butler, Appl. Phys. Lett. **47**, 655 (1985).

3 T. Shibutani, M. Kume, K. Hamada, H. Shimizu, K. Itoh, G. Kano, and I. Termoto, IEEE J. Quantum Electron. **QE-23**, 760 (1987).

4 K. Kojima, S. Noda, K. Mitsunaga, K. Kyuma, and T. Nakayama, *Technical Digest of 5th International Conference on Integrated Optics and Optical Fibre Communication* (International Institute of Communications, Venice, Italy, 1985), p. 99.

5 S. Noda, K. Kojima, K. Mitsunaga, K. Kyuma, K. Hamanaka, and T. Nakayama, IEEE J. Quantum Electron. **QE-23**,188 (1987).

6 Y. Nakano and K. Tada, Appl. Phys. Lett. **49**,1145 (1986).

7 W. Tsang, R. Logan, and L. Johnson, Appl. Phys. Lett. **34** (11), 752 (1979).

8 S. Noda, K. Kojima, K. Mitsunaga, K. Kyuma, and T. Nakayama, Appl. Phys. Lett. **48** (1), 4 (1986).

[9] K. Aiki, M. Nakamura, J. Umeda, A. Yariv, A. Katzir, and H. W. Hen, Appl. Phys. Lett. **27**, 145 (1975).

# Structure of DFB-CSP Laser

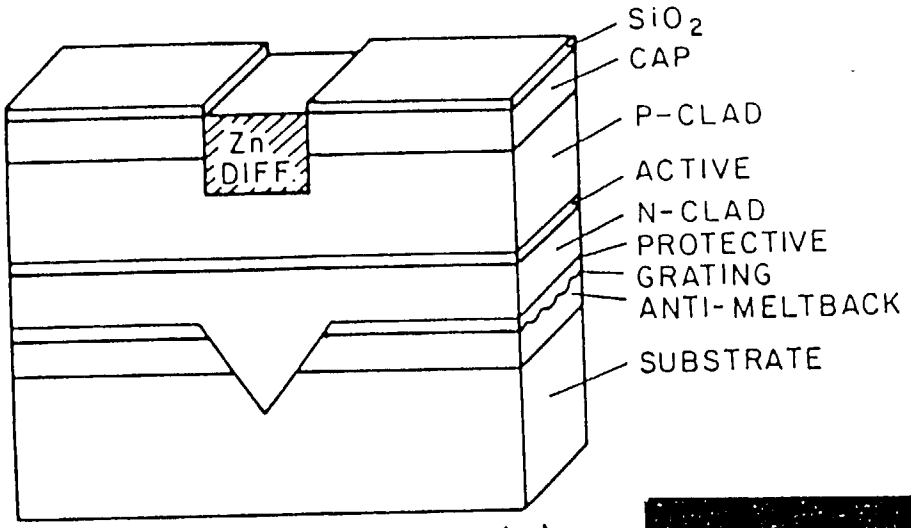


DFB-CSP LASER (a)

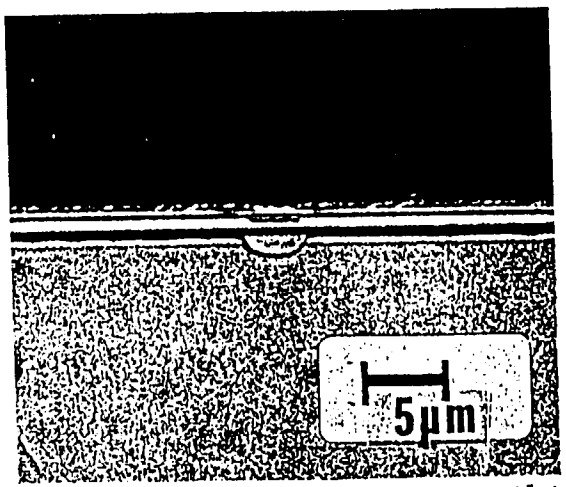


CROSS-SECTION CLEAVE (b)

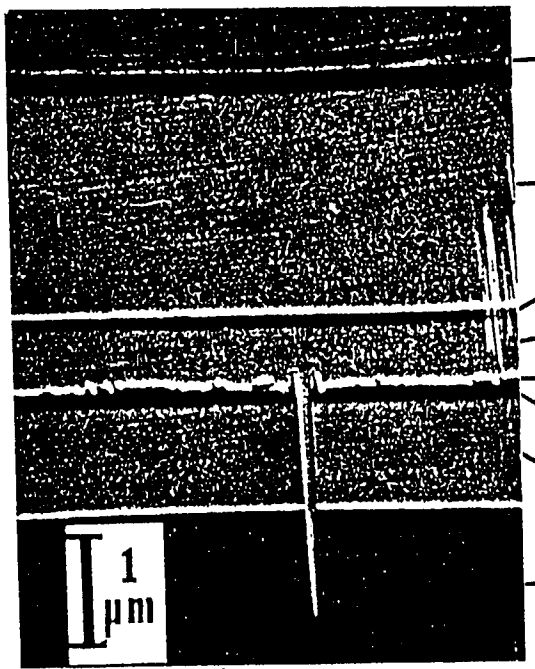


CROSS-SECTION 1°ANGLE-LAP (c)

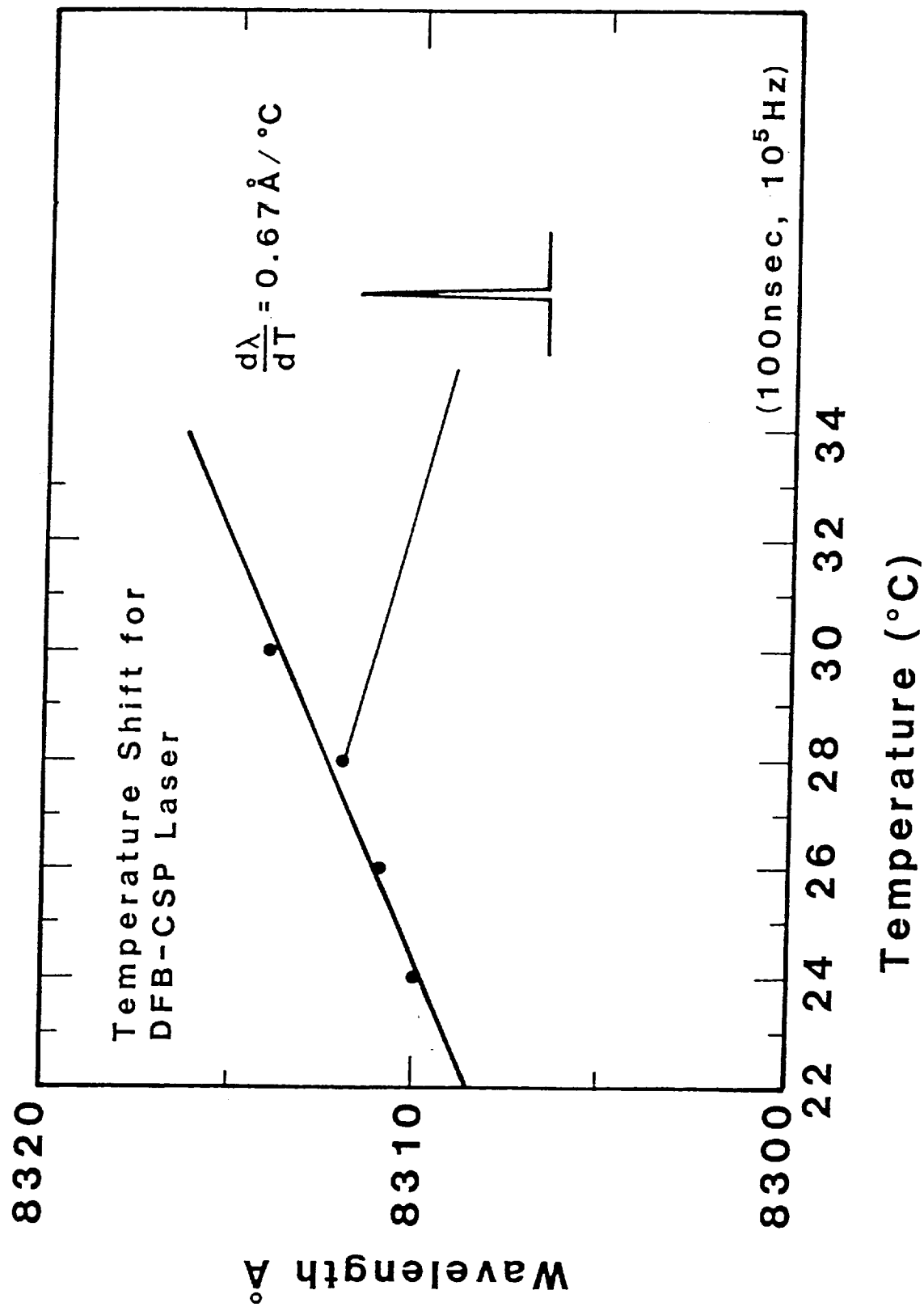
Temperature Shift for
DFB-CSP Laser
$\frac{d\lambda}{dT} = 0.67 Å / °C$
(100nsec, $10^5$Hz)
Wavelength Å
8320
8310
8300
22
24
26
28
30
32
34
Temperature (°C)

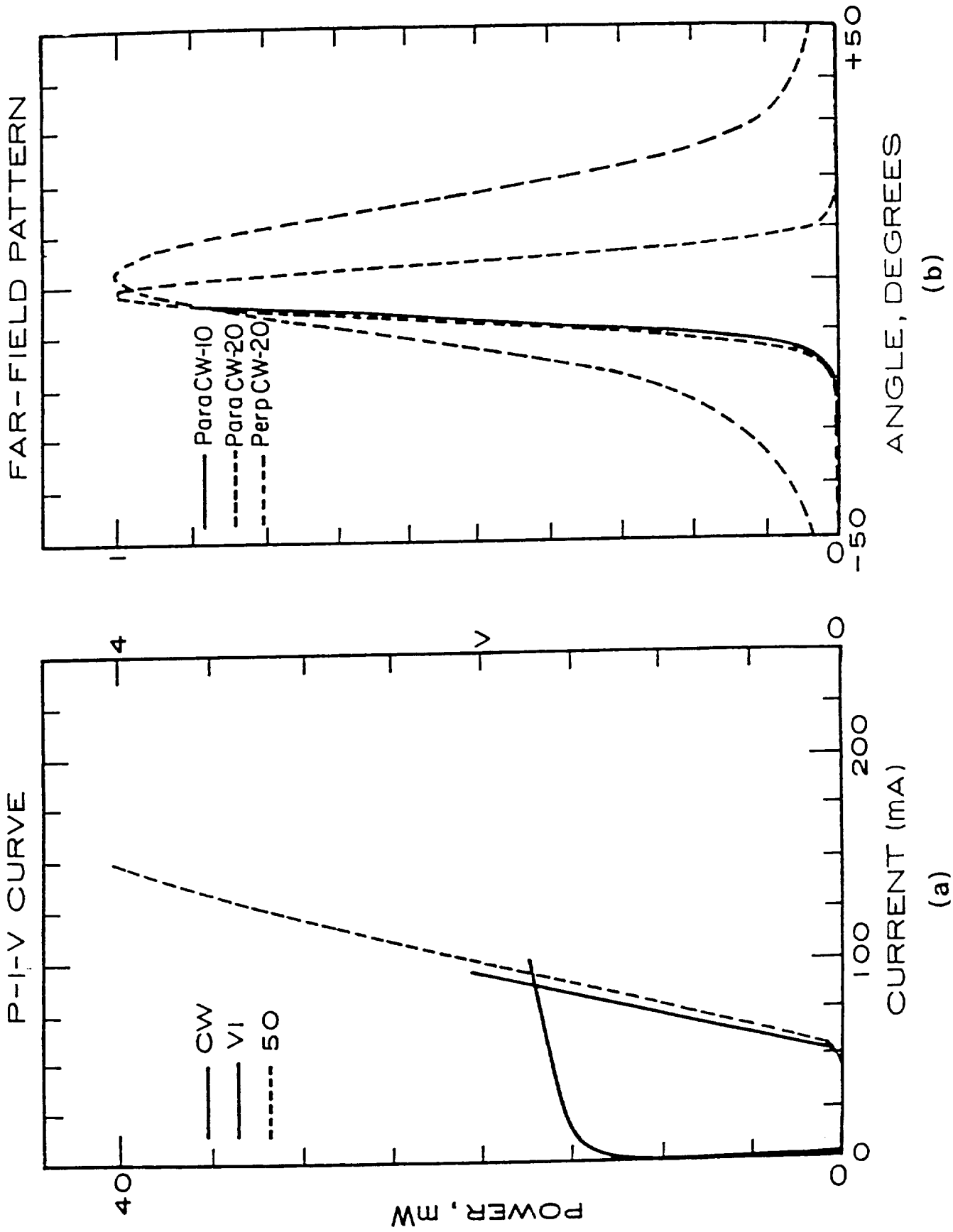
FAR-FIELD PATTERN
Para CW-10
Para CW-20
Perp CW-20
ANGLE, DEGREES
+50
0
-50
(b)
P-I-V CURVE
CW
VI
50
POWER, mW
CURRENT (mA)
40
0
200
100
(a)

NASA
National Aeronautics and Space Administration

# Report Documentation Page

| 1. Report No. | 2. Government Accession No. | 3. Recipient's Catalog No. |
|---|---|---|
| NASA CR-4189 | | |

**4. Title and Subtitle**
High-Power AlGaAs Channeled Substrate Planar Diode Lasers for Spaceborne Communications

**5. Report Date**
November 1988

**6. Performing Organization Code**

**7. Author(s)**
J. C. Connolly, B. Goldstein, G. N. Pultz, S. E. Slavin, D. B. Carlin, and M. Ettenberg

**8. Performing Organization Report No.**

**10. Work Unit No.**
506-44-21-01

**9. Performing Organization Name and Address**
David Sarnoff Research Center
Princeton, NJ 08543-5300

**11. Contract or Grant No.**
NAS1-17441

**12. Sponsoring Agency Name and Address**
National Aeronautics & Space Administration
Langley Research Center
Hampton, Virginia 23665-5225

**13. Type of Report and Period Covered**
Contractor Report
8/4/86 through 7/15/87

**14. Sponsoring Agency Code**

**15. Supplementary Notes**
Langley Technical Monitor: Herbert D. Hendricks
Final Report

**16. Abstract**

A high-power channeled substrate planar AlGaAs diode laser with an emission wavelength of 8600-8800 Å has been developed. The opto-electronic behavior (power-current, single spatial and spectral behavior, far-field characteristics, modulation, and astigmatism properties) and results of computer modeling studies on the performance of the laser will be discussed. Lifetest data on these devices at high output power levels is also included. In addition, a new type of channeled substrate planar laser utilizing a Bragg grating to stabilize the longitudinal mode has been demonstrated. The fabrication procedures and optoelectronic properties of this new diode laser are described.

| 17. Key Words (Suggested by Author(s)) | | 18. Distribution Statement |
|---|---|---|
| semiconductor laser | Bragg grating | Unclassified - Unlimited |
| high power | distributed feedback | Subject Category 36 |
| mode stabilized | | |
| single longitudinal mode | | |
| AlGaAs (Aluminum Gallium Arsenide) | | |

| 19. Security Classif. (of this report) | 20. Security Classif. (of this page) | 21. No. of pages | 22. Price |
|---|---|---|---|
| Unclassified | Unclassified | 168 | A08 |

NASA FORM 1626 OCT 86

NASA-Langley, 1988